

**COMPUTATIONAL MODELING OF FAILURE IN THERMAL
BARRIER COATINGS UNDER CYCLIC THERMAL LOADS**

DISSERTATION

Presented in Partial Fulfillment of the Requirements for
the Degree Doctor of Philosophy in the Graduate
School of The Ohio State University

By

Himanshu Bhatnagar, B.Tech, M.S.

* * * * *

The Ohio State University
2009

Dissertation Committee:

Prof. Somnath Ghosh, Advisor

Prof. M.E. Walter

Prof. James Williams

Prof. June K Lee

Approved by

Advisor
Graduate Program in
Department of Mechanical Engineering

ABSTRACT

In this dissertation, finite element models are used to investigate catastrophic failure of thermal barrier coatings (TBCs) due to delaminations along susceptible interfaces of thermally grown oxide (TGO) with the ceramic top coat and the inter-metallic bond coat. The materials and geometries in the studies are chosen to be representative of TBC materials in real applications.

The characteristics of the failure modes along the TGO and bond coat interface (*e.g.* buckling instability and strain energy driven delamination propagation) are investigated using thermo-elastic finite element models. The solution of a linear elastic eigen-value problem determines the onset of the buckling instability with a pre-existing delamination between bond coat and the TGO. The virtual crack extension method is employed to study strain energy release rate driven interfacial delamination at wavy interfaces. The materials and geometries in the study are chosen to be representative of TBC materials in real applications. Extensive sensitivity analyses are conducted to identify the critical design parameters affecting the onset of buckling and extension of interfacial delamination, as well as to develop parametric relations that enhance the understanding of these mechanisms. Finally, a numerical exercise demonstrates that the buckling instability is the leading failure mechanism at flat interfaces or at the locations of

minimum cross-section in a wavy interface. However, in the vicinity of waviness, crack extension becomes a dominant mode of failure.

The top coat crack initiation and propagation is investigated using a thermo-elastic finite element model with bond coat creep. Cracks are assumed to initiate when the maximum principal stress exceeds rupture stress of the top coat. A sensitivity analysis estimates the contribution of geometric and material parameters and forms a basis to develop parametric relation to estimate maximum principal stress. Subsequently, crack propagation simulations using a hysteretic cohesive zone model are performed for parametric combinations which initiate cracks away from the interface. These analyses conclude that parametric combinations initiating top coat cracks also assist in propagation and eventual delamination of TGO and top coat interface.

A homogenization based continuum damage mechanics (HCDM) modeling framework is proposed for TBC failure effects of top coat microstructural defects. An extended Voronoi cell finite element (X-VCFEM) is employed to perform the micro-mechanical analysis of RVE and the results show that HCDM model has limited validity due to loss of material stability with significant damage. A sensitivity analysis reveals that the range of HCDM validity is dependent on top coat cohesive energy.

Dedicated to my wife Asha, son Rishabh and
my parents for their love and support.

ACKNOWLEDGEMENTS

I would like to express my sincere gratitude to my advisors, Prof. Somnath Ghosh and Prof. Mark E. Walter for their support, patience, and enthusiasm that made this work possible. I would like to thank Prof. James Williams for his generosity and guidance. I would like to give special thanks to Prof. June K Lee and Prof. Gregory Washington for taking out time to participate in my doctoral committee. I am grateful for the support provided by the National Aeronautics and Space Administration (NASA) through a University Research Engineering Technology Institute (URETI) grant to the Ohio State University for Aeropropulsion and Power Technology (UAPT). Computer support by the Ohio Supercomputer Center through grant PAS813-2 is also gratefully acknowledged.

I would like to thank my fellow lab research associates Dakshina Murthy Valiveti, Jayesh Jain, Kapil Nandawana, Anand Srivastava, Deepu Joseph, Kedar Kirane, Abhijeet Tiwari, Sanket Sarkar, Sivom Manchiraju, Jie Bai, Gayathri Venkataramani and Shanhu Li for the discussions and help throughout the course of my study.

Finally, I would like to thank my family especially my wife and son whose continuous love, support and patience made it possible for me to finish this dissertation.

VITA

- 1975.....Born – New Delhi, India
- 1998.....B.Tech. Mechanical Engineering,
Institute of Technology, B.H.U,
Varanasi, U.P, India
- 2003 – Present.....Graduate Research Associate
The Ohio State University
Columbus, OH USA
- 2008.....M.S. Mechanical Engineering,
The Ohio State University
Columbus, OH USA

PUBLICATIONS

Research Publications

H. Bhatnagar, M.E. Walter and S. Ghosh, A Parametric Domain Map for Top Coat Damage Initiation and Propagation, *Int. Journal for Multiscale Computational Engineering*, 2007, 5:227

H. Bhatnagar, S. Ghosh and M.E. Walter, Parametric Studies of Failure Mechanisms in Elastic EB-PVD Thermal Barrier Coatings Using FEM, *Int. Journal of Solids and Structures*, 2006, 4384-4406

H. Bhatnagar, S. Ghosh, M.E. Walter, Computational Modeling of Competing Failure Mechanisms in EB-PVD Thermal Barrier Coatings, *Proceedings of SES 2008 Conference*, 2008, Champaign, IL

H. Bhatnagar, Computational Modeling of Competing Failure Mechanisms in EB-PVD Thermal Barrier Coatings, *Edward Hayes Research Forum*, 2006, Columbus, OH

H. Bhatnagar, S. Ghosh, M.E. Walter, Computational Modeling of Competing Failure Mechanisms in EB-PVD Thermal Barrier Coatings, *Proceedings of SES 2006 Conference*, 2006, College Station, PA

H. Bhatnagar, S. Ghosh, M.E. Walter, Computational Simulation of Failure in EB-PVD Thermal Barrier Coatings, *8th USNCCM Conference*, 2005, Austin, TX

H. Bhatnagar, H. Kim, M.E. Walter, S. Ghosh, *Proceedings of ASME 2005 IMECE*, 2005, Orlando, FL

H. Kim, H. Bhatnagar, M.E. Walter, S. Ghosh, *Proceedings of ASME 2004 IMECE*, 2004, Anaheim, CA

H. Bhatnagar, S. Ghosh and M.E. Walter, Numerical Parametric Study of Macroscopic Failure Mechanism in EBPVD Thermal Barrier Coatings, *Proceedings of NUMIFORM 2004 International Conference*, 2004, Columbus, OH

FIELDS OF STUDY

Major Field: Mechanical Engineering

TABLE OF CONTENTS

Abstract.....	ii
Acknowledgements	v
Vita	vi
List of Tables	xi
List of Figures.....	xii
1. Introduction.....	1
1.1 Motivation.....	1
1.2 Scope of Proposed Research.....	5
1.3 Organization of this dissertation	7
2. Parametric Studies of Competing Failure Mechanisms in Elastic EB-PVD	
Thermal Barrier Coatings Using FEM.....	10
2.1 Introduction.....	10
2.2 Mechanisms of TBC failure and solution methods.....	13
2.2.1 Buckling Instability at Flat and Wavy Interfaces.....	14
2.2.2 Delamination Growth by Crack Propagation at Interfaces	16
2.3 Finite Element Models of the TBC	18
2.3.1 Material Properties	18
2.3.2 Geometric Model and Finite element Mesh.....	20
2.3.3 Boundary conditions	21
2.4 Parametric Modeling of Buckling Instability and Interfacial Crack Extension....	22
2.4.1 Validation Study of the Computational Model	23
2.4.2 Critical Stress Analysis for Buckling Instability in the TBC.....	26
2.4.3 Estimating Energy Release Rate for Interfacial Crack Extension	35
2.5 Competition Between Buckling and Crack Extension Modes.....	43

2.6 Conclusions.....	46
3. A Parametric Domain Map for Top Coat Damage Initiation and Propagation in EB-PVD Thermal Barrier Coatings.....	61
3.1 Introduction.....	61
3.2 The Top Coat Failure Mechanisms And Solution Approach.....	64
3.2.1 Crack Initiation within the Top Coat	65
3.2.2 Propagation of Cracks Originating within the Top Coat	66
3.3 Finite Element Models of TBC.....	75
3.3.1 Material Models	75
3.3.2 Geometric Model and Finite Element Mesh	78
3.3.3 Boundary Conditions	79
3.3.4 Cohesive Zone Element Implementation.....	80
3.4 Parametric Modeling of Crack Initiation and Propagation in the Top coat.....	81
3.4.1 Sensitivity Analysis for Crack Initiation within the Top Coat	81
3.4.2 Parametric Domain Map for Damage Initiation in the Top Coat	85
3.4.3 Sensitivity Analysis for Crack Propagation within the Top Coat.....	88
3.5 Comparison of Numerical Prediction with Experiments	90
3.6 Conclusions.....	92
4. A Parametric Study of Damage Initiation and Propagation in EB-PVD Thermal Barrier Coatings.....	104
4.1 Introduction.....	104
4.2 Finite Element Models of TBCs	105
4.2.1 Material Models	107
4.2.2 Geometric Model and FEM Mesh	108
4.2.3 Boundary Conditions	109
4.2.4 Irreversible Hysteretic Mixed-Mode Cohesive ZONE MODEL.....	110
4.2.5 Incremental Direction of Crack Propagation	113
4.2.6 Selection of Cohesive zone parameters	115
4.3 Parametric Modeling of Crack Initiation in the Top coat.....	116
4.3.1 Parametric Representation for Crack Initiation in the Top Coat	118

4.4 Parametric investigation of top coat Crack Propagation.....	119
4.4.1 Validation of Top Coat Crack Propagation Direction	120
4.4.2 Top Coat Crack Propagation Results.....	121
4.4.3 Effect of Top Coat Cracks on TGO and Top Coat Interface Delamination ..	122
4.5 Comparison of Numerical Prediction with Experiments	124
4.6 Conclusions.....	125
5. A Homogenization Based Continuum Damage MecHanics Modeling Framework	
for Thermal Barrier Coatings.....	135
5.1 Introduction.....	135
5.2 Voronoi Cell Finite element assumptions and weak form.....	138
5.3 Creation of Enriched Stress Functions in X-VCFEM.....	141
5.3.1 Pure Polynomial Forms of Stress Function	142
5.3.2 Branch Stress Functions Using Level Set Methods	142
5.3.3 Multi-resolution Wavelet based stress Functions	144
5.4 X-VCFEM Solution Method.....	146
5.5 Aspects of Numerical Implementation of X-VCFEM	152
5.5.1 Stability Conditions	152
5.5.2 Adaptive criteria for cohesive crack growth	152
5.5.3 Elimination of element rigid body modes.....	157
5.5.4 Crack Update Procedure	158
5.6 Numerical examples using X-VCFEM.....	159
5.7 Homogenization Based Continuum damage mechanics (HCDM) model	163
5.7.1 Damage State Variable	165
5.7.2 Principal Damage Coordinate System (PDCS).....	166
5.7.3 Micromechanical RVE mOdel With Cohesive Zone Elements.....	167
5.7.4 Homogenization and Stiffness Evaluation.....	170
5.8 Evolution Equations for the Homogenization based Model in PDCS	172
5.9 Sensitivity Analysis of Validity of HCDM for top coat damage.....	173
5.10 Conclusions.....	176
6. Conclusions and Future Studies	187
Bibliography	193

LIST OF TABLES

Table	Page
2.1	Material properties of components of the TBC system [7,29,30].....49
2.2	Critical buckling load comparison with results in [32].....49
2.3	Discontinuities in the values of σ^b at the edges of each h/R ratio range in the parametric Eqns. 2.9 and 2.10.....49
2.4.	Range of variation of parameters from experimental observations [2,21,38-41] for energy release rate study50
2.5.	Functional relation between energy release rate and critical parameters, based on sensitivity analysis using FEM simulations. The values h_0 , t_0 , R_0 , E^* and c_n (n=1-10) are constants that are determined using the least square fit technique50
3.1.	Material properties of components of the TBC system as obtained from [7,29,58].....95
3.2.	Range of variation of parameters from experimental observations reported in [4,7,21,38,39,59]95

LIST OF FIGURES

Figure	Page
1.1 A SEM image [20] of the TBC microstructure consisting of the top coat, the thermally grown oxide layer, the bond coat and the super-alloy substrate	9
2.1 A SEM image of the TBC microstructure [20] consisting of the top coat, the thermally grown oxide layer, the bond coat and the super-alloy substrate	51
2.2 Schematic diagrams showing the competing failure mechanisms in TBC systems with flat and wavy interfaces.....	51
2.3 Schematic diagrams showing (a) geometric and dimensional parameters (b) finite element model of the TBC system with bond coat lower interface rigid, symmetry at vertical edge of delamination (right) and radial periodicity at the vertical edge of the bonded part (left) (c) close-up of the mesh at the crack tip	52
2.4 Contour plots showing transverse stress (GPa) at fully bonded wavy interfaces for (a) Type I undulation penetrating completely into the bond coat; (b) Type II undulation protruding completely into the top coat.....	52

2.5	Plots showing (a) the comparison between the finite element results and a low order analytical solution [10], (b) comparison of finite element results and a higher order analytical solution [43].....	53
2.6	Plots for the two layer TBC, showing critical buckling load sensitivity to (a) geometric parameters and (b) material parameters	54
2.7	Plots of the critical buckling stress as a function of h/R ratio for the two layer TBC, obtained with the parametric relations and finite element solution for the axisymmetric case.....	55
2.8	Plots for the three layer TBC, showing the variation of normalized critical buckling stress with (a) top coat thickness (t) and (b) top coat modulus E_{TC}	56
2.9	Plot showing the sensitivity of the energy release rate with respect to (a) geometric parameters; and (b) material parameters	57
2.10	Plot showing the sensitivity of the energy release rate with respect to (a) undulation parameters, (b) expansion mismatch stress in the TGO and top coat.....	58
2.11	Plot showing the comparison of energy release rate (G) near an interfacial undulation with the steady state energy release rate (G_{ss}) at an edge delamination [43] for $h/R=0.2$, $t=10 \mu\text{m}$, $W=30 \mu\text{m}$ and $\sigma_{TGO}=2.17 \text{ GPa}$	59

2.12	Plot showing the variation of the normalized energy release rate as the interfacial crack propagates along an interfacial undulation for $W=20\ \mu\text{m}$, $A=4\ \mu\text{m}$ and $G^{\text{max}}=21\ \text{J/m}^2$	60
2.13	Plot showing (a) the competition between buckle initiation and interface crack extension, (b) the corresponding locations for energy release rate curves and for study of the competition between buckling and delamination propagation	61
3.1	Schematic diagram of the TBC model showing geometric and dimensional parameters of the undulation as well as the location of the crack characterized by normal distance v . The substrate, excluded here for clarity, is included in the finite element model.....	96
3.2	A plot showing the hysteretic cohesive zone element response with cyclic loading to eventual failure when $\delta=\delta_e=0.001$	96
3.3	Finite element model (not to scale) of the TBC system with the bottom of substrate constrained to remain flat, symmetry at left vertical edge and radial periodicity at the right vertical edge.....	97
3.4	Plots showing top coat principal stress sensitivity to (a) geometric parameters, (b) material parameters and (c) thermal load cycle parameters	98
3.5	Plots showing sensitivity of the location of principal stress to (a) geometric parameters, (b) material parameters and (c) thermal load cycle	100

3.6	Plot showing the domain map of the parametric space delineating TBC designs into safe, sub-safe and fail combinations based on two unique combinations of parameters ψ and ξ	102
3.7	Plots showing sensitivity of the incremental direction of crack propagation to geometric parameters.....	103
4.1	An SEM image of the TBC microstructure [20] consisting of the top coat, the thermally grown oxide layer, the bond coat and the super-alloy substrate	127
4.2	Schematic diagrams showing (a) geometric and dimensional parameters (b) finite element model (not to scale) of the TBC system with boundary conditions.....	127
4.3	A plot showing the hysteretic cohesive zone element response with cyclic loading to eventual failure when $\delta = \delta_e = 0.001$	128
4.4	Plot showing the convergence of crack propagation angle with increasing cohesive stiffness (σ_{max} / δ_e).....	128
4.5	Plots showing top coat principal stress sensitivity to (a) geometric parameters, (b) material parameters.....	129
4.6	Plots of principal stress contours showing crack arrest when prescribed path deviates by (a) 30 degrees and (b) 90 degrees from that predicted by Eqn. 5	130

4.7	Plots showing the variation in (a) incremental crack propagation direction and (b) crack propagation rate as the crack propagates along an initially assigned path towards the interface	131
4.8	Plots showing the topcoat principal stress contours when topcoat and TGO interface is (a) perfectly bonded and (b) laced with very stiff cohesive zone elements	132
4.9	Principal stress contour plots showing crack trajectories for TBC geometry defined by (a) $A=10\ \mu\text{m}$, $W=20\ \mu\text{m}$ and $h=6\ \mu\text{m}$ and (b) $A=10\ \mu\text{m}$, $W=30\ \mu\text{m}$, $h=4\ \mu\text{m}$	133
4.10	Comparison of top coat crack trajectory (a) schematic of SEM micrograph observations [7] with (b) finite element simulation. The geometric parameters are $A=10\ \mu\text{m}$, $W=30\ \mu\text{m}$, $t=3\ \mu\text{m}$	134
5.1	A SEM image of the TBC microstructure [20] showing the diffused nature of micro cracks in the top coat	178
5.2	(a) A mesh of Voronoi cell elements generated by tessellation of the heterogeneous microstructural domain. (b) A typical Voronoi cell element enriched by wavelet functions	179
5.2	Schematic of a snap-back response with crack propagation.....	180
5.4	Schematic showing parameters associated with crack propagation within a Voronoi cell.	180

5.5	Schematic of a center cracked plate geometry subjected to uniaxial tension σ_0 .	181
5.6	A σ_{22} normal stress contour plot of center cracked plate subjected to uniaxial tension after significant crack propagation	181
5.7	A comparison of the macroscopic stress-strain response of an elastic center cracked plate using complete reloading and incremental loading with crack update. The stress and strain are normalized with $\sigma^{max}=147$ MPa and $\epsilon^{max}=1.E-5$.	182
5.8	The mechanical response of a center cracked plate with irreversible cohesive elements using incremental loading with crack updates.	182
5.9	A schematic showing a plate with two inclined cracks contained in two Voronoi cells and subjected to uniaxial vertical tensile load. The initial crack geometry is depicted with the solid line and the subsequent trajectory is illustrated with dashed lines.	183
5.10	The macroscopic response from uniaxial loading of the plate with two inclined cracks shown in Fig. 5.9	183
5.11	Rate independent irreversible traction separation cohesive law	184
5.12	An RVE schematic showing the crack trajectory with an inclined crack subjected to unit tensile strain along horizontal axis. The initial crack geometry is depicted with solid line and the subsequent trajectory is illustrated with dashed line	184

5.13	a) The macroscopic response of the RVE, and b) the relationship between damage state variable (κ) and damage work for increasing values of δ_c	185
5.14	A plot showing the relationship between the critical value of damage state variable (κ_c) and cohesive energy associated with the cohesive zone elements.....	186
5.15	A plot showing the degradation of the secant stiffness E_{2222} of the top coat RVE for increasing damage work.....	186

CHAPTER 1

INTRODUCTION

1.1 MOTIVATION

State-of-the-art electron beam physical vapor deposition (EB-PVD) thermal barrier coatings (TBCs) are used in gas turbine engines to protect components from high temperature gases and severe transient thermal loading. As shown in the SEM micrograph of Fig. 1.1, a conventional TBC consists of three layers deposited on a super-alloy substrate. The first layer is a 50-100 μm thick bond coat that provides oxidation protection, while the second is a 100-120 μm thick top coat for providing thermal insulation. The 'strain tolerant' top coat is structured to limit strain induced cracking and subsequent delamination; strain tolerance is achieved by incorporating micro-cracks or aligned porosity in the material [1]. Typically, due to its low, temperature-insensitive thermal conductivity [1], Yttria stabilized Zirconia is the material of choice for the top coat. The top coat is transparent to oxygen, and thus a third layer, the thermally grown

oxide (TGO) forms as the bond coat oxidizes. Due to TGO growth and the creep deformation of the bond coat, the morphology of the TGO interfaces with adjoining layers continues to evolve during the life of the TBC [2]. As shown in Fig. 1.1, the SEM images of the TBC microstructure reveal that the TGO interfaces have both planar and wavy sections.

Individual layers in TBCs are significantly stronger than the interfaces between the top coat and TGO and between the TGO and bond coat. Furthermore the interface toughness also tends to degrade with exposure time [3]. Consequently, over their service life, TBCs are susceptible to delamination along the top and/or bottom TGO interfaces.

Experimental observations [4, 5] have confirmed that in the absence of bond coat creep, delamination at the TGO-bond coat interface leads to buckling instability and failure in TBCs. On a flat interface, the spallation failure is primarily driven by local buckling instability at the delamination site. A significant body of work exists in the literature on this failure mechanism with the details of buckle initiation, propagation, and coalescence [6-9]. A number of these investigations in the literature [7, 8] consider a two layer TBC systems, where the substrate is coated with a bond coat layer and either no ceramic top coat is deposited or the top coat is considered negligible. A widely used

analytical solution for critical buckling load for a circular blister has been developed by Hutchinson and Suo [10], and this solution has been employed to predict buckle initiation in TBCs by Evans *et al.* [11] and He *et al.*[9]. While the analytical model [10] is accurate for very large interfacial delaminations, the predictions incur error for the insipient stages of delamination where the assumed rotational constraints become questionable.

The presence of interfacial waviness dramatically affects failure mechanisms in TBCs. The effect of waviness has been highlighted by Evans *et al.* [11], where a sinusoidal undulation was used to understand the origin of interfacial cracks and by He *et al.* [9], where crack growth along the interface has been associated with periodic and a-periodic morphologies. The onset of failure in elastic TBCs may consequently be viewed as a competition between strain energy driven interfacial delamination growth mechanisms and buckling induced instabilities.

There is also experimental evidence that with significant bond coat creep, damage initiates within the top coat leading to delamination of the top coat and TGO interface [12-14]. Damage within the top coat is primarily driven by the stresses developed due to the coefficient of thermal expansion (CTE) mismatch between the different layers during thermal loading, as well as by creep deformation of the bond coat. In addition to

significant in-plane compressive stresses, the wavy morphology of the top coat and TGO interface results in significant out-of-plane tensile stresses in the top coat. The out-of-plane stresses render the top coat susceptible to cracking in the vicinity of interfacial undulations. During operation the TBC can experience critical loads causing crack initiation within the top coat. During subsequent loading the initial crack may: (a) propagate until it reaches the interface, (b) propagate away from the interface, or (c) be arrested without any subsequent propagation. The cracks that reach the TGO and top coat interface may initiate delamination resulting in failure. The top coat crack initiation and its eventual trajectory in a TBC under operating conditions will depend on the applied loading as well as various geometric and material parameters. Notable among these are important thermo-mechanical properties and geometric and morphological features of the interfaces and the constituent layers. Hence, failure characterization requires establishing a criterion for crack initiation and accurate simulation of the subsequent crack propagation leading to interfacial delamination.

The top coats in real thermal barrier coatings are quite heterogeneous and contain numerous defects within their microstructure. These initial micro-flaws have been postulated to influence TBC failure [15]. The top coat damage may initiate from or be

assisted by the presence of micro-flaws. This makes it imperative to investigate the effects of real top coat microstructure and understand the microstructural interaction with damage evolution. An efficient method to study damage interaction and evolution involves continuum damage mechanics (CDM) [16] theories that represent the cumulative effect of all micro-flaws in the material. A CDM method incorporates the results of the micro-mechanical analyses into the macro-scale model using homogenization [16]. Hence, an accurate simulation of micro-crack propagation along with a reliable damage model is required to study the influence of microstructural defects in TBC top coats.

1.2 SCOPE OF PROPOSED RESEARCH

In the present work, various failure mechanisms responsible for catastrophic delamination of TBCs along susceptible TGO-top coat and TGO-bond coat interfaces are investigated using finite element models. Two independent investigations for defect free TBCs are performed to characterize experimentally observed failure mechanisms based on critical geometric and material parameters. The first investigation uses a finite element model to characterize competing interfacial delamination failure modes (*e.g.* buckling instability and strain energy driven interfacial crack propagation) in linear elastic thermal

barrier coatings. The solution of a linear elastic eigen-value problem determines the onset of the buckling instability with a pre-existing delamination between the bond coat and the TGO. The virtual crack extension method is employed to study strain energy release rate driven interfacial delamination at wavy interfaces. The materials and geometries in the study are chosen to be representative of TBC materials in real applications. Extensive sensitivity analyses are conducted to identify the critical design parameters affecting the onset of buckling and extension of interfacial delamination, as well as to develop parametric relations that enhance the understanding of these mechanisms. Novel parametric relations are derived to predict critical buckling load and energy release rate in three layer TBCs and are compared with existing relations in the literature.

The second investigation uses a thermo-elastic finite element model to study top coat crack initiation and propagation for TBCs with bond coat creep. These cracks are postulated to be responsible for delamination along the top coat and TGO interface. Cracking is assumed to initiate when the maximum principal stress exceeds the rupture stress of the top coat. A sensitivity analysis estimates the contribution of geometric and material parameters and forms the basis for a parametric relation that gives maximum

principal stress. The derived relation delineates the parametric combinations that are susceptible to damage.

Finally, a computational framework is developed to understand the effects of microstructural defects on TBC failure. The framework employs a specialized eXtended Voronoi Cell Finite Element Model (X-VCFEM) [17, 18] to simulate propagation of multiple micro-cracks in conjunction with a homogenized continuum damage model (HCDM) proposed for composite materials by Jain and Ghosh [19]. The range of validity of HCDM for top coat with micro cracks is established using a simple RVE with a single flaw.

1.3 ORGANIZATION OF THIS DISSERTATION

This dissertation has been divided into 6 chapters. In Chapter 2, competing failure mechanisms along TGO-bond coat interfaces are investigated for elastic TBCs. Novel parametric relations based on sensitivity analyses are established for critical parameters. Chapter 2 concludes with a study of the competing buckling and delamination mechanisms for a delamination extending over an undulation. In Chapter 3, parameters influencing top coat damage initiation and propagation are investigated. A parametric domain map is developed to identify fail-safe sub-domains within the multi-dimensional

parametric design space. This investigation is further extended to investigate the influence of top coat cracking on delamination in Chapter 4. A novel relation is also derived to delineating the parametric combinations that are susceptible to failure. In Chapter 5, a framework is developed to characterize the influence of top coat microstructural flaws on damage evolution. A summary of significant contributions towards understanding failure in TBCs and of possible improvements of TBCs are discussed in the concluding chapter.

Each chapter begins with a brief introduction to the essential features analyzed in that chapter. This is followed by main body consisting of theoretical developments and/or numerical results. A brief set of conclusions at the end of each chapter is used to introduce the reader to the next chapter.

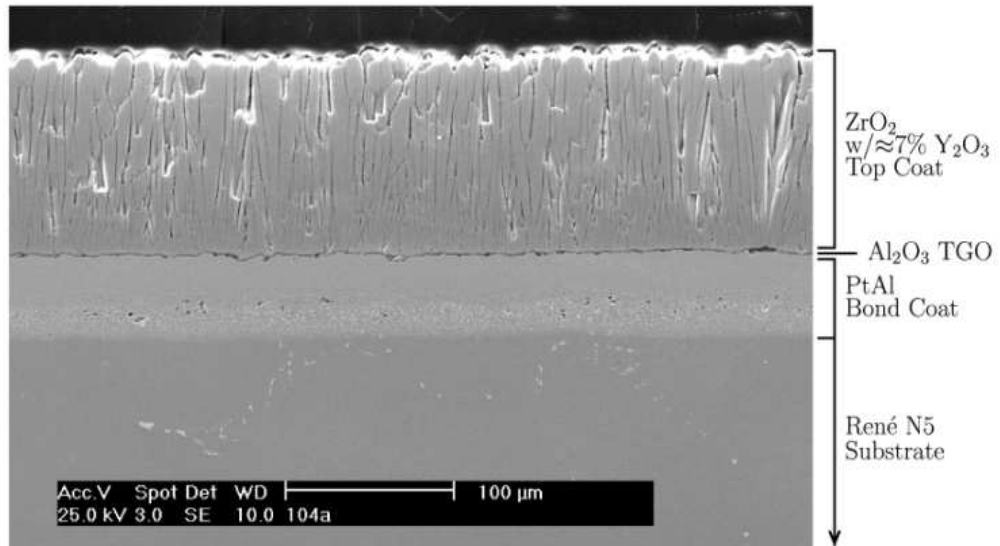


Figure 1.1: A SEM image of the TBC microstructure [20] consisting of the top coat, the thermally grown oxide layer, the bond coat and the super-alloy substrate.

CHAPTER 2

PARAMETRIC STUDIES OF COMPETING FAILURE MECHANISMS IN ELASTIC EB-PVD THERMAL BARRIER COATINGS USING FEM

2.1 INTRODUCTION

The scanning electron microscope (SEM) micrograph of Fig. 2.1 shows a conventional thermal barrier coating (TBC) consisting three layers deposited on a super alloy substrate. The there layers are the bond coat, thermally grown oxide and a ceramic top coat. Individual layers in TBCs are significantly stronger than the inter-layer interfaces. Consequently, over their service life, TBCs are susceptible to delamination and buckling instability. The stresses developed due to the mismatch between coefficient of thermal expansion (CTE) of different layers during thermal loading are the primary driving forces behind the initiation and propagation of TBC damage.

A number of geometrical and mechanical factors are known to contribute to the instability and failure in TBCs. Notable among these are important geometric and morphological features of interfaces and constituent layers, and their thermo-mechanical properties. On a flat interface, the spallation failure is primarily driven by local buckling instability at the delamination site. A significant body of work exists in the literature on this failure mechanism with the details of buckle initiation, propagation, and coalescence [9-11, 21, 22]. The presence of interfacial waviness dramatically affects failure mechanisms in TBCs. This has been highlighted in [11], where a sinusoidal undulation was used to understand the origin of interfacial cracks and in [9], where crack growth along the interface has been associated with periodic and a-periodic morphologies. The onset of failure in TBCs may consequently be viewed as a competition between strain energy driven interfacial crack growth mechanism and buckling induced instability and delamination.

This chapter is aimed at the development of parametric formalism through the numerical study of instability and failure mechanisms in TBC systems by using the finite element method. The closed-form parametric relations are developed assuming that the interfaces can be idealized as planar with intermittent sinusoidal undulations and all the

layers are defect free. The effect of TBC defects on failure are highlighted in [23], such effects however, are not incorporated in the present work since the objective is to develop closed parametric forms. A schematic of the competing damage modes due to pre-existing delamination at the TGO-bond coat interface is shown in Fig. 2.2. The parametric relations are constructed to evaluate critical factors affecting buckling initiation and interface crack extension, as well as to understand the competition between them. These relations will be applicable to all TBC systems with geometric and material parameters within the specified range and not limited to a particular system. The computational model assumes the substrate to be rigid, and excludes its explicit consideration in the deformation and stress analyses. The bond coat and TGO are analyzed using elastic properties, and the model features a pre-existing delamination at the interface of bond coat and TGO. In the sensitivity analysis of candidate parameters, each failure mechanism is studied in isolation from other mechanisms. In the analysis, a linear elastic eigen-value problem is solved as explained in Ansys7.0 [24] to determine the initiation of buckling instability. For estimating the crack propagation at the interface, the energy release rate is determined by the virtual crack extension method based on the stiffness derivative finite element technique proposed by Parks [25].

The chapter starts with a focus on buckling delamination, where the contribution of material and geometric parameters to buckling initiation in two layer TBCs is estimated. A parametric relationship for the critical buckling load in terms of the parameters is developed and compared with existing analytical solutions in the literature for a two layer TBC model. Also the amount of pre-existing delamination that is necessary for the initiation of buckling instability is determined for applied compressive stresses in the TGO. A similar process is also executed for three layer TBCs and compared with the results for the two layer TBC to examine the effect of the top coat. Next, a similar approach is pursued to study strain energy driven delamination at wavy interfaces. A sensitivity analysis is conducted to identify important material and geometric parameters affecting the energy release rate for crack propagation at the interface of single layer and multi layer TBCs. As a final step, the critical values of parameters obtained for competing buckling instability and interface delamination mechanisms are compared, to identify dominant mechanism ranges and to prescribe a fail-safe design space.

2.2 MECHANISMS OF TBC FAILURE AND SOLUTION METHODS

In the context of linear elastic behavior, dominant failure mechanisms in thermal barriers coatings have been identified as the buckling instability and delamination by

crack extension along the interface between the bond coat and TGO [1, 7, 9, 11]. During operation under thermal loads, the TBC can experience critical loads leading to buckling instability and unbounded out-of-plane deflections of the delaminated portion, as shown in the schematic of Fig. 2.2. The buckling instability is eventually arrested at the edge of delamination by the bonded interface. On the other hand, high stress concentrations at the delamination edges can propagate a crack at the interface to increase the extent of delamination. The probability of a particular mode, taking precedence over the other in a TBC under operating conditions, will depend on various geometric and material parameters affecting each mechanism as well as the applied loading. Hence it is of interest to study the dependence of the variables driving these mechanisms on the TBC parameters. A brief introduction to the methods of solution implemented to study these mechanisms is presented next.

2.2.1 BUCKLING INSTABILITY AT FLAT AND WAVY INTERFACES

Irrespective of the interface morphology, the delaminated portion of the TBC is susceptible to buckling instability. In addition to the geometric features and material properties, the nature of the delamination and the critical buckling stresses depend on the contact conditions at the interfaces. A linearized model of elastic stability, using modal

analysis in the commercial FEM code Ansys [24], is incorporated to determine the critical buckling stresses in the TBC system. In this model, the effect of in-plane compressive stresses on the out-of-plane deflection is accounted for by a stress stiffness matrix $[S]$ that augments the conventional stiffness matrix $[K]$. As shown in [24], the $[S]$ matrix is independent of material properties. The stress stiffening matrix $[S]$ is computed from the intensity of the compressive load, referred to as a perturbation stress $\{R\}$, with a linear dependence arising from problem linearity. Assuming that the compressive stress does not change during an infinitesimal change in the buckling displacement $\{\Delta D\}$, the critical load for instability in two contiguous configurations may be equated as [26]:

$$\lambda_{cr}\{R\} = ([K] + \lambda_{cr}[S])\{D\} = ([K] + \lambda_{cr}[S])\{D + \Delta D\} \quad (2.1)$$

where $\{D\}$ is the buckling displacement vector in the reference configuration and λ_{cr} is a scalar multiplier. This is simplified to give the incremental buckling equation as:

$$([K] + \lambda_{cr}[S])\{\Delta D\} = [24] \quad (2.2)$$

Eqn. 2.2 corresponds to a modal analysis problem with $\{\Delta D\}$ as the eigenvector and an associated eigen-value λ_{cr} defining the buckling mode. The block Lanczos eigen-value

extraction method is used in Ansys [24] to determine the lowest eigen-value. Subsequently λ_{cr} is used to scale the far field compressive stress in the TGO to determine the critical buckling stress.

2.2.2 DELAMINATION GROWTH BY CRACK PROPAGATION AT INTERFACES

In the model, the applied load is in a direction parallel to the constituent material layers and their associated interfaces. For this load condition, a crack tip at the delaminated flat interface does not induce a stress concentration to cause crack extension. Consequently, crack growth at the interface between the bond coat and TGO interface is studied exclusively for wavy interfaces. In this study, this mechanism is assumed to be governed by Griffith's energy release rate criterion. According to this criterion, crack growth will occur if the energy required for creating new crack surface area is achieved in the system. The virtual crack extension method, based on the stiffness derivative finite element technique proposed by Parks [25], is used to evaluate the energy release rate. This is determined as the negative of the derivative of the total system potential energy with respect to crack extension. In the finite element model, the potential functional is represented in terms of the global stiffness matrix, the displacement field and the external

loads. The energy release rate G is thus expressed by the stiffness derivative technique [25] as:

$$G = -\frac{\partial U}{\partial a} = -\frac{1}{2}\{\mathbf{D}\}^T \frac{\partial[\mathbf{K}]}{\partial a} \{\mathbf{D}\} \quad (2.3)$$

where $\{\mathbf{D}\}$ is the displacement field, $[\mathbf{K}]$ is the stiffness matrix, and a is the crack length.

G is evaluated numerically from the change in system potential energy per unit crack extension due to a virtual extension of the crack using the relation:

$$G = -\frac{1}{2} \frac{(U_1 - U_2)}{\Delta a} \quad (2.4)$$

where U_1 and U_2 are the respective total potential energies before and after the crack extension by length Δa . A FEM analysis is first conducted with a prescribed length of delamination, and the potential energy U_1 of the system associated with the applied load is calculated. In the second analysis to evaluate U_2 , the finite element analysis is conducted with the crack extended by an infinitesimal length over the initial delamination.

To eliminate the contribution of structural compliance variation due to crack extension, the strain field computed from the first pre-crack extension model is applied to the second analysis. The virtual crack extension is achieved by moving the FE nodes in

the vicinity of the crack tip in the direction of probable crack propagation. The results are sensitive to the region considered as crack tip vicinity and magnitude of crack extension. A very large crack extension may result in distorted elements, whereas, a very small extension may not result in a correct energy release rate. The models used in this study are checked for convergence of the energy release rate with respect to both of these parameters. It is found that variation in energy release rate calculated from the numerical model is within 2% when the nodes associated with at least three layers of nearest and contiguous elements are moved by 1% of the edge length of the elements in close vicinity. The converged values of these parameters are utilized in all subsequent analyses.

2.3 FINITE ELEMENT MODELS OF THE TBC

Various aspects of the finite element model of the TBC with different damage mechanisms are summarized in the following subsections.

2.3.1 MATERIAL PROPERTIES

The EB-PVD TBC system conventionally consists of multiple layers of different materials with distinct interfaces. The substrate is usually a nickel based superalloy with high strength and stiffness, even at elevated temperatures. The bond coat material is often

an inter-metallic platinum modified nickel aluminide with a CTE similar to that of the substrate material. Mechanical properties of the bond coat material may vary with thermal cycling as reported in [27]. The top coat material of choice is yttria stabilized zirconia with a strain tolerant columnar structure. It has been reported [28] that material properties of the top coat vary with deposition process parameters, as well as with the inter-columnar spacing. The mechanical properties of all the layer materials are obtained from those reported in [7, 29, 30] and are listed in Table 2.1. All the materials are assumed to have linear elastic isotropic behavior.

Since the interface is the most likely location for damage, interface toughness in TBCs is of key importance. The interface between the bond coat and the TGO experiences severe stresses due to thermal expansion mismatch and is crucial to TBC durability. The interfacial toughness degrades over time due to segregation (particularly of sulfur) and thermal cyclic loading [9] and cannot be characterized uniquely. Therefore a range for interfacial toughness is assumed in this work, based on two estimates of the interface fracture energy reported by [9]. The range of room temperature fracture energy varies from 10 J-m^{-2} for a diffusion interface to 1 J-m^{-2} for a degraded interface.

2.3.2 GEOMETRIC MODEL AND FINITE ELEMENT MESH

A schematic diagram of the finite element model of the TBC system is shown in Fig. 2.3. Only straight sided and penny-shaped configurations are considered in this work and hence 2D plane strain and axi-symmetric representations of the TBC system are deemed sufficient. The TBC morphology and delamination are assumed to be symmetric about the vertical plane and only the half geometry is modeled. As shown in Fig. 2.3a, the delamination is characterized by a length parameter, which corresponds to a radius in the axi-symmetric case or a width in plane strain. The bond coat-substrate interface is assumed to be relatively stress free, hence the substrate is not explicitly considered in this model. From Fig. 2.1 it can be observed that undulations in the vicinity of planar interfaces between the TGO and bond coat are commonly observed due to the surface roughness of the deposited bond coat. As demonstrated in Fig. 2.4, these undulations may penetrate into the bond coat (type I) or protrude completely into the top coat (type II). Other intermediate scenarios with undulations protruding into adjoining layers in various proportions are also possible. In this study, only sinusoidal undulations that correspond to the limiting configurations of Fig. 2.4 are considered.

The finite element model of a $100 \times 80 \mu\text{m}$ TBC system consist of a mesh of four-noded (QUAD4) elements, identified as PLANE182 in the ANSYS element library [24]. These elements are capable of representing both plane strain and axi-symmetric behavior. The resulting model consist of more than 115,000 elements and 110,000 nodes, and exhibits less than 0.5% error in the strain energy when compared to a more refined mesh. As shown in Fig. 2.3c, a highly refined mesh is used in the vicinity of the crack-tip.

2.3.3 BOUNDARY CONDITIONS

The TBC system model is subjected to a uniform thermal load through a drop in the temperature from $1000 \text{ }^\circ\text{C}$ to room temperature of $30 \text{ }^\circ\text{C}$. The thermal loads caused by this cooling cycle generate compressive stresses in the TGO and top coat on account of CTE mismatch. For all buckling analyses a uniform thermal load creates the perturbation load in the system. Although temperature gradients are expected along the TBC thickness during service, the uniform thermal load assumption is considered adequate, since the critical buckling load is relatively insensitive to the perturbation load. For buckling analysis with planar or wavy interfaces, symmetry boundary conditions are applied at the left edge, roller supports are applied at the lower horizontal boundary to simulate a rigid substrate, and radial periodic boundary conditions are applied at the right edge of the

models. The top surface of the TBC is exposed to the hot gases and is considered to be free of any mechanical constraints. The delaminated region is treated as a contact surface for the wavy interfaces only, and 2D surface contact elements are used in this region.

In the analysis of delamination growth by crack propagation at the wavy interface, symmetry boundary conditions are applied at the left edge, roller supports are applied at the lower horizontal boundary, and radial periodic boundary conditions are applied at the right edge of the models. The delaminated wavy interfaces have contact surfaces and surface contact elements are used in the calculation of energy release rate. Once again, temperature gradients are not considered in these simulations. The growth of delamination occurs primarily during the cooling cycle when the stresses due to CTE mismatch are the highest. The FEM simulations for the energy release rate are performed at room temperature.

2.4 PARAMETRIC MODELING OF BUCKLING INSTABILITY AND INTERFACIAL CRACK EXTENSION

Simulations conducted with the computational models discussed in section 2 are used to derive functional forms of the critical drivers of instability and crack extension induced damage in terms of important geometrical and material parameters in the TBC model.

Sensitivity analyses of these drivers are conducted with respect to the parameters and the results are utilized in the determination of the functional dependence. Prior to the sensitivity analyses, model validation is conducted by comparing results of the simulations with analytical results in the literature.

2.4.1 VALIDATION STUDY OF THE COMPUTATIONAL MODEL

The analytical solution of buckling instability in a two layer TBCs (bond coat and TGO) is provided by Hutchinson and Suo [10]. This work uses classical plate theory (CPT) with clamped edge constraints to obtain an analytical solution for the critical buckling stress:

$$\sigma_b = \left[\frac{\pi^2 E}{12(1-\nu^2)} \right] \left(\frac{h}{R} \right)^2 \quad (2.5)$$

where σ_b is the critical buckling stress, E and ν are the elastic modulus and Poisson's ratio of the TGO, h is the TGO thickness, and R is the dimension of the existing delamination. Solutions of the finite element model are compared with those from Eqn. 2.5. Although there is excellent agreement for $\frac{h}{R} \leq 0.06$, the results show divergence beyond this limit as shown in Fig. 2.5a. The discrepancy arises mainly from the

limitations of the classical linear thin plate theory, implemented in the analytical solution. First, the assumption of a thin TGO in the delaminated region for smaller values of R may not be appropriate for higher (h/R) ratios. Higher order plate theories for thick plates, such as the one proposed in [31], are deemed more appropriate for improved solutions. Secondly, the clamped plate theory with rigid rotational constraints at the edges is not a good approximation at higher values of (h/R) . Since the TGO ligaments remain attached to the bond coat and have a finite stiffness in rotation, the debonded region does not behave as a clamped plate. The contribution and detachment of such ligaments under transverse loading have been discussed in [8]. On the other hand, the computational model captures the physics of the real problem, including the attached ligaments and rotational stiffness of the edges.

A special procedure is invoked to implement a higher order theory with elastically restrained edges in a more accurate representation of the analytical solution. It is observed that the computationally predicted buckling loads are within the extreme bounds of the Reddy plate theory calculations in [32] with zero and infinite rotational stiffness. The rotational stiffness for the TBC system is calibrated through a comparison

of the results of FEM simulations with the available analytical solutions [32]. The relation between Kirchhoff load and Reddy buckling load is given [32] as:

$$N^R = \frac{N^K \left(1 + \frac{N^K}{70Gh} \right)}{\left(1 + \frac{N^K}{(14/17)Gh} \right)} \quad (2.6)$$

where G is the shear modulus and N^R and N^K represent the Reddy and Kirchhoff buckling loads, respectively. Assuming the load N^R to be equal to the buckling load predicted by FEM solutions, N^K is solved from Eqn. 2.6. The rotational stiffness parameter $\frac{K_r R}{D}$ is then evaluated from the unified Kirchhoff equation [32]

$$\sqrt{\frac{N^K R^2}{D}} J_0 \left(\sqrt{\frac{N^K R^2}{D}} \right) + \left(\frac{K_r R}{D} - (1-\nu) \right) J_1 \left(\sqrt{\frac{N^K R^2}{D}} \right) = 0 \quad (2.7)$$

where $D = \frac{Eh^3}{12(1-\nu^2)}$ is the flexural rigidity, R is the radius of the plate, and J_0 and J_1 are the Bessel functions of first kind of order zero and one, respectively. The value of rotational stiffness parameter is then used in Eqn. 2.7 to obtain N^K for different values of R . Subsequently, the value of the buckling load may be evaluated from Eqn. 2.6 for different values of (h/R) in the range $(0 \leq \frac{h}{R} \leq 1)$. Fig. 2.5b shows that the results obtained by this analytical model with higher order theory and finite rotational stiffness are in

close agreement with the numerical results for values of $\frac{h}{R} \leq 0.2$. However, significant errors are still incurred at higher values of (h/R) . This may be attributed to the use of a single data point used in the calibration of the rotational stiffness parameter and the assumption that it remains constant throughout the entire range of (h/R) . While limited studies have investigated plate buckling with different rotational stiffness [32-34], an established relationship between the rotational stiffness and the thickness, size, and modulus is lacking in the literature. Hence, the development of functional relations for buckling load for a larger range of (h/R) is pursued in this study. Such a functional form is needed, as large ratios are expected at the incipient stages of delamination formation and it is not known *a priori* whether the buckling instability initiates at such small delamination lengths.

2.4.2 CRITICAL STRESS ANALYSIS FOR BUCKLING INSTABILITY IN THE TBC

The critical buckling load or stress is dependent on a number of geometric and material parameters of the TBC system, as well as on the applied loads. Deriving functional forms of the critical buckling loads in terms of the critical parameters is a desirable, yet non-trivial exercise. Simplified forms of such relations have been provided in [9-11, 35]. In this study, these relations are extended for more comprehensive

accounting of the range of critical parameters. The relations are first developed for the two layered TBCs (bond coat and TGO) and subsequently extended to three-layered TBCs (bond coat, TGO, and ceramic top coat).

2.4.2.1 Two layer TBC system model

The first analysis is for a two-layered TBC with a planar interface. In order to identify the critical parameters entering the function, a sensitivity study of buckling load with respect to geometric and material parameters of the two layers is conducted for both plane strain and axi-symmetric conditions. Candidate parameters for this study are selected based on buckling characterization studies in the literature [1, 9, 22, 30]. The parameters considered in the sensitivity analysis are: (i) L , length of the TBC model length, (ii) h , thickness of the TGO, (iii) b , thickness of the bond coat, (iv) E_{TGO} , stiffness of the TGO, (v) E_{BC} , stiffness of the bond coat, and (vi) R , length of the pre-existing delamination. Definitions of the geometric parameters are pictorially given in Fig. 2.3a.

In the FEM simulations of the TBC system for sensitivity analyses, a single parameter is varied at a time while keeping all others fixed. The results of the sensitivity analyses are summarized in Figs. 2.6a, b where the normalized critical buckling stress is plotted as a function of the normalized geometric and material parameters, respectively. The critical

buckling stresses for each case are normalized with respect to the corresponding maximum critical buckling stresses, *i.e.*, $S^{max}=30.24$ GPa for the geometric parameters study and $S^{max}=0.52$ GPa for the material parameters study, respectively. Each parameter is normalized with its maximum value considered in this work, *i.e.*, $L^{max}=1000$ μm , $b^{max}=100$ μm , $h^{max}=50$ μm , and $R^{max}=1000$ μm for geometric parameters and $E_{TGO}^{max}=600$ GPa and $E_{TC}^{max}=300$ GPa for material parameters. Fig. 2.6a shows very little influence of the overall model length L or the bond coat thickness b on the critical stress. The critical buckling stress decreases rapidly with increasing delamination length R before stabilizing at near zero critical buckling stress values. The critical stress variation is found to fit an inverse quadratic relation with the delamination length. When the two layers are completely delaminated ($R=L=1000$ μm), the critical stress is equal to the buckling stress in a single layer. Finally, the critical stress increases nonlinearly with the TGO thickness h . The dependence is quadratic for lower TGO thicknesses, but for thicker TGOs the relation is more complex.

Fig. 2.6b summarizes the results of the sensitivity analyses with respect to the elastic moduli of the constituent materials of the TBC system. While the buckling stress is generally insensitive to the bond coat modulus, it reduces slightly (~8%) for a very

compliant bond coat of approximately 1/20 of TGO modulus. For a compliant bond coat it is easier for the TGO to buckle at lower loads. This effect becomes significant when the modulus of bond coat is appreciably less than that of the TGO, as discussed in [36]. For a compliant bond coat, the energy released from the bond coat has also been shown [37] to be much more than the energy stored in the TGO. The numerical model captures the reduction in critical stress for very compliant bond coat as predicted by analytical models [36, 37]. The buckling stress is linearly dependent on the TGO modulus. When compared to plane strain delamination analyses, the sensitivity analyses for axi-symmetric delamination yields a self-similar functional dependence with a higher value for the critical stress.

2.4.2.2 Parametric Representation of the Critical Stress for Buckling Instability

The sensitivity analysis forms a basis for the development of a parametric representation of the critical buckling stress σ_{TGO}^{b2} in terms of the important parameters for the two-layer TBC system. From the summary of results in Fig. 2.6, the critical parameters identified are the TGO thickness h , TGO modulus E_{TGO} and the interfacial delamination size R . Furthermore, it is also observed that a dependence of σ_{TGO}^{b2} on the (h/R) ratio best represents the influence of individual parameters h and R . This

observation is also consistent with dimensional analysis. These analyses point to a

functional form for the buckling stress as $\sigma_{TGO}^{b2} \propto E_{TGO} f\left(\left(\frac{h}{R}\right)^n\right)$ where n is a constant to

be determined. A similar parametric dependence has been discussed in [9, 11] as

$$\sigma_{TGO}^{b2} = \begin{cases} 0.81 E_{TGO} \left(\frac{h}{R}\right)^2 & \text{Plane Strain} \\ 1.21 E_{TGO} \left(\frac{h}{R}\right)^2 & \text{Axisymmetric} \end{cases} \quad (2.8)$$

These relations are based on the thin plate theory and consequently they have limited range of validity. It has been pointed out in [31] that classical plate theory is valid for $0.0 < \left(\frac{h}{R}\right) \leq 0.05$, and the range of applicability is confirmed in the current FEM simulations as well. As shown in Fig. 2.5a, the analytical predictions are within 3% of the FEM results at $\left(\frac{h}{R}\right) = 0.06$. However, at higher (h/R) values, the two predictions diverge rapidly. For plane strain, the differences are 13%, 81% and 320% at (h/R) ratios of 0.2, 0.5 and 1.0, respectively. For the axi-symmetric case, the differences are 30%, 120% and 350%, respectively. From the present study, it is clear that σ_{TGO}^{b2} representation using a single continuous function of the parameters is very difficult.

Consequently, in the development of parametric relations for an extended range of validity, the range $0.0 < \left(\frac{h}{R}\right) \leq 1.0$ is divided into four segments. Each segment is determined from the nature of $\sigma_{TGO}^{h^2}$ dependence on the (h/R) ratio. Exclusive validity ranges are associated with each functional form to avoid non-unique solutions for any geometric configuration. For both the plane strain and axisymmetric cases, the first sub-domain corresponds to the range of validity of Eqns. 2.8 derived by Evans *et al.* [11] and He *et al.* [9]. The functional relations for the subsequent regions are obtained by a least squares based “best fit” analysis of the FEM solutions with an error tolerance of 3.5%. The parametric relations are summarized in Eqns. 2.9 and 2.10. Excellent agreement of these relations with the finite element results for the axisymmetric case is demonstrated in Fig. 2.7.

$$\sigma_{TGO}^{h^2} = \begin{cases} 0.8100E_{TGO}\left(\frac{h}{R}\right)^2 & \forall \quad 0.00 < \left(\frac{h}{R}\right) \leq 0.06 \\ 0.4655E_{TGO}\left(\frac{h}{R}\right)^{1.8} & \forall \quad 0.06 < \left(\frac{h}{R}\right) \leq 0.21 \\ 0.2765E_{TGO}\left(\frac{h}{R}\right)^{1.45} & \forall \quad 0.21 < \left(\frac{h}{R}\right) \leq 0.50 \\ 0.2050E_{TGO}\left(\frac{h}{R}\right) & \forall \quad 0.50 < \left(\frac{h}{R}\right) \leq 1.0 \end{cases} \quad (\text{plane strain}) \quad (2.9)$$

$$\sigma_{TGO}^{h^2} = \begin{cases} 1.2100E_{TGO} \left(\frac{h}{R}\right)^2 & \forall \quad 0.00 < \left(\frac{h}{R}\right) \leq 0.06 \\ 0.6800E_{TGO} \left(\frac{h}{R}\right)^{1.8} & \forall \quad 0.06 < \left(\frac{h}{R}\right) \leq 0.21 \\ 0.3887E_{TGO} \left(\frac{h}{R}\right)^{1.45} & \forall \quad 0.21 < \left(\frac{h}{R}\right) \leq 0.50 \\ 0.2753E_{TGO} \left(\frac{h}{R}\right) & \forall \quad 0.50 < \left(\frac{h}{R}\right) \leq 1.0 \end{cases} \quad (\text{axisymmetric}) \quad (2.10)$$

These parametric equations do not suffer from the restrictive assumptions of the analytical solutions [9-11] and represent a wide range in the context of linear elasticity. It should be noted that the ranges of the (h/R) ratio are kept the same for both the plane strain and axisymmetric cases. Also, the exponents and the functional forms are kept the same with only differences in the coefficients. The distinct forms in different ranges result in discontinuities at the edges of the (h/R) ranges. The discontinuity errors are tabulated in Table 2.3 and are found to be within established limits. The slightly higher errors for the axisymmetric case are due to the fact that the range and exponents are kept the same as for the plane strain case.

2.4.2.3 Three layer TBC system model

The parametric form is subsequently extended for a three-layered TBC system consisting of the bond coat, TGO, and ceramic top coat with planar interfaces. A

sensitivity analysis of the critical buckling load for this model is performed under plane strain assumptions only. In addition to h and R , the parameters include the top coat thickness (t) as shown in Fig. 2.3a, and the modulus (E_{TC}). Experimental observations [1, 28, 30] have motivated the consideration of the range of variation of t to be $\sim 1-50 \mu\text{m}$ and of E_{TC} to be $\sim 1-200$ GPa. Fig. 2.8a summarizes the results of the sensitivity analysis with respect to t , h and R . In this analysis, $E_{TC} = 100$ GPa, the normalizing top coat thickness $t^{\text{max}} = 50 \mu\text{m}$ and the normalizing stress $S^{\text{max}} = 137$ GPa. The critical buckling stress increases sharply at lower values of the top coat thickness before stabilizing at a value that is significantly higher than the corresponding two-layer critical stress. This result concurs with the multi-layer analytical model predicting similar characteristics developed in [21]. Two important observations can be made from the plots in Fig. 2.8a. The stabilized critical stress depends on the TGO thickness h and is insensitive to the delamination size R . On the other hand, the rate of increase of the critical stress at lower values of t is inversely dependent on R and is insensitive to h . The magnification in S/S^{max} due to the addition of the top coat reduces with increasing (h/R) ratios (~ 4 for $h/R=0.4$ and ~ 2 for $h/R=0.8$). Furthermore, Fig. 2.8b shows a quadratic dependence of S/S^{max} on the elastic modulus E_{TC} for a fixed $(h/R)=0.4$.

A process similar to that discussed for the two-layer TBC is followed to obtain a functional relation for critical buckling stress in the three-layer TBC. This functional relation reduces that in Eqn. 2.9 in the limit that t is equal to zero. Using a least squares based “best fit” analysis of the FEM solutions with an error tolerance of 4%, this relation may be express as:

$$\sigma_{TGO}^{b3} = \sigma_{TGO}^{b2} + \left(\frac{h}{R}\right)^{-0.45} \left(1 - e^{\left(c_1 \frac{t}{R}\right)}\right) \left(C_2 \frac{E_{TC}^2}{E^*} + C_3 E_{TC}\right) \quad \forall \quad 0.25 \leq \left(\frac{h}{R}\right) \leq 1.0 \quad (2.11)$$

where σ_{TGO}^{b3} and σ_{TGO}^{b2} are the critical TGO stress for three and two layer TBCs respectively, $E^* = 1$ GPa (necessary for dimensional consistency) and C_1 , C_2 and C_3 are constants. The constants are determined using the best fit analysis as: $C_1 = 1.115$, $C_2 = -1.33E-3$ and $C_3 = 0.746$. Eqn. 2.11 predicts the critical stress to within 4% of the FEM results for most parametric variations. However larger differences are found for $\left(\frac{h}{R}\right) < 0.25$ with maximum error 7.3% for $(h/R) = 0.2$ and hence, this formula is not recommended for such geometric configurations. Also top coats that are thinner than the TGO, *i.e.* $t < h$, are physically unlikely and are not considered in Eqn. 2.11. This parametric form significantly improves the understanding of buckling instability in linearly elastic multi-layered TBCs and maybe used as a fail-safe design tool.

2.4.3 ESTIMATING ENERGY RELEASE RATE FOR INTERFACIAL CRACK

EXTENSION

It has been discussed in section 2.2, that the presence of a wavy TGO-BC interface induces high transverse stresses perpendicular to the interface. Stress concentrations near the edge of a delamination may cause the delamination to extend, a phenomenon that is governed by the strain energy release rate. As shown in [22], this energy release rate in turn is influenced by various geometric and material parameters. Hence, it is desirable to develop comprehensive functional forms depicting the relation between the energy release rate and the critical parameters in TBC systems. Simplified parametric relations for two-layer TBCs have been provided in [9, 11], among others, and for three-layer TBCs in [21]. However, these relations mainly address cracks propagating from undulations and exclude scenarios where the cracks propagate towards an interfacial undulation from a planar delaminated interface. The latter situation is considered in this chapter with a realistic range of critical parameters.

The configurations in Fig. 2.4 describe the two limiting cases of wavy interfaces with undulations, protruding into alternate constituent layers. The type I undulation configuration penetrates the bond coat while the type II undulation configuration

protrudes into the top coat. Finite element models of the two configurations with sinusoidal undulations are used for stress analysis in the 3-layer TBC system without any pre-existing delamination. The analyses conclude that the type I undulations induce tensile transverse stresses at the junction of planar and wavy interfaces, whereas the type II undulations induce compressive transverse stress at the same location as shown in the contour plots of Fig. 2.4. Consequently, the type I undulation configuration is chosen for developing parametric forms of the energy release rate. Only the plane strain case is considered in this study.

The first case considered in the development of the functional dependence is where the delamination is on the verge of extending into the wavy portion of the interface. Subsequently, the delamination is incrementally extended into the undulation and the variation of energy release rate is studied. A sensitivity analysis is done for the three-layer TBC system to assess the influence of critical parameters on the energy release rate G . Candidate parameters for this analysis are selected from results of characterization studies reported by [7, 21, 22, 30]. They are the: (i) TGO thickness (h), (ii) top coat thickness (t), (iii) length of the pre-existing delamination (R), (iv) amplitude of the sinusoidal undulation (A), (v) undulation wavelength (W) (vi) TGO stiffness (E_{TGO}), (vii)

bond coat stiffness (E_{BC}) (viii) top coat stiffness (E_{TC}), and (ix) far-field thermal mismatch stresses σ_{TGO} and σ_{TC} in the TGO and the top coat, respectively. The ranges of each parameter are selected based on experimental observations in [2, 21, 38-41] and are listed in table 4. The far-field stress in a layer is evaluated as $(\alpha_{layer} - \alpha_{substrate})\Delta T$, where α is the coefficient of thermal expansion and ΔT is the temperature change from the stress free state. Since the far field stress is a linear function of ΔT , its variation is achieved by simply reducing the applied uniform temperature in a range from 900°C to 30°C, assuming that 1000°C is the stress free temperature.

The sensitivity analysis is carried out by varying a single parameter at a time. The analysis shows highly nonlinear dependence of the energy release rate G on some parameters like h , A , and W . More variations of these nonlinear parameters are considered in the sensitivity simulations. The energy release rate G is calculated by the virtual crack extension method discussed in section 2.2. Results of the sensitivity analysis are summarized through plots of the variation of the normalized energy release rate G/G^{max} with normalized geometric and material parameters in Figs. 2.9 and 2.10. For each plot, G^{max} is calculated from the FEM analyses and the normalizing parameters are $h^{max} = 6 \mu\text{m}$, $t^{max} = 15 \mu\text{m}$, $E_{TGO}^{max} = 480 \text{ GPa}$, $E_{TC}^{max} = 80 \text{ GPa}$, $E_{BC}^{max} = 280 \text{ GPa}$, $A^{max} = 10$

μm , $W^{\text{max}}=30\ \mu\text{m}$, and $R^{\text{max}}=35\ \mu\text{m}$. Fig. 2.9a shows that G/G^{max} varies inversely with t , prior to stabilizing at a constant value. It also shows a non-linear dependence for lower values of h . Fig. 2.9b shows that G/G^{max} has a strong dependence on E_{TC} and E_{TGO} , increasing linearly with E_{TGO} and decreasing asymptotically with E_{TC} . However, it is relatively insensitive to E_{BC} and is only about 7% smaller than the maximum value for a very compliant bond coat ($E_{BC}^{\text{min}} \sim 100\ \text{GPa}$). Hence E_{BC} is excluded from the expression of the parametric relation. Fig. 2.10 shows the sensitivity of G/G^{max} with respect to the geometric parameters of the undulation. It has an inverse non-linear dependence on the wavelength (W) and a non-linear dependence on the amplitude (A). The influence of the delamination size (R) is relatively weak. Also G/G^{max} is found to be very sensitive to the far field stresses σ_{TGO} and σ_{TC} with quadratic dependences as shown in Fig. 2.10(b).

2.4.3.1 Parametric Representation of the Energy Release Rate

Based on their influence on the energy release rate G , the critical parameters are re-classified into four basic groups and the sensitivity study results are used to establish their functional relations. The functional relation for each group is expressed in Table 5. The constant values h_0 , t_0 , R_0 , E^* and c_n (for $n=1-10$) in these relations are determined by using the least square fit with data generated by FEM simulations. These functions are

subsequently combined to derive a functional dependence form of the energy release rate

as:

$$G \propto f_1(h, A, W) f_2(t) f_3(R) f_4(\sigma_{TGO}, E_{TGO}, \sigma_{TC}, E_{TC}) \quad (2.12)$$

This combined function is constrained to have a zero value, when: (i) the system is stress free, (ii) the TGO and the top coat thickness or their elastic moduli reduce to zero simultaneously (*i.e.*, $h=t=0$ or $E_{TGO}=E_{TC}=0$), (iii) there is no delamination ($R=0$) and (iv) there is no interfacial undulation in the vicinity of the delamination ($A=0$ or $W=\infty$). The energy release rate should not become zero when only one of the TGO or top coat thicknesses or moduli reduces to zero (*i.e.*, $h \neq t=0$ or $E_{TGO} \neq E_{TC}=0$). From these constraint considerations, the energy release rate functional form is derived to be

$$G = (\tan^{-1} \psi)^{C_1} \left(C_2 t e^{-C_3 \frac{t}{t_0}} - C_4 \frac{h^2}{h_0} + C_5 h \right) \left(1 - e^{-C_6 \frac{R}{R_0}} \right) \xi \sigma_{TGO}^2 \quad (2.13)$$

where $\psi = \left(\frac{2\pi A + 3h}{W} \right)$, $\xi = \left(C_7 \frac{1}{E_{TGO}} + C_8 \frac{(\alpha_{TC} - \alpha_{BC})^2 E_{TC}}{(\alpha_{TGO} - \alpha_{BC})^2 E_{TGO}^2} e^{-C_9 \frac{E_{TC}}{E^*}} \right)$, $t_0=1 \mu\text{m}$, $h_0=1$

μm , $R_0=1 \mu\text{m}$, $E^*=1 \text{ GPa}$, $(\alpha_{layer} - \alpha_{BC})$ is the CTE mismatch of the layers and $C_1 - C_9$ are

constants. The constants in Eqn. 2.13 are evaluated using a least squares based best fit

analysis of the FEM results with a tolerance of 10%. For stresses and moduli expressed in GPa, lengths in μm , and the energy release rate in Joules/m^2 , the constants are derived to be: $C_1=3.62$, $C_2=2.02 \times 10^3$, $C_3=0.92$, $C_4=17.83$, $C_5=427.97$, $C_6=0.14$, $C_7=1.10$, $C_8=111.25$ and $C_9=0.12$. This relation is found to predict energy release rate to within 6% of the all simulation results for a wide range of parametric variations. Only for TBC systems with a very thin top coat (*i.e.* $t < 10 \mu\text{m}$), the maximum error is relatively high and $\sim 10\%$. Larger differences between FEM results and the predicted values are also found when the amplitude (A) is significantly less than the TGO thickness (h), which are taken to be out of the validity range for this relation.

An alternate mechanism of crack propagation has been suggested in [42] for flat interfaces. This requires an interfacial delamination to originate from the root of a vertical cleavage crack penetrating through the top coat and the TGO. An analytical solution for steady state energy release rate at such an edge delamination has been derived [42] as:

$$G_{ss} = \frac{\sigma_{TGO}^2 h_{TGO} (1-\nu^2)}{2E_{TGO}} + \frac{\sigma_{TC}^2 h_{TC} (1-\nu^2)}{2E_{TC}} - \sum_{i=TGO,TC} \frac{1}{E_i} \left[\frac{P^2}{h_i} + \frac{12M_i^2}{h_i^3} \right] \quad (2.14)$$

$$\text{with } P = \frac{E_{TC} h_{TC}^2}{6} \kappa, \quad M_i = \frac{E_i \kappa h_i^3}{12} \quad \text{and} \quad \kappa = \frac{3(\epsilon_{TGO} - \epsilon_{TC})}{2h_{TC} \left[1 + \frac{E_{TC} h_{TC}}{4E_{TGO} h_{TGO}} \right]}$$

where σ_i and ε_i denote the expansion mismatch stress and strain, h_i denotes thickness, E_i is the elastic modulus of the respective layers and ν is the Poisson ratio of the TGO and the top coat. It is demonstrated [42] that G_{ss} for such a delamination can reach very high values and grow even for fairly tough interfaces. Fig. 2.11 shows a comparison of G from Eqn. 2.13 with G_{ss} from Eqn. 2.14 for a TBC with 10 μm thick top coat. In the vicinity of a significant undulation, G exceeds the value of G_{ss} . Despite predicting comparable energy release rates for specific configurations, there are several notable differences between the functional forms of Eqns. 2.13 and 2.14. These are as follows.

(i) The energy release rate at an edge delamination in Eqn. 2.14 increases almost linearly with top coat thickness (t). However, for the case of a delamination in the vicinity of an interfacial undulation, G decreases exponentially before stabilizing at a constant value. This difference may be attributed to the symmetry constraint imposed on the detached bi-layer that limits it from acquiring a curvature comparable to that of the edge delamination. The sensitivity analysis predicts that this constraint increases with increasing top coat thickness and elastic modulus, before stabilizing at a constant value. This characteristic difference reveals that for a thicker top coat, the prediction of higher G_{ss} by Eqn. 2.14 is more appropriate than that by Eqn. 2.13.

(ii) Eqn. 2.14 shows that at an edge delamination, both the detached layers have comparable contribution to the energy release rate, whereas Eqn. 2.13 suggests that near an undulation the TGO layer contribution outweighs the exponentially decreasing contribution of the top coat. Hence, the stress state in the TGO layer is more critical for the G of delamination near undulations.

For any given geometric configuration and materials properties, the energy release rate reaches a critical value G^c when the far field stress in the TGO reaches a critical value (σ_{TGO}^c). The corresponding parametric equation for the critical TGO stress is obtained from Eqn. 2.13 as:

$$\sigma_{TGO}^c = \left[\frac{G^c}{(\tan^{-1} \psi)^{C_1} \left(C_2 t e^{-C_3 \frac{t}{t_0}} - C_4 \frac{h^2}{h_0} + C_5 h \right) \left(1 - e^{-C_6 \frac{R}{R_0}} \right) \xi} \right]^{0.5} \quad (2.15)$$

Eqn. 2.15 reveals that for delamination growth, σ_{TGO}^c varies inversely with TGO thickness and with the delamination size. The critical stress σ_{TGO}^c also varies with the inverse of the CTE mismatch, and hence a larger mismatch will assist delamination. The CTE mismatch should therefore be minimized to extend TBC life.

As an extension to the present sensitivity analysis, the energy release rate is determined for an interfacial delamination extending into the undulation region. Fig. 2.12 shows that the energy release rate increases as the delamination extends over the first quarter of the undulation wave and then reduces to minimum (G^{min}) at the beginning of the last quarter. Comparing the values at the beginning and end of the entire undulation period, it is seen that G ends up higher after the delamination has extended over an undulation. This observation confirms its dependence on the delamination length as predicted by the sensitivity analysis. From this study it is apparent that for any undulation, if G^{min} exceeds interface strength, delamination may extend completely over it.

2.5 COMPETITION BETWEEN BUCKLING AND CRACK EXTENSION MODES

The parametric forms of Eqns. 2.11 and 2.15 predict the critical stresses σ_{TGO}^{b3} and σ_{TGO}^c for buckling instability and interface crack extension respectively, in a three-layer TBC. For any given configuration, material and load condition, the critical stress can therefore be determined for each mechanism. A comparative analysis using these equations can determine optimal configurations for the TBC system from a fail-safe point

of view. Such a comparison is clearly limited to the delamination approaching an undulation from a flat interface.

To study the competition between these failure mechanisms as the delamination extends over an undulation, a FEM model of a representative TBC configuration is set up with the following parameters: $h=1 \mu\text{m}$, $t=5 \mu\text{m}$, $A=4 \mu\text{m}$, $W=20 \mu\text{m}$, $R=30 \mu\text{m}$, $E_{TC}= 40 \text{ GPa}$ and $E_{TGO}= 400 \text{ GPa}$. Since the delaminated wavy surfaces can come in contact and alter the buckling mode shape as well as G , these surfaces are modeled using contact elements in the FE model. The competition of the two modes is best understood from the results of the simulations in the form of the graphical representation in Fig. 2.13. The critical stress σ_{TGO}^{cw} at which G exceeds the critical interface energy G^c in Eqn. 2.15 is compared with the critical buckling stress σ_{TGO}^{bw} . The four plots represent the energy release rates G for a temperature drop from 1000 °C to room temperature (30 °C), for four different locations of the crack tip as shown in Fig. 2.13b. The vertical dotted lines represent the critical buckling stress σ_{TGO}^{bw} corresponding to the four crack tip locations, while the dashed horizontal lines enclose the range of possible interfacial fracture energies for such configuration from the data given in [35]. For a weak interface with fracture energy 1 J/m², σ_{TGO}^{cw} is lower than σ_{TGO}^{bw} for all configurations and loading

conditions, and hence delamination dominates. The competition is more pronounced for a strong interface (fracture energy = 10 J/m²) and is investigated for crack tip locations **a**, **b**, **c** and **d** in Fig. 2.13b. The selection of these locations is based on the variation of G with crack advance shown in Fig. 2.12. As the delamination approaches the undulation wave at location **a**, σ_{TGO}^{cw} marginally exceeds buckling stress and the crack will extend to location **b** where the slope of the undulation reverses. At location **b**, σ_{TGO}^{cw} reduces considerably but σ_{TGO}^{bw} is slightly higher due to the thicker bending cross-section. Consequently, the crack extends to location **c** where σ_{TGO}^{cw} is expected to be maximum. The buckling instability dominates here since σ_{TGO}^{bw} is significantly lower than σ_{TGO}^{cw} . Beyond location **c**, σ_{TGO}^{cw} is expected to reduce but a comparison at location **d** shows σ_{TGO}^{bw} is slightly lower than σ_{TGO}^{cw} and hence buckling still dominates. From these numerical results, it is apparent that buckling instability is most likely to occur when the delamination is either at a planar interface or reaches the last quarter of an undulation. For other cases, interfacial crack extension mode dominates, especially when the undulation amplitude is significant.

2.6 CONCLUSIONS

In this chapter, characteristics of failure modes *e.g.* buckling instability and strain energy driven interfacial crack propagation at interfacial delamination in linear elastic thermal barrier coatings (TBCs) are investigated using a finite element model. The solution of a linear elastic eigen-value problem determines the onset of the buckling instability with a pre-existing delamination between bond coat and the TGO. The virtual crack extension method is employed to study strain energy release rate driven interfacial delamination at wavy interfaces. The materials and geometries in the study are chosen to be representative of TBC materials in real applications. Extensive sensitivity analyses are conducted to identify the critical design parameters affecting the onset of buckling and extension of interfacial delamination, as well as to develop parametric relations that enhance the understanding of these mechanisms. These novel parametric relations, that extend the range of applications of the functional dependence found in literature, are validated with existing relations in the literature.

The chapter concludes with a numerical exercise studying the competing mechanisms as the delamination extends over an undulation. It is demonstrated that the buckling instability is the leading failure mechanism at flat interfaces or near the locations of

minimum cross-section in a wavy interface. However, in the vicinity of waviness, crack extension can become a dominant mode of failure. The probability of a particular mechanism taking precedence over the other depends on various geometric and material parameters and the nature of the loading. A comparative study of the predicted critical buckling stress with critical delamination stress can identify the dominant mechanism. The highlights of studies with these parametric relations are summarized below.

The critical buckling stress relationships for two-layer TBCs has an extended range of validity and better accuracy for incipient stages of buckling instability as compared to the existing analytical solutions in the literature [9, 11]. The effect of the top coat is realized through its inclusion in the three-layer TBC model. The critical stress for this model is found to strongly dependent on the top coat geometry and material, in addition to the relevant two layer model parameters. The effect of the top coat thickness is found to stabilize with increasing thickness.

The parametric form for the critical stress initiating interfacial crack extension at the delamination in a three-layer TBC is vital for understanding the effect of interface morphology on the failure mechanism. Furthermore, it is helpful in quantitatively establishing criteria for dominant failure mechanisms.

The parametric relations can be used by designers as a helpful tool in the design of reliable TBCs in thermo-mechanical applications. The life of TBCs can be prolonged through an optimal combination of geometric and material parameters that suppresses the dominant mechanism.

Although the present study illustrates the competition between the failure mechanisms in detail, the validity is limited to the linear elastic TBCs. The failure modes will be further influenced by the material non-linearity of the constituent layers, cyclic thermal loading and residual stresses, and this is the subject of next chapter.

Property	Substrate	Bond coat	TGO	TBC
Poisson's Ratio	0.31-0.35	0.30-0.33	0.23-0.25	0.10-0.12
Elastic modulus (GPa)	120-220	110-200	320-400	0-100
Thermal expansion coefficient ($10^{-6} / ^\circ\text{C}$)	14.8-18.0	13.6-17.6	8.0-9.6	9.0-12.2

Table 2.1. Material properties of components of the TBC system as obtained from [7, 29, 30]

h/R	FEM	Free Edges	Clamped Edges
0.2	10.16	5.64	17.7

Table 2.2. Critical buckling load comparison with results in [32]

h/R ratio	Discontinuity error (%)	
	Plane Strain	Axisymmetric
0.06	0.87	1.35
0.22	0.90	2.9
0.50	1.25	3.25

Table 2.3. Discontinuities in the values of σ^b at the edges of each h/R ratio range in the parametric Eqns. 2.9 and 2.10.

Parameter	Range of Variation
TGO thickness (h)	1-6 μm
Undulation amplitude (A)	5-10 μm
Undulation wavelength (W)	10-30 μm
Interfacial delamination (R)	5-70 μm
Top coat modulus (E_{TC})	10-100 GPa
TGO modulus (E_{TGO})	260-480 GPa
Bond coat modulus (E_{BC})	150-280 GPa

Table 2.4. Range of variation of parameters from experimental observations [2, 21, 38-41] for energy release rate study. All combinations of A and W , outside of the range $0.3 < \frac{A}{W} < 0.5$ are excluded.

Function of (Parameters)	Functional Relation to G
$f_1(h, A, W)$	$\left(c_1 \frac{h^2}{h_0} + c_2 h + c_3 \right) \left(\tan^{-1} \left(\frac{2\pi A + 3h}{W} \right) \right)^{c_4}$
$f_2(t)$	$c_5 t e^{-c_6 \frac{t}{t_0}} + c_7$
$f_3(R)$	$c_6 \left(1 - e^{-c_7 \frac{R}{R_0}} \right)$
$f_4(\sigma_{TC}, E_{TC}, \sigma_{TGO}, E_{TGO})$	$\left(c_8 \frac{\sigma_{TGO}^2}{E_{TGO}} + c_9 \frac{\sigma_{TC}^2}{E_{TC}} e^{c_{10} \frac{E_{TC}}{E^*}} \right)$

Table 2.5. Functional relation between energy release rate and critical parameters, based on sensitivity analysis using FEM simulations. The values h_0 , t_0 , R_0 , E^* and c_n ($n=1-10$) are constants that are determined using the least square fit technique.

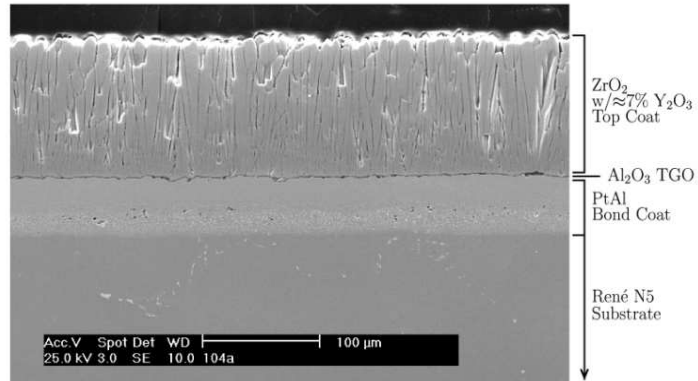


Figure 2.1: A SEM image [20] of the TBC microstructure consisting of the top coat, the thermally grown oxide layer, the bond coat and the super-alloy substrate.

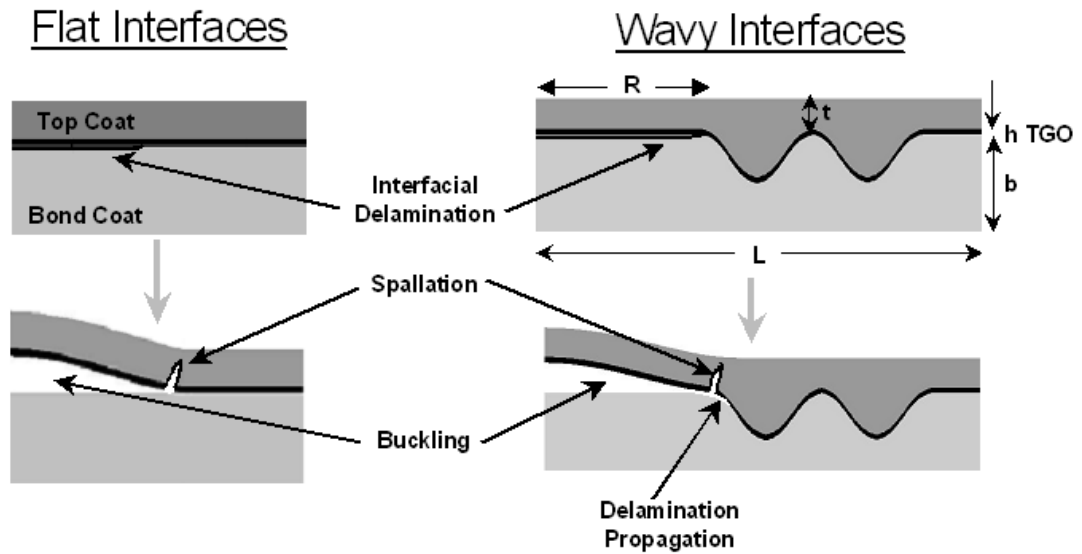


Figure 2.2: Schematic diagrams showing the competing failure mechanisms in TBC systems with flat and wavy interfaces.

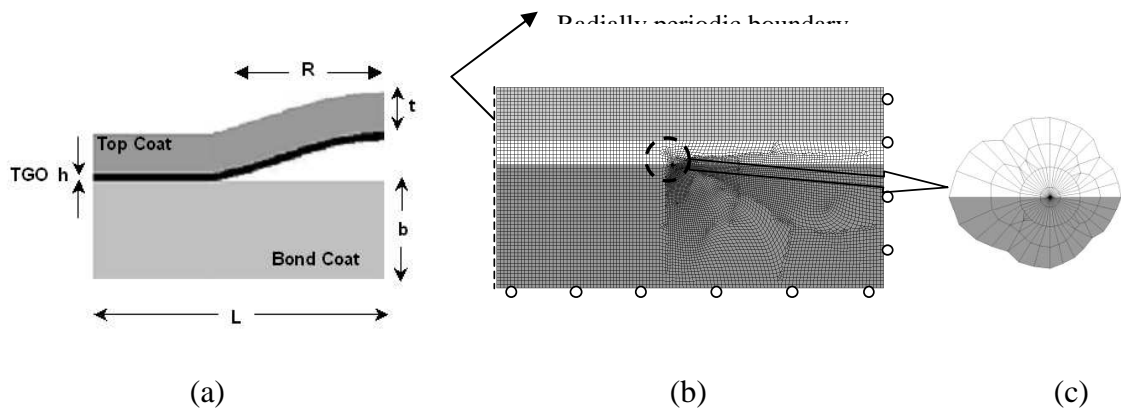


Figure 2.3: Schematic diagrams showing (a) geometric and dimensional parameters (b) finite element model of the TBC system with bond coat lower interface rigid, symmetry at vertical edge of delamination (right) and radial periodicity at the vertical edge of the bonded part (left) (c) close-up of the mesh at the crack tip.

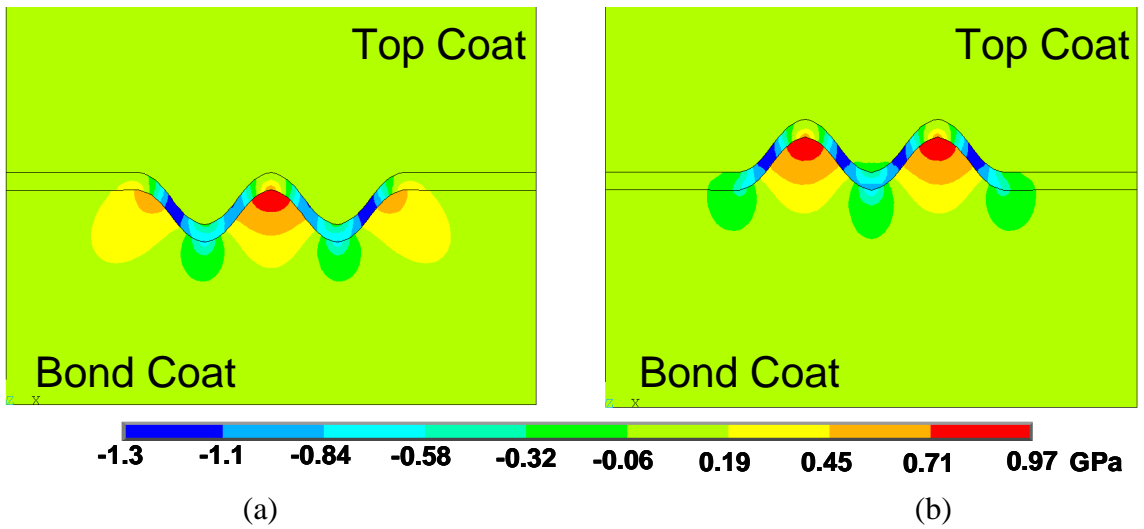
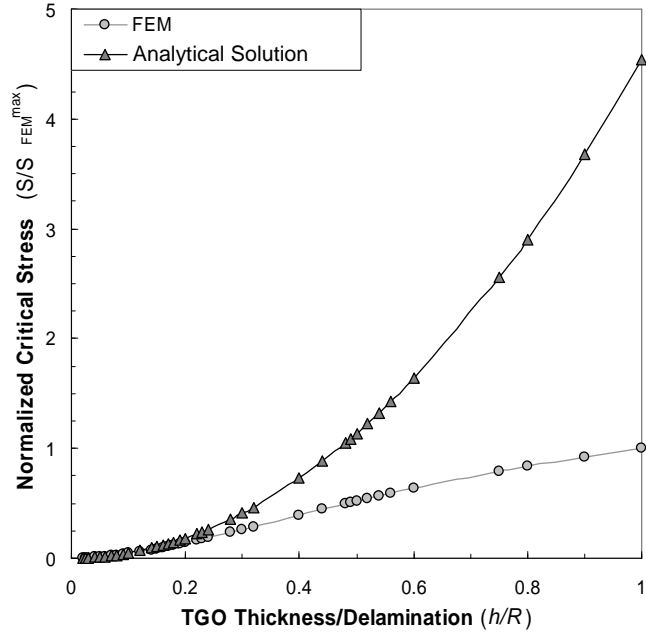
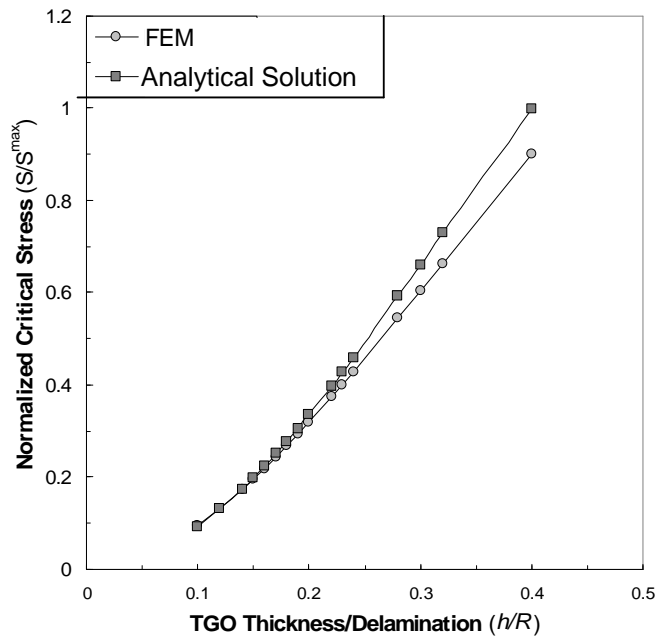


Figure 2.4: Contour plots showing transverse stress (GPa) at fully bonded wavy interfaces for (a) Type I undulation penetrating completely into the bond coat; (b) Type II undulation protruding completely into the top coat.

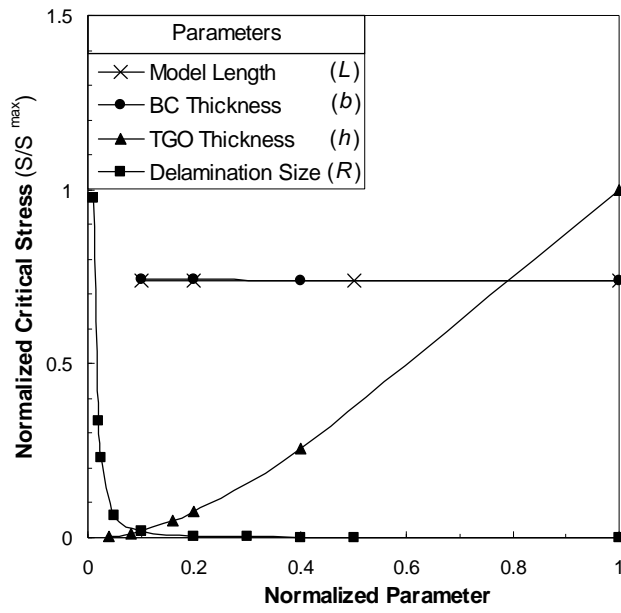


(a)

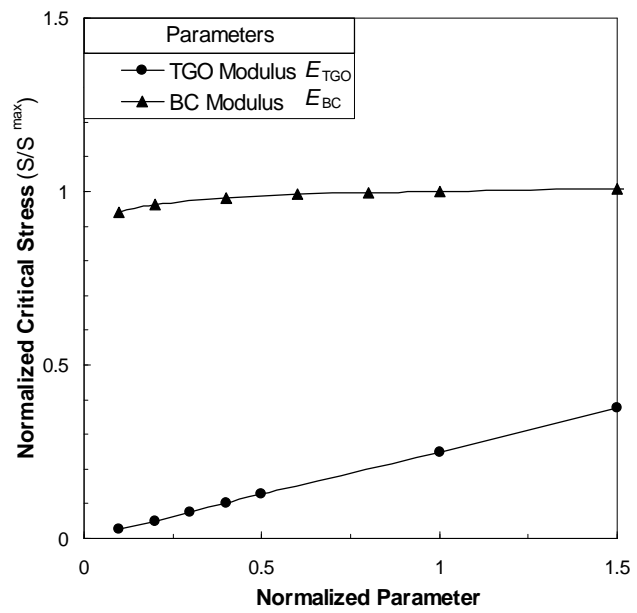


(b)

Figure 2.5: Plots showing (a) the comparison between the finite element results and a low order analytical solution [10] where normalizing stress $S^{max}=110$ GPa, (b) comparison of finite element results and a higher order analytical solution [43] where normalizing stress $S^{max}=46$ GPa



(a)



(b)

Figure 2.6: Plots for the two layer TBC, showing critical buckling load sensitivity to (a) geometric parameters (normalizing values of $L^{max}=1000 \mu\text{m}$, $b^{max}=100 \mu\text{m}$, $h^{max}=50 \mu\text{m}$, $R^{max}=1000 \mu\text{m}$, and $S^{max}=30.2 \text{ GPa}$), and (b) material parameters (the normalizing values of $E_{BC}^{max}=600 \text{ GPa}$, $E_{TGO}^{max}=600 \text{ GPa}$, and $S^{max}=0.52 \text{ GPa}$).

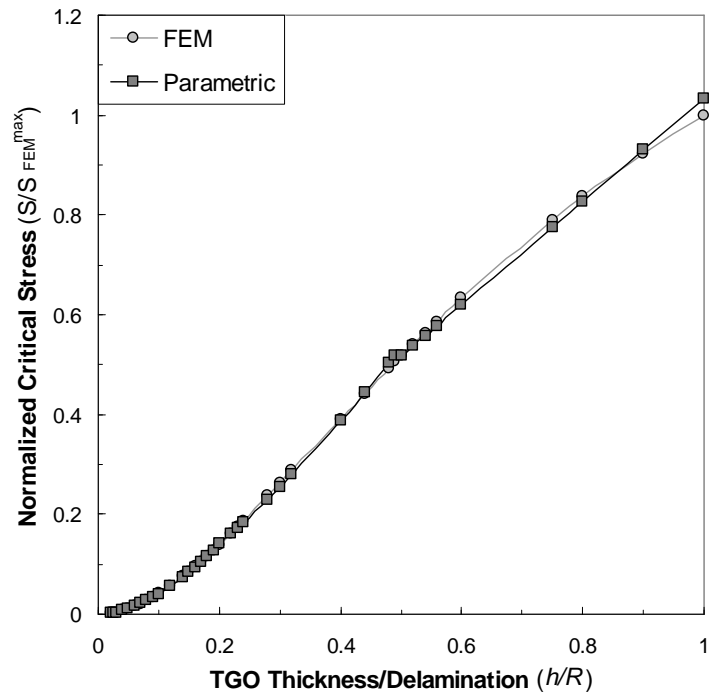
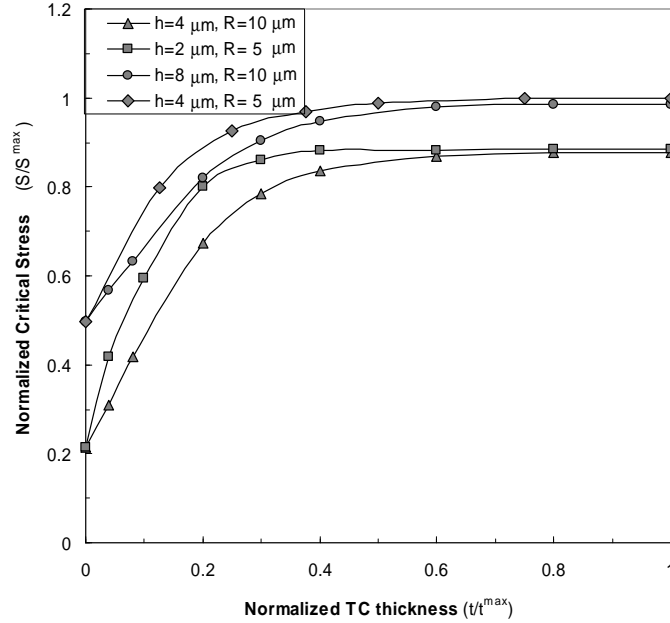
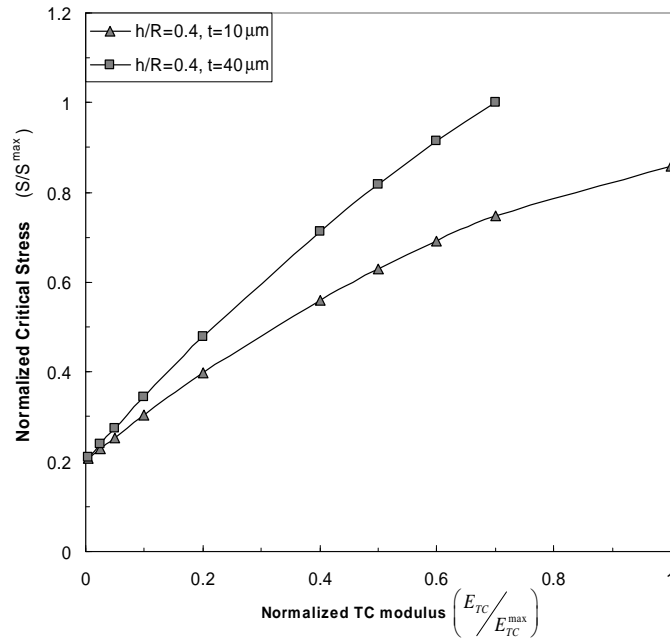


Figure 2.7: Plots of the critical buckling stress as a function of h/R ratio for the two layer TBC, obtained with the parametric relations and finite element solution for the axisymmetric case (normalizing stress $S_{FEM}^{max} = 110$ GPa).

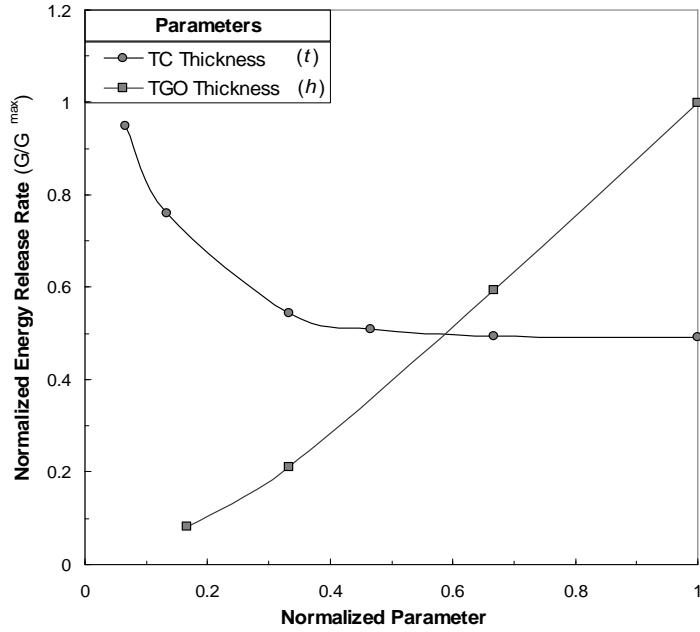


(a)

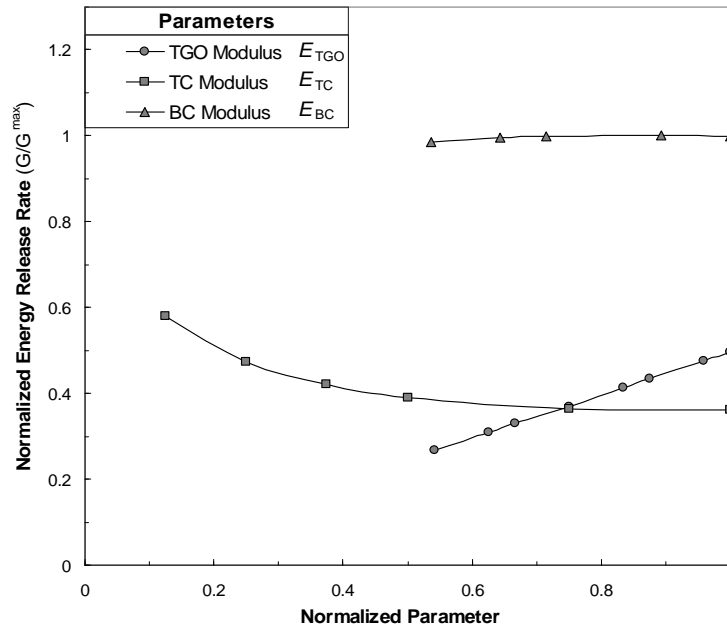


(b)

Figure 2.8: Plots for the three layer TBC, showing the variation of normalized critical buckling stress with (a) top coat thickness (t) (normalizing values: $S^{\max} = 137$ GPa and $t^{\max} = 50 \mu\text{m}$.) and (b) top coat modulus E_{TC} (normalizing values: $S^{\max} = 147$ GPa and $E_{TC}^{\max} = 200$ GPa).

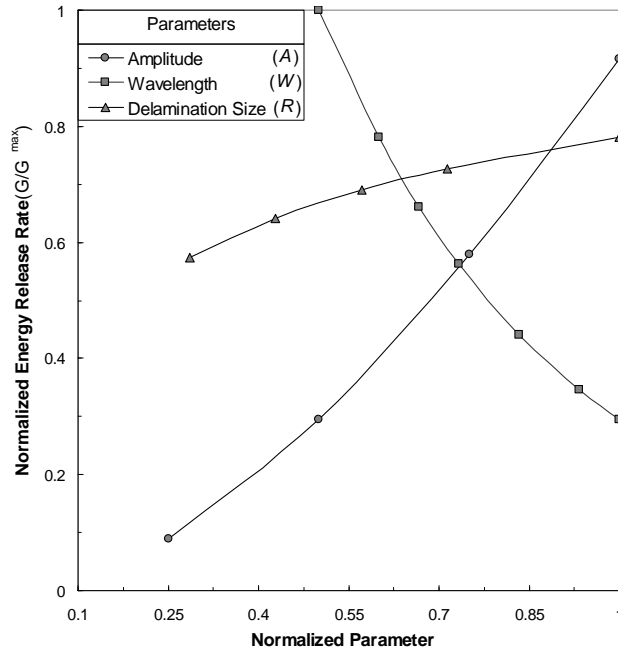


(a)

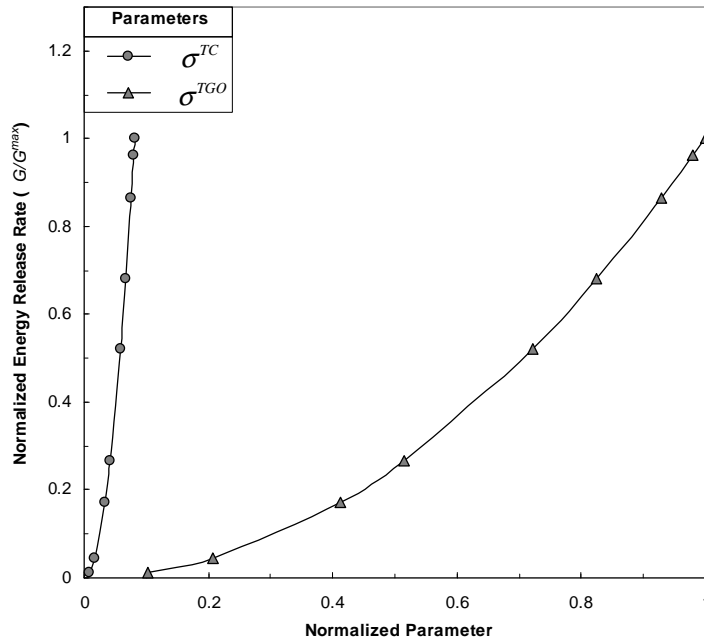


(b)

Figure 2.9: Plot showing the sensitivity of G with respect to (a) geometric parameters (normalizing measures are: $h^{\max} = 6 \mu\text{m}$, $t^{\max} = 15 \mu\text{m}$, and $G^{\max} = 22 \text{ J/m}^2$); and (b) material parameters (normalizing measures are: $E_{TGO}^{\max} = 480 \text{ GPa}$, $E_{TC}^{\max} = 80 \text{ GPa}$, $E_{BC}^{\max} = 280 \text{ GPa}$, and $G^{\max} = 12 \text{ J/m}^2$).



(a)



(b)

Figure 2.10: Plot showing the sensitivity of the energy release rate with respect to (a) undulation parameters (normalizing factors are $A^{\max} = 6 \mu\text{m}$, $W^{\max} = 30 \mu\text{m}$, $R^{\max} = 35 \mu\text{m}$, and $G^{\max} = 16 \text{ J/m}^2$), (b) expansion mismatch stress in the TGO and top coat (normalizing factors are $\sigma^{\max} = 2.2 \text{ GPa}$ and $G^{\max} = 4.6 \text{ J/m}^2$).

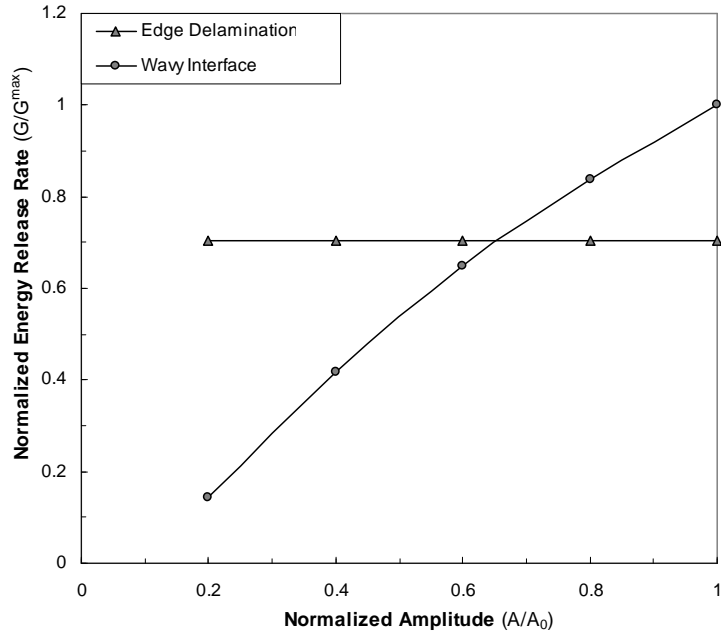


Figure 2.11: Plot showing the comparison of energy release rate (G) near an interfacial undulation with the steady state energy release rate (G_{ss}) at an edge delamination [42] for $h/R=0.2$, $t=10 \mu\text{m}$, $W=30 \mu\text{m}$ and $\sigma_{TGO}=2.17 \text{ GPa}$ (normalizing factors: $A_0=10 \mu\text{m}$, $G^{max}=52 \text{ J/m}^2$).

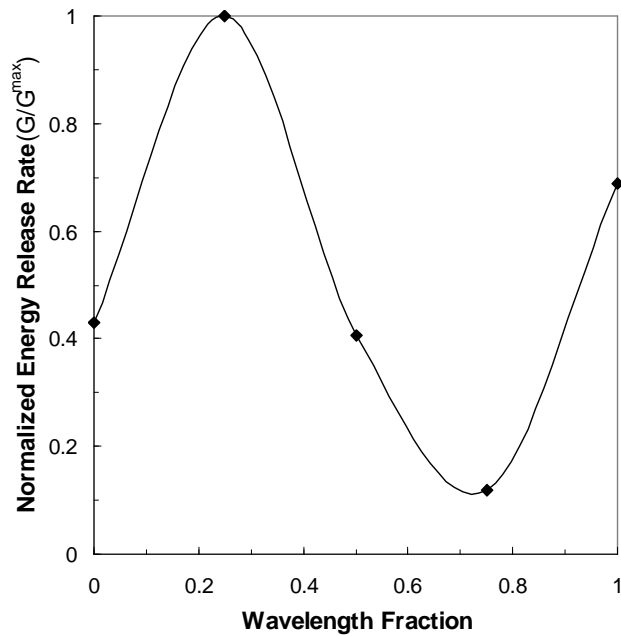
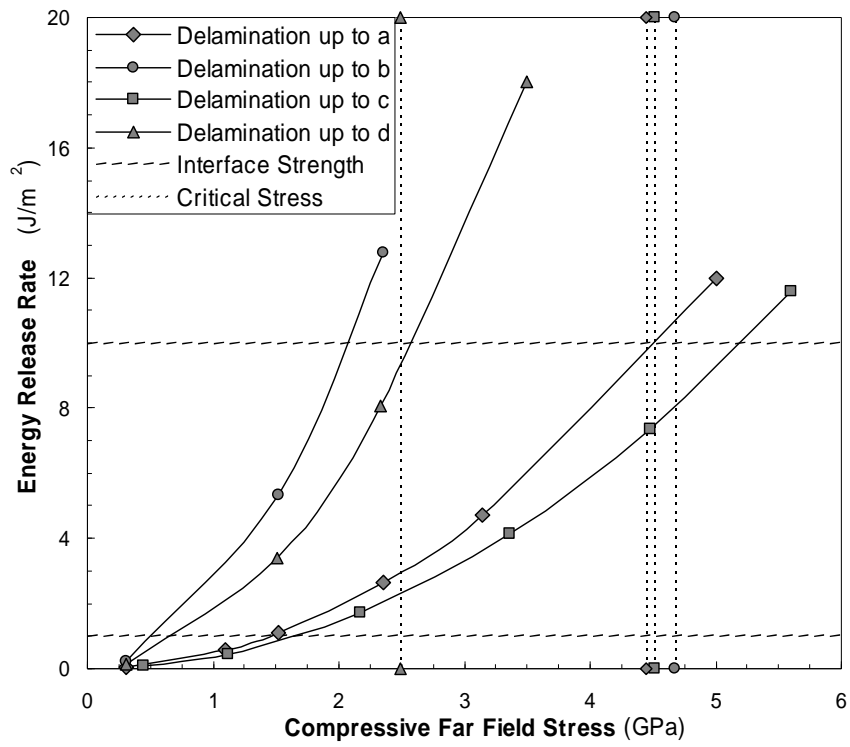
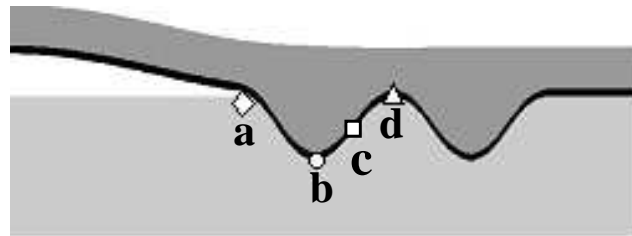


Figure 2.12: Plot showing the variation of the normalized energy release rate as the interfacial crack propagates along an interfacial undulation for $W=20 \mu\text{m}$, $A=4 \mu\text{m}$ and $G^{max}=21 \text{ J/m}^2$.



(a)



(b)

Figure 2.13: Plot showing (a) the competition between buckle initiation and interface crack extension, (b) the corresponding locations for energy release rate curves and for study of the competition between buckling and delamination propagation.

CHAPTER 3

A PARAMETRIC DOMAIN MAP FOR TOP COAT DAMAGE INITIATION AND PROPAGATION IN EB-PVD THERMAL BARRIER COATINGS

3.1 INTRODUCTION

Experimental observations [4, 5] confirm that in the absence of significant bond coat creep, delamination is predominantly along TGO and bond coat interface. TBC spallation is preceded by a competition between buckling and interface delamination that is stimulated by the waviness of the interface. The competing mechanisms have been extensively investigated in the literature [6-9] and were recently formalized parametrically to enable identification of the dominant failure mechanism for TGO and bond coat delamination [6].

There is also evidence that with significant bond coat creep, damage initiates within the top coat leading to delamination of top coat and TGO interface [12-14, 44]. Damage

within the top coat is primarily driven by the stresses developed due to the coefficient of thermal expansion (CTE) mismatch between the different layers during thermal loading, as well as by creep deformation of the bond coat. A number of geometrical and mechanical factors are known to contribute to the damage initiation and propagation within the top coat. Notable among these are important geometric and morphological features of interfaces and constituent layers, and their thermo-mechanical properties.

A significant body of work exists in the literature characterizing the growth of undulations under cyclic loading [12, 13, 44]. A number of these investigations also consider the top coat damage [12, 13], but the relationship between damage and geometric and material factors has not been addressed in detail. Xu *et al.* [14] have demonstrated the variation in energy release rate as the crack propagates within the top coat for crack paths that were selected *a priori*.

This chapter is aimed at the development of parametric domain maps delineating safer TBC system designs from those prone to failure. The multi-dimensional parametric space is represented as a reduced order 2-D parametric domain map for the crack initiation in terms of the critical geometric parameters. This map is created through parametric finite element simulations that include the substrate, bond coat, TGO and the

top coat. The crack path is not postulated *a priori*; instead, crack initiation and its subsequent trajectory is determined based on the local drivers at the crack tip. A sensitivity analysis is employed to first estimate the contribution of material and geometric parameters to crack initiation. Subsequently, sensitivities to parameters responsible for crack initiation are investigated through crack propagation simulated with a hysteretic cohesive zone model.

The development of domain map enables the realization and selection of geometric parameters that result in a safer TBC. As a final step, based on the predictions of the parametric domain map that incorporates crack initiation followed by crack propagation, two representative failure scenarios are simulated. The geometry and material properties for these cases are obtained from the literature and the predicted crack trajectories are found to be in good agreement with experimental observations in the literature [4, 7]. The models developed in this work are micromechanical in nature with explicit damage representation at the micromechanical scale of the TBC. However, the implications of the model are macroscopic, in that it is used to predict overall reliability of EB-PVD TBCs.

3.2 THE TOP COAT FAILURE MECHANISMS AND SOLUTION APPROACH

In the context of linear elasticity, TBCs are insensitive to cyclic loading and the failure mechanisms are limited to TGO interfaces [7-9]. However, incorporating bond coat creep introduces significant non-linearity to the TBC response under cyclic loading and also activates an alternate failure mechanism reported by Evans *et al.* [7] and Karlsson *et al.* [12]. During operation under cyclic thermal loads, the TBC can experience critical loads causing crack initiation within the top coat and at the site of interfacial undulations. During subsequent cycles of loading the initial crack may: (a) propagate until it reaches the interface, (b) propagate away from the interface or (c) be arrested without any subsequent propagation. The probability of crack initiation and its eventual trajectory in a TBC under operating conditions will depend on various geometric and material parameters as well as the applied loading. Hence, it is of interest to study the influence of TBC parameters on initiation and propagation of top coat cracks. A brief introduction to the methods used to study the initiation and propagation of cracks is presented next.

3.2.1 CRACK INITIATION WITHIN THE TOP COAT

In addition to significant in-plane compressive stresses caused by its thermal expansion mismatch with the substrate, the top coat is also subjected to out-of-plane tensile stresses due to the wavy morphology of the top coat and TGO interface. This renders the top coat susceptible to cracking in the vicinity of interfacial undulations. Since the material of choice is brittle Yttria stabilized Zirconia (YSZ), the top coat cracking is likely to initiate in Mode I. A Mode I crack initiation criterion similar to [45] is employed where damage appears as a finite crack oriented normal to principal direction, when, as given in Eqn. 3.1, the maximum of first principal stress ($S1^{max}$) exceeds rupture stress ($\sigma_{rupture}$):

$$S1^{max} \geq \sigma_{rupture} \quad (3.1)$$

Crack initiation is sensitive to the rupture stress rather than fracture energy, hence even though the top coat and TGO interface toughness is lower than the bulk top coat the rupture stress is assumed to be invariant. It enables identification of safer TBC designs through a sensitivity analysis to determine relationship of $S1^{max}$ on various geometric and material parameters. The parameters considered for this study are shown pictorially in

Fig. 3.1 and include: a) top coat modulus (E_{TC}), b) TGO modulus (E_{TGO}), c) TGO thickness (h), d) amplitude (A) and wavelength (W) of the undulation, and e) thermal cycle parameters including peak temperature and heating, holding, and cooling time. Since the resulting crack is oriented normal to the principal direction for Mode I fracture, the orientation of the principal axis is recorded so that propagation of a nascent crack can be studied.

3.2.2 PROPAGATION OF CRACKS ORIGINATING WITHIN THE TOP COAT

The top coat may incur cracks due to local tensile stresses at the sites of interfacial undulations, however, not all cracks will contribute to the large scale failure of TBC. The critical cracks that required further investigation are those that propagate with each load cycle and reach the interface. Since the cracks that reach the interface will initiate delaminations, it is of interest to understand their sensitivity to the various parameters. In recent years cohesive zone models have emerged as important tools for modeling crack propagation in homogeneous and heterogeneous materials [17, 46-49]. Cracking is simulated by inserting special cohesive elements between continuum elements (*e.g.*, [46, 47, 49]) The use of a highly refined computational mesh, especially near the crack tip is also a requirement, even though the effect is mitigated due to the finite crack tip stresses

provided by the cohesive zone. In this chapter, a state of the art cohesive zone model is employed along with a criterion for crack path evolution determined by the local crack tip state, thus eliminating the mesh-dependent prediction of crack path even with a structured mesh. These computational tools are described in next two subsections.

3.2.2.1 Hysteretic mixed-mode cohesive element formulation

Due to the cyclic nature of the thermal loading, TBCs may incur significant fatigue damage within the top coat leading to crack coalescence and failure. The hysteretic cohesive models proposed by Nyugen *et al.* [50] and Maiti and Guebelle [51] are found to be suitable for such failure but they are limited to Mode I loading. Although top coat cracks are assumed to initiate under Mode I loading, they may experience mixed mode loading as they extend along complicated trajectories. Hence, for TBC application, a hysteretic cohesive model is extended to mixed mode loading that reduces to an irreversible bi-linear, rate-independent cohesive law under monotonic loading [48, 51].

The bi-linear cohesive model is discussed in detail elsewhere *e.g.*, [48] and is summarized by the following traction-separation law:

$$T = \begin{cases} \frac{\sigma_{\max}}{\delta_c} \delta & \text{if } \delta < \delta_c \text{ (hardening region)} \\ \frac{\sigma_{\max}}{\delta_c - \delta_e} (\delta - \delta_e) & \text{if } \delta_c < \delta < \delta_e \text{ (softening region)} \\ 0 & \text{if } \delta > \delta_e \text{ (completely debonded)} \end{cases} \quad (3.2)$$

The effective separation and effective traction are defined as $\delta = \sqrt{\delta_n^2 + \beta^2 \delta_t^2}$ and $T = \sqrt{T_n^2 + \beta^{-2} T_t^2}$, respectively, where δ_n and T_n are the normal separation and traction, δ_t and T_t are the tangential separation and traction and β is an empirical factor. As the effective separation increases, the effective traction across the elements reaches a maximum value (σ_{\max}) at δ_c , and then decreases for further increase in separation. This increase in traction δ is known as hardening. The subsequent decrease is known as softening, which introduces irreversibility through monotonic decay of the peak stress due to damage. At a selected effective separation (δ_e) the tractions vanish, indicating the failure of the element.

Regardless of whether the element is in the hardening or soften region, the unloading is always assumed to be towards the origin of the traction–separation curve. Thus, the bi-linear cohesive model remains fully reversible within the hardening region. Once it enters the softening region ($\delta \geq \delta_c$), any subsequent unload/reload occurs with reduced stiffness, rendering the deformation irreversible. Upon reloading it returns to the state at

the beginning of unload, and additional monotonic damage can be accrued upon further loading.

To account for dissipative mechanisms in the fracture process zone ahead of the crack tip, a hysteretic model incurs fatigue damage only during reloading. This damage can occur at any point, including when the element is in the so-called hardening region. Unloading is still assumed to be linearly towards the origin of traction-separation curve, and therefore hysteresis curves are formed. During reloading the stiffness of the cohesive element is assumed to decay according to the stiffness degradation given below in Eqn. 3.3. The rate of stiffness decay is controlled by the introduction of an additional parameter δ_f .

$$\begin{aligned} \dot{K}_{nn} &= \begin{cases} -K_{nn}^p \frac{\dot{\delta}_n}{\delta_f} & \text{if } \dot{\delta}_n > 0 \\ 0 & \text{if } \dot{\delta}_n \leq 0 \end{cases} \\ \dot{K}_{tt} &= \begin{cases} -K_{tt}^p \frac{\dot{\delta}_t}{\delta_f} & \text{if } \dot{\delta}_t > 0 \\ 0 & \text{if } \dot{\delta}_t \leq 0 \end{cases} \end{aligned} \quad (3.3)$$

These incremental stiffness equations are converted to difference equations to calculate the stiffness at the $(p+1)^{th}$ step based on the stiffness of the p^{th} load step and increment in displacement jump. The resulting normal and tangential stiffness are:

$$\begin{aligned}
K_{nm}^{p+1} &= K_{nm}^p e^{\frac{\Delta\delta_n}{\delta_f}} & \text{where } \Delta\delta_n &= \delta_n^{p+1} - \delta_n^p \\
K_{tt}^{p+1} &= K_{tt}^p e^{\frac{\Delta\delta_t}{\delta_f}} & \text{where } \Delta\delta_t &= \delta_t^{p+1} - \delta_t^p
\end{aligned} \tag{3.4}$$

Due to the incremental nature of fatigue damage, increments in normal and tangential tractions are calculated using the following equation:

$$\begin{pmatrix} \dot{T}_n \\ \dot{T}_t \end{pmatrix} = \begin{bmatrix} K_{nm} & 0 \\ 0 & K_{tt} \end{bmatrix} \begin{pmatrix} \dot{\delta}_n \\ \dot{\delta}_t \end{pmatrix} \tag{3.5}$$

Using the backward Euler method, the normal and tangential tractions at the $(p+1)^{th}$ step are evaluated using the updated stiffness as given in Eqn 3.6.

$$\begin{aligned}
T_n^{p+1} &= T_n^p + K_{nm}^{p+1} \Delta\delta_n \\
T_t^{p+1} &= T_t^p + K_{tt}^{p+1} \Delta\delta_t
\end{aligned} \tag{3.6}$$

The hysteretic response of the cohesive model remains within the envelope of the bilinear model, and when the reloading curve intersects the softening curve it follows the curve for as long as the loading process continues. During such periods the element accrues only monotonic damage without any fatigue damage. From the above formulation, it can be seen that five cohesive zone parameters namely, σ_{\max} , δ_c , δ_e , δ_f and β define the hysteretic cohesive zone response. Fig. 3.2 graphically

illustrates, the traction-separation response of the hysteretic cohesive model under cyclic loading.

3.2.2.2 Incremental direction of crack propagation

The crack trajectory cannot be determined *a priori* as it depends on the local drivers at the crack tip. This makes it imperative to evaluate the direction of crack propagation at each increment of loading as the crack is restricted to follow the trajectory defined by the cohesive zone elements. The following are among the numerous methods proposed in the literature to evaluate incremental direction: maximum circumferential stress $\sigma_{\theta\theta}^{\max}$ criterion (Erdogan and Sih [52]), maximum energy release rate criterion-MERR (Palaniswamy and Knauss [53]), and strain energy density criterion (Sih [54]). In the present work direction is determined using the maximum cohesive energy criterion proposed by Li and Ghosh [17]. This criterion postulates that the crack will propagate in the direction that maximizes the available cohesive energy. From the definition of the J-Integral, a relation between the cohesive energy ϕ for complete decohesion and the critical energy release rate G_c has been established in [47] as:

$$G_c = J = \int_0^R T \frac{\partial \delta}{\partial x} dx = \int_0^{\delta_c} T d\delta = \phi \quad (3.7)$$

where R is the length of the cohesive zone. Consequently, for a given crack tip state of stress, the crack growth direction is estimated as that along which G_c or equivalently the cohesive energy ϕ is maximized. The cohesive energy ϕ_A at the crack tip A along any direction α can be expressed for an arbitrary effective separation $\delta(\alpha)$ as:

$$\phi_A(\alpha) = \left(\int_0^{\delta(\alpha)} T(\alpha) d\delta \right)_A = \left(\int_0^{t(\alpha)} T(\alpha) \cdot \frac{\partial \delta}{\partial t} dt \right)_A \quad (3.8)$$

where $T(\alpha) = \sqrt{(T_n^{coh})^2 + \beta^{-2} (T_t^{coh})^2}$ is the magnitude of the effective cohesive traction.

The corresponding unit normal n and tangential t vectors along the direction α are expressed as:

$$n = -\sin \alpha i + \cos \alpha j \quad , \quad t = \cos \alpha i + \sin \alpha j \quad (3.9)$$

The normal and tangential components of the cohesive traction force at an angle α are then deduced as:

$$\begin{Bmatrix} T_n^{coh} \\ T_t^{coh} \end{Bmatrix} = \begin{bmatrix} n_x & n_y \\ t_x & t_y \end{bmatrix} \begin{Bmatrix} \sigma_{xx} n_x + \sigma_{xy} n_y \\ \sigma_{xy} n_x + \sigma_{yy} n_y \end{Bmatrix} = \begin{Bmatrix} \sigma_{xx} \sin^2 \alpha + \sigma_{xy} \sin 2\alpha + \sigma_{yy} \cos^2 \alpha \\ -\frac{1}{2} \sigma_{xx} \sin 2\alpha + \sigma_{xy} \cos 2\alpha + \frac{1}{2} \sigma_{yy} \sin 2\alpha \end{Bmatrix} \quad (3.10)$$

and hence the effective cohesive traction for direction α is:

$$T(\alpha) = \sqrt{(\sigma_{xx} \sin^2 \alpha - \sigma_{xy} \sin 2\alpha + \sigma_{yy} \cos^2 \alpha)^2 + \beta^{-2} \left(-\frac{1}{2} \sigma_{xx} \sin 2\alpha + \sigma_{xy} \cos 2\alpha + \frac{1}{2} \sigma_{yy} \sin 2\alpha \right)^2} \quad (3.11)$$

The incremental direction of crack propagation is assumed to maximize the cohesive energy at A , according to the criteria

$$\frac{\partial \phi_A(\alpha)}{\partial \alpha} = 0 \quad \text{and} \quad \frac{\partial^2 \phi_A(\alpha)}{\partial \alpha^2} < 0. \quad (3.12)$$

The resulting direction of crack propagation α_0 is obtained by inserting Eqn. 3.11 into Eqn. 3.8 and using the maxima criteria in Eqn. 3.12 and can be written as follows:

$$\alpha_0 = \sin^{-1} \left(\frac{\sigma_{yy} - \sigma_{xx} \pm \sqrt{(\sigma_{xx} - \sigma_{yy})^2 + 4\sigma_{xy}^2}}{\sqrt{\left(\sigma_{yy} - \sigma_{xx} \pm \sqrt{(\sigma_{xx} - \sigma_{yy})^2 + 4\sigma_{xy}^2} \right)^2 + 4\sigma_{xy}^2}} \right). \quad (3.13)$$

The change in crack trajectory is achieved by generating a new mesh incorporating an updated crack path laced with cohesive elements. To reduce the computational expense associated with this process, the crack trajectory update is subjected to a geometric criterion that identifies whether there are tendencies for significant direction variation. The proposed geometric criterion requires that the crack path be updated only when the incremental direction (α_0) exceeds a tolerance limit based on the critical angle (α_c) that

minimizes the crack tip distance to the interface. Fig. 3.1 illustrates the crack geometry and critical angle schematically. As the undulation is idealized with a sinusoidal wave represented in Eqn. 3.14a and critical angle corresponds to the normal from the crack tip (x_2, y_2) to the interface (x_1, y_1) , α_c can be determined using the trigonometric relation in Eqn. 3.14b and is given in Eqn. 3.15.

$$y_1 = -A \left(1 + \sin \left(\frac{\pi}{2} - \frac{x_1}{W} \pi \right) \right) \quad (3.14a)$$

$$\frac{y_2 - y_1}{x_2 - x_1} = - \left(\frac{dy_1}{dx_1} \right)^{-1} = - \frac{W}{\pi A \cos \left(\frac{\pi}{2} - \frac{x_1}{W} \pi \right)} \quad (3.14b)$$

$$\alpha_c = \tan^{-1} \left(\frac{y_2 - y_1}{x_2 - x_1} \right) \quad (3.15)$$

Eqn. 3.15 shows that the critical angle of propagation is a function of crack tip location, as well as the undulation geometry. The crack path is updated when $\|\alpha_0\|/\|\alpha_c\|$ is greater than 0.1%.

3.3 FINITE ELEMENT MODELS OF TBC

3.3.1 MATERIAL MODELS

Advanced TBCs typically have nickel based super-alloy substrates with high strength and stiffness, even at elevated temperatures. The bond coat material of choice is an inter-metallic platinum modified nickel aluminide with a CTE similar to that of the substrate material. Mechanical properties of the bond coat material may vary with thermal cycling, and the bond coat may also undergo significant creep deformation at elevated temperature [27]. A thermally-activated creep material model for the bond coat has been proposed in [27] based on micro-tensile test results performed on bond coats extracted from actual TBC systems. The model is phenomenological in nature and does not account for explicit variables at the microstructural level. The strain rate-stress law in this model is expressed as

$$\begin{aligned}\dot{\epsilon}_{creep} &= 7.5 \times 10^{20} \left(\frac{\sigma}{E} \right)^{2.7} \exp\left(\frac{-340 [kJ/mol]}{RT} \right) & T < 800^\circ C \\ \dot{\epsilon}_{creep} &= 9.1 \times 10^{27} \left(\frac{\sigma}{E} \right)^4 \exp\left(\frac{-400 [kJ/mol]}{RT} \right) & T > 800^\circ C\end{aligned}\tag{3.16}$$

where $\dot{\epsilon}_{creep}$ is the equivalent creep strain rate, σ is the equivalent deviatoric stress, R is the gas constant, and T is the absolute temperature. The model was calibrated with

experiments in [27] and a change in model parameters was found at 800°C . This bond coat material model is implemented as a user subroutine in the ABAQUS [55] finite element package.

The effect of bond coat creep on the out-of-plane creep strain accumulation in the bond coat has been investigated analytically by Balint and Hutchinson [56] and numerically by Karlsson *et al.* [12]. Numerical implementation of the creep material model in this study is validated through reproducing results reported in [27] with similar geometry and material properties.

Although it is believed that damage initiates in the top coat [4] and accurate material model of the top coat are essential, the Yttria stabilized Zirconia with a strain tolerant columnar structure is not well characterized in the literature. The effect of the top coat material model was investigated to determine the best representation for accurate prediction of failure. The thermal expansion coefficient of the TGO is less than that of the substrate, causing very high compressive stresses in the TGO. The TGO reduces these stresses by lengthening through out-of-plane displacements that increase the undulations accommodated by a relatively compliant bond coat [13]. However, the top coat provides a constraint that restricts such deformation and leads to out-of-plane stresses near the

undulations. The magnitude and location of these stresses clearly depend on the top coat stiffness. A compliant top coat would not restrict TGO deformation and the out-of-plane stresses would localize at the TGO and top coat interface due to bending of the TGO. However, a stiffer top coat will prevent TGO deformation resulting in out-of-plane tensile stresses in the vicinity of the undulation. Since experimental observations in [4, 14, 30] suggest that cracks initiate away from the interface at the undulation sites, the top coat is idealized as an isotropic elastic material with no pre-existing flaws. Furthermore, although the columnar structure of the top coat suggests that under tension it will be more compliant in-plane than out-of-plane, CTE mismatches between the top coat and substrate will lead to in-plane compression. With little in-plane tension during load, effects of the columnar microstructure should not be significant. Mechanical properties of the top coat are sensitive to deposition process parameters as well as to the inter-columnar spacing [28]. The properties may also vary during the TBC service life due to sintering [57] with total exposure time at high temperatures. However, this variation is not significant over individual thermal cycles. Solutions with four different top coat moduli, ranging between 100 and 220 GPa, are considered in this study to account for microstructure variability in the specimens. Table 3.1 presents material property values

for each of the TBC layers obtained from those reported by Evans *et al.* [7] and Cheng *et al.* [29]. The rupture stress for top coat is assumed to be same as homogeneous Yittria stabilized Zirconia reported in [58].

3.3.2 GEOMETRIC MODEL AND FINITE ELEMENT MESH

A finite element model of the TBC system including the substrate, bond coat, TGO, and top coat is shown in Fig. 3.3. 2D plane strain representations of the TBC system are selected as undulations are assumed to run through the sample thickness. The TBC morphology is assumed to be symmetric about the vertical plane and only the half geometry is modeled. The undulations in the vicinity of planar interfaces between the TGO and bond coat are commonly observed due to the initial as well as growing surface roughness of the bond coat. In this study, only sinusoidal undulations penetrating into the bond coat are considered.

A $150 \times 1100 \mu\text{m}$ section of TBC system is modeled with a graded mesh of four-noded elements which are identified as CPE4(QUAD2D) in the ABAQUS element library [55]. The resulting model consist of more than 11,000 elements and 12,000 nodes, and exhibits less than 0.5% error in the strain energy when compared to a more refined mesh. As

shown in Fig. 3.3, a highly refined mesh is used in the vicinity of the TGO undulation, and the mesh becomes coarse away from the region of interest.

3.3.3 BOUNDARY CONDITIONS

In practice, the top surface of the TBC is exposed to hot combustion gases and is assumed to be free of any mechanical constraints or loads. The current TBC system model is subjected to a cyclic thermal load through variation of a uniformly applied temperature from 1000 °C to room temperature of 30 °C. Each nominal temperature cycle includes 10 minute heating, 10 minute hold at peak temperature, and 10 minute cooling. All analyses are performed for five successive cycles. The thermal loads caused by this thermal cycle generate in-plane compressive stresses in the TGO and top coat on account of the CTE mismatch. Although temperature gradients are expected along the TBC thickness during service, the uniform thermal load assumption is considered adequate since out-of-plane thermal effects are secondary to undulation stresses. For all analyses symmetry boundary conditions are applied at the left edge; a rigid substrate is simulated with roller supports applied at the lower horizontal boundary; and radial periodic boundary conditions are applied at the right edge of the models. These boundary conditions are shown pictorially in Fig. 3.3.

3.3.4 COHESIVE ZONE ELEMENT IMPLEMENTATION

The hysteretic cohesive model described in Sec. 3.2.2 is implemented as a four-noded cohesive element within ABAQUS's User defined Element (UEL) subroutines [55]. These elements are compatible with the regular, continuum ABAQUS QUAD2D elements. The element is comprised of two cohesive surfaces with 2 nodes each. In the initial, unloaded state, the nodes of the two surfaces share the same coordinates. With the application of external load, the surfaces move and separate from one another as the adjacent solid elements deform. The relative normal and tangential tractions for the 2D cohesive elements are calculated at the element integration points according to the traction separation law defined by Eqn. 3.2. The element has two integration points corresponding to those of the QUAD2D element. The parameters associated with the cohesive element definition in ABAQUS are the number of nodes for the element and their connectivity, the cohesive zone parameters associated with the element and the solution dependent state variables required for the element. Fig. 3.3 shows a TBC finite element model with cohesive elements along a representative crack path.

3.4 PARAMETRIC MODELING OF CRACK INITIATION AND PROPAGATION IN THE TOP COAT

The parametric space is defined by parameter ranges given in Table 3.2 and is spanned by nearly 100 simulations. These results yield information about how crack initiation and extension in the TBC system is sensitive to important geometrical, material, and loading parameters. Critical analysis of the results demonstrates that there are some parameter ranges that provide safer TBC designs.

TBC failure due to top coat spallation can be characterized by crack initiation and crack propagation phases. Two studies are conducted to investigate these phases. These studies are performed sequentially, namely, the probable locations of crack initiation are determined in the first study, and the subsequent study assumes existence of a finite crack at that location.

3.4.1 SENSITIVITY ANALYSIS FOR CRACK INITIATION WITHIN THE TOP COAT

In order to identify the critical parameters assisting crack initiation, a sensitivity analysis of the maximum first principal stress ($S1^{\max}$) with respect to geometric, material, and loading parameters is performed for the TBC system. Candidate parameters

considered in the sensitivity analysis are: (i) h , thickness of the TGO, (ii) A , amplitude of the sinusoidal undulation, (iii) W , wavelength of the undulation (iv) t , thickness of the top coat (v) E_{TGO} and a_{TGO} , stiffness and thermal expansion coefficient of the TGO, (vi) E_{TC} and a_{TC} , stiffness and thermal expansion coefficient of the top coat, (viii) s_r, s_h and s_c , heating, hold and cooling time of the thermal cycle respectively and (ix). T_{peak} , peak temperature of thermal cycle load. Definitions of the geometric parameters are pictorially given in Fig. 3.1. Individual parameters are varied incrementally while keeping all others stationary, *i.e.* parametric variation is achieved by changing the value of one parameter at a time. This is needed to isolate the effect of each parameter on the damage initiation and propagation. Such variation is performed for each parameter until the entire parametric space is spanned.

The simulations revealed that the magnitude and location of $S1^{max}$ in the top coat is sensitive to several parameters. It also shows that $S1^{max}$ occurs either along the axis of symmetry or along the interface. Hence, the location of the $S1^{max}$ is characterized by its normal distance from the interface (v). A representative set of the sensitivity analyses results for $S1^{max}$ magnitude are summarized in Figs. 3.4a-c, where the normalized $S1^{max}$ is plotted as a function of the normalized geometric, material, and loading parameters

respectively. The $S1^{\max}$ for each plot is normalized by $S1_0^{\max}$, the maximum amongst all reported results in that plot. Each parameter is normalized with its maximum value considered in this work. $S1^{\max}$ is found to be insensitive to any increase in the top coat thickness t or the bond coat thickness b beyond the nominal values ($b=60 \mu\text{m}$ and $t=100 \mu\text{m}$) selected. Fig. 3.4a shows that principal stress decreases exponentially with increasing undulation wavelength W and asymptotically approaches zero. This is confirmed by the fact that an undulation with infinite wavelength corresponds to a flat interface for which the $S1^{\max}$ principal stress is zero. For increasing amplitude A , there is first an increase in the principle stress and then exponential decay. Finally, the principal stress increases non-linearly with the TGO thickness h and with quasi-stabilization at high thickness values.

Fig. 3.4b shows that $S1^{\max}$ increases linearly with the top coat and TGO modulus with the TGO modulus having a steeper increase. The principal stress decreases almost linearly with increase in the thermal expansion coefficient of the TGO. However, increasing the thermal expansion coefficient of the top coat first decreases the principal stress and then causes rapid increase.

Fig. 3.4c shows that the increase in peak temperature of the thermal cycle almost linearly increases the principal stress. For higher values, the duration of the cooling and holding do not influence the principal stress. However, significant decreases in the cooling and holding durations can increase the principal stress significantly.

Parametric sensitivities of normal distance (ν) of the $S1^{\max}$ location from the interface are summarized in Figs. 3.5a-c, where the normalized ν is plotted as a function of the normalized geometric, material, and loading parameters. The ν for each case are normalized with respect to the corresponding maximum value of normal distance ν_o and each parameter is normalized with respect to its maximum value reported in the figure captions. Fig. 3.5a shows that increasing TGO thickness reduces the normal distance (ν) of $S1^{\max}$ from the interface. An increase in wavelength first reduces ν before sharply increasing it. The variation in ν due to increase in amplitude is parabolic, with ν increasing from zero, reaching a peak and then reducing back to zero. However, it should be noted that for these simulations, reduction of ν to zero resulted from the $S1^{\max}$ location moving to a different location along the interface and not just returning to the initial location.

Fig. 3.5b shows that for their range of variation, the moduli of TGO and top coat do not influence the location ν . An increase in TGO thermal expansion coefficient increases ν exponentially. The relationship between ν and a_{TC} is parabolic. Fig. 3.5c shows that the location of $S1^{\max}$ is insensitive to any increase in duration of heating, cooling, and holding time beyond 10 minutes. Furthermore, there is little change for a considerable increase in peak temperature.

3.4.2 PARAMETRIC DOMAIN MAP FOR DAMAGE INITIATION IN THE TOP COAT

The sensitivity analyses show that the maximum of the first principal stress ($S1^{\max}$) magnitude as well as its normal distance from the interface (ν) is very sensitive to several parameters. Due to the highly non-linear response that results from bond coat creep and cyclic loading, closed form parametric equations to predict failure are infeasible. Instead, a domain-partitioning map of the critical geometric parameters is developed as a tool to predict TBC failure.

From the sensitivity analyses, TGO thickness and undulation geometry are found to emerge as geometric parameters that have the most effect on damage. The multi-dimensional parametric space spanned by the parameters h , A , and W is characterized to

predict failure. In this work, a novel reduced order parametric space is introduced that can effectively represent the multi-parameter dependence of damage initiation. Two non-dimensional parameters (ψ, ξ) are uniquely defined from sensitivity and dimensional analysis for this representation as:

$$\psi = \frac{h^2}{A \times W} \quad (3.17a)$$

$$\xi = \frac{W}{A} \left(\frac{h}{h_0} \right)^{\left(\frac{2A}{W} \right)^3} \quad (3.17b)$$

where h is the TGO thickness, A is the undulation amplitude, W is the undulation wavelength and $h_0=1 \mu\text{m}$. Partitioning of the 2D (ψ, ξ) domain delineates regions of different damage characteristics. Three distinct domains, *viz.* “safe”, “fail,” and “sub-safe” sub-domains are introduced. The “safe” domain corresponds to the geometries for which no crack will be initiated in the top coat. The “fail” domain contains those geometries for which interfacial cracks will initiate. The “sub-safe” domain corresponds to geometries for which cracks will initiate away from the interface and further loading will determine if they will propagate towards the interface. The boundaries of the three

distinct domains are delineated by critical non-dimensional parameters ψ_c and ξ_c , and

the domains are expressed as:

$$\begin{aligned} \text{Fail Domain:} & \quad \psi \geq \psi_c \ \& \ \xi \geq \xi_c \\ \text{Sub-safe Domain:} & \quad \psi \geq \psi_c \ \& \ \xi < \xi_c \\ \text{Safe Domain:} & \quad \psi < \psi_c \end{aligned} \tag{3.18}$$

The critical values (ψ_c, ξ_c) are evaluated in the following steps:

- (i) Conduct simulations for various combinations of parameters and designate each parametric combination as fail, safe or sub-safe based on results of crack initiation.
- (ii) Determine the corresponding parameters (ψ, ξ) from Eqn. 3.17. The critical values ψ_c and ξ_c are identified as those that correspond to the transition between the different fail-safe domains as shown in Fig. 3.6.

The critical co-ordinates defining the partition boundaries are determined to be $\psi_c = 2.0 \times 10^{-2}$ and $\xi_c = 4.8$. It should be noted that this domain delineation is done for $E_{TC} = 200$ GPa and $E_{TGO} = 400$ GPa. The complete dependence of these domains on E_{TC} and E_{TGO} will be explored in future studies.

3.4.3 SENSITIVITY ANALYSIS FOR CRACK PROPAGATION WITHIN THE TOP COAT

For the domain map the “safe” configurations that do not initiate cracks and the “fail” configurations that initiate cracks at the interface are readily identified. However, the occurrences of “sub-safe” configurations require additional analysis for further subdivision into “safe” and “fail.” Since the maximum principal stress axis is always parallel to the axis of symmetry, a horizontal crack path is selected for all sub-safe geometries and is laced with hysteretic cohesive elements. The crack is allowed to propagate with cyclic thermal loading while monitoring the incremental direction of propagation. As discussed in Sec. 3.2.2.2, the analysis is terminated when the incremental direction of crack propagation (α_0) exceeds 0.1% of the critical angle (α_c).

The cracks that deviate away from the interface ($\alpha_0 > 0$) at the termination of the analysis are unlikely to cause interfacial delamination and are thus re-classified as “safe”. Configurations that propagate cracks towards the interface ($\alpha_0 < 0$) could reach the interface and become “fail” or could arrest and become “safe.” Given the complexity of the cracks propagating towards the interface, the present focus is on cracks that are repelled away from the interface.

A parametric investigation of the sensitivity of the incremental direction with geometric parameters including (i) h , thickness of the TGO, (ii) A , amplitude of the sinusoidal undulation, and (iii) W , wavelength of the undulation. Fig. 3.7 shows the relationship between crack propagation direction (α_0) normalized by its maximum value and normalized geometric parameters. Each parameter is normalized with the maximum value given in the figure caption. Fig. 3.7 shows that increase in TGO thickness (h) decreases the incremental angle (α_0) which promotes potentially critical cracks that are attracted towards the interface. An increase in undulation amplitude (A) or wavelength (W) is likely to suppress critical cracks as they promote repulsion of cracks away from the interface.

The functional dependence of crack deflection on geometric parameters is formalized using the following dimensionless parametric expression ζ :

$$\zeta = \frac{A}{A_0} \frac{W}{h} \cos\left(2\pi \frac{h}{h_0}\right) \quad (3.19)$$

where A is the undulation amplitude, W is the undulation wavelength and h is the TGO thickness, $h_0 = 5\mu m$ and $A_0 = 10\mu m$. Sensitivity studies show that for the "sub-safe" parametric combinations for which $\zeta \leq \zeta_c$, the cracks are repelled away from interface

and are deemed safe. The critical value, ζ_c , is determined from the sensitivity data to be 2.32. Similar to the domain map, this delineation of safe geometries is done for $E_{TC} = 200 \text{ GPa}$ and $E_{TGO} = 400 \text{ GPa}$. This parametric expression ζ can be used in combination with domain maps for selection of safer TBC designs.

3.5 COMPARISON OF NUMERICAL PREDICTION WITH EXPERIMENTS

As a final step, the experimental observations of top coat failure reported in the literature [4, 7] and compared with the domain map prediction as well as finite element simulations. Two cases are considered for which geometric parameters and crack trajectories are obtained from SEM micrographs as follows:

- a) $A=10 \text{ }\mu\text{m}$, $W=40 \text{ }\mu\text{m}$ and $h=3\mu\text{m}$ with a crack initiating at $v\sim 9 \text{ }\mu\text{m}$ and propagating horizontally for $\sim 14 \text{ }\mu\text{m}$ before deviating slightly towards the interface and leading to delamination (*Fig. 8b* in [4]), and
- b) $A=10 \text{ }\mu\text{m}$, $W=30 \text{ }\mu\text{m}$ and $h=3 \text{ }\mu\text{m}$ with a crack initiating at $v\sim 5.5 \text{ }\mu\text{m}$ and propagating horizontally for $\sim 7.5 \text{ }\mu\text{m}$ before deviating slightly towards the interface and penetrating the TGO layer (*Fig. 7c* in [7]).

For both cases of A , W , and h parameter combinations in the two situations described above, Eqn. 3.18 predicts the TBC to be in the “sub-safe” domain. This is in agreement with the experimentally observed crack initiation away from the interface.

The finite element simulations with nominal values for material and cohesive parameters, (*i.e.*, $E_{TGO} = 400$ GPa, $E_{TC} = 200$ GPa and $\sigma_{\max} = 287$ MPa) yield the following crack trajectories for the corresponding cases described above:

- a) The crack initiates at $v=9.8$ μm from the interface and propagates horizontally for 15 μm before the first directional update.
- b) The crack initiates at $v=6.38$ μm from the interface and propagates horizontally for 8.75 μm before the first directional update.

In both cases the cracks deviate towards the interface indicating a possibly critical crack. The finite element simulations of crack initiation and propagation agree very well with the experimentally observed crack trajectories. This implies that the modeling framework employed to develop the domain map is capable of accurately predicting crack trajectories.

3.6 CONCLUSIONS

In this chapter, failure characteristics of elastic top coats for thermal barrier coatings (TBCs) are investigated using a finite element model. The evolution of maximum principal stress determines the onset of top coat cracking. Some of these cracks are postulated to subsequently lead to delamination of the interface between the top coat and the TGO. A hysteretic cohesive zone model is employed to study crack propagation within the top coat. The materials and geometries in the study are chosen to be representative of TBC materials in real applications. The contribution of geometric parameters to crack initiation is estimated, and a multi-dimensional parametric space is represented as a reduced-order 2-D parametric domain map for crack initiation in terms of the parameters. The reduced-order domain map is constructed by collecting the relevant parameters into 2 unique variables that span the 2-D domain. This domain classifies the design space as “fail”, “safe,” and “sub-safe” for crack initiation.,

The direction of crack propagation for TBC designs identified as “sub-safe” are also investigated. The crack propagation is assumed to be in the direction that maximizes the cohesive energy based on the criterion proposed by Li and Ghosh [18]. Since, interfacial delamination is ultimately responsible for TBC failure, designs that attract the crack

towards the interface are deemed “fail” and those repelling it as “safe”. The potentially safer combinations within the "sub-safe" domain are identified by a third dimensionless expression within the domain map. However, this domain map is limited to specific material properties of the constituent layers and explicit dependence on material parameters will be established in future investigations.

The chapter concludes with finite element simulations of two representative failure scenarios from the literature. The geometry and material properties for these cases are obtained from the literature and nominal material properties are selected for simulations. The parametric domain map predictions for criticality of crack initiation and propagation are found to be in good agreement experimental observations. Furthermore, finite element simulations of the propagation also compare well with the experimentally observed crack trajectories.

Despite establishing parametric criteria to determine initiation of micro-cracks in the top coat, the present study is limited to establishing the critical direction of crack propagation. However, cracks that tend to propagate *towards* the interface do not ensure interfacial delamination since the crack may arrest before actually reaching the interface. Thus the proposed domain maps provide a conservative estimate of safer TBC designs.

Parametric investigations accounting for other factors like rate of crack propagation can reduce the conservativeness and are the subject of future work.

Property	Substrate	TGO	TBC
Poisson's Ratio	0.31-0.35	0.23-0.25	0.10-0.12
Elastic modulus (GPa)	120-220	320-400	100-220
Thermal expansion coefficient ($10^{-6} / ^\circ\text{C}$)	14.8-18.0	4.0-8.0	6.0-12.2
Rupture Stress (Mpa)	-	-	287

Table 3.1. Material properties of components of the TBC system as obtained from [7, 29, 58]

Parameter	Range of Variation
TGO thickness (h)	2-6 μm
Undulation amplitude (A)	5-50 μm
Undulation wavelength (W)	10-160 μm
TC thermal expansion (a_{TC})	6-12 x 10^{-6}
TGO thermal expansion (a_{TGO})	4-8 x 10^{-6}
Top coat modulus (E_{TC})	100-220 GPa
TGO modulus (E_{TGO})	320-400 GPa

Table 3.2. Range of variation of parameters from experimental observations reported in [4, 7, 21, 38, 39, 59]

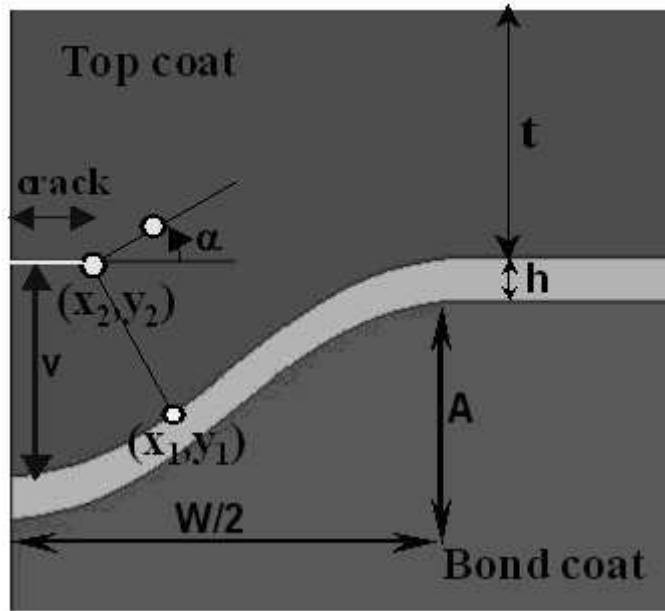


Figure 3.1: Schematic diagram of the TBC model showing geometric and dimensional parameters of the undulation as well as the location of the crack characterized by normal distance v . The Substrate, excluded here for clarity, is included in the finite element model.

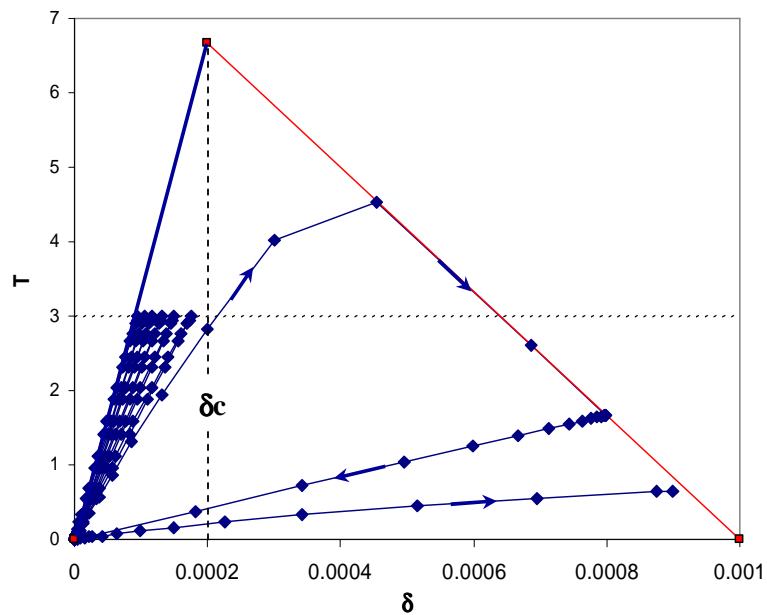


Figure 3.2: A plot showing the hysteretic cohesive zone element response with cyclic loading to eventual failure when $\delta = \delta_c = 0.001$.

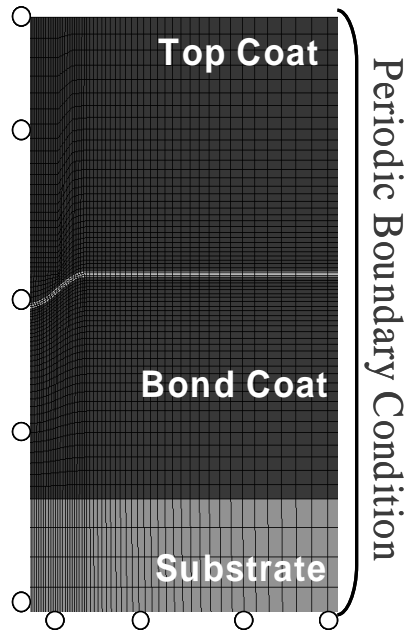
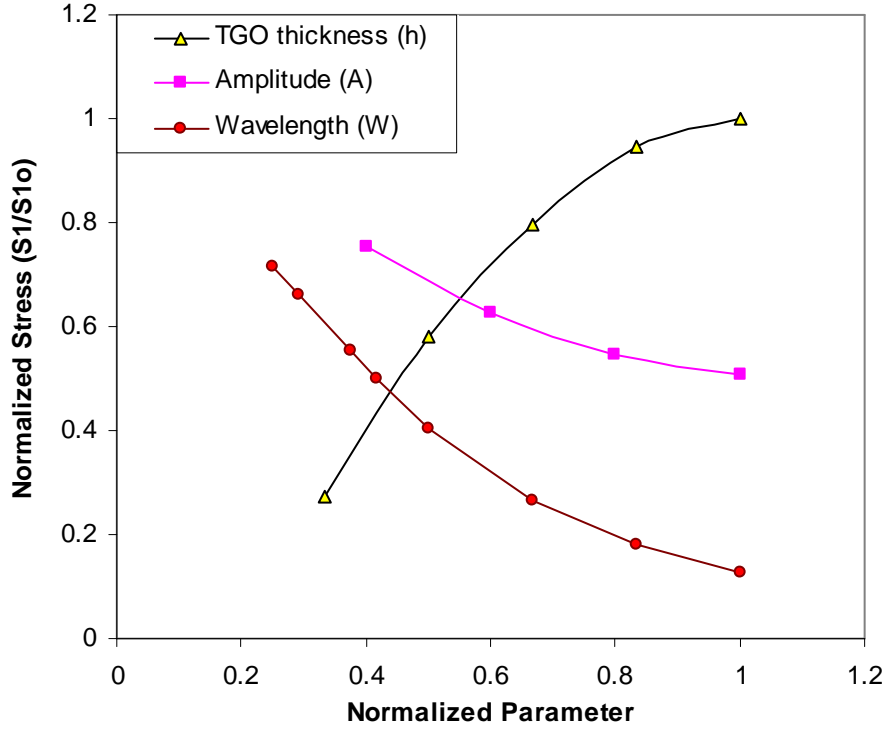


Figure 3.3: Finite element model (*not to scale*) of the TBC system with the bottom of substrate constrained to remain flat, symmetry at left vertical edge and radial periodicity at the right vertical edge.

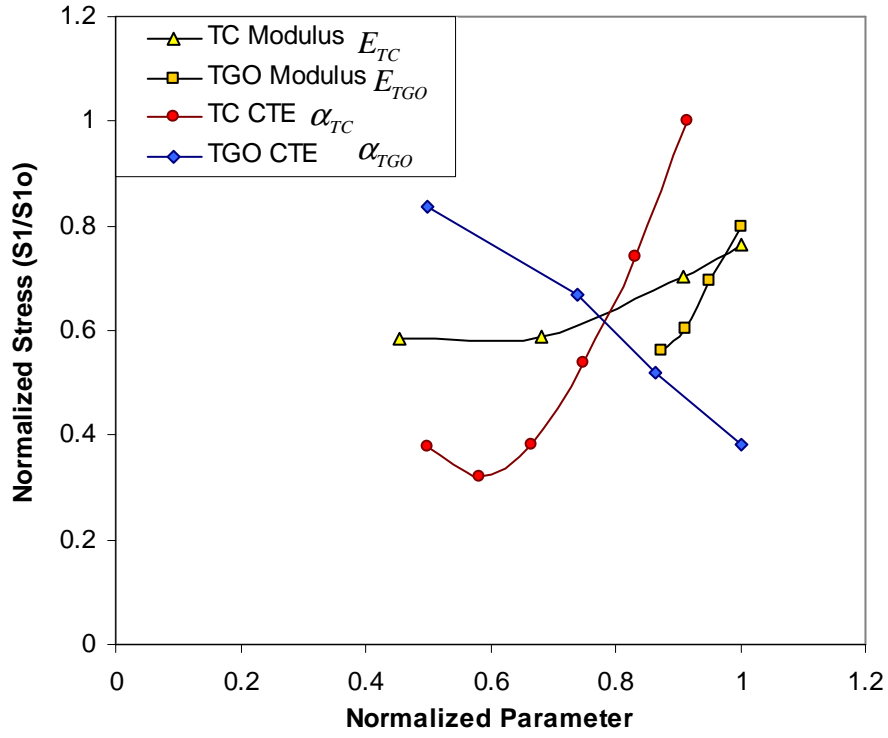


(a)

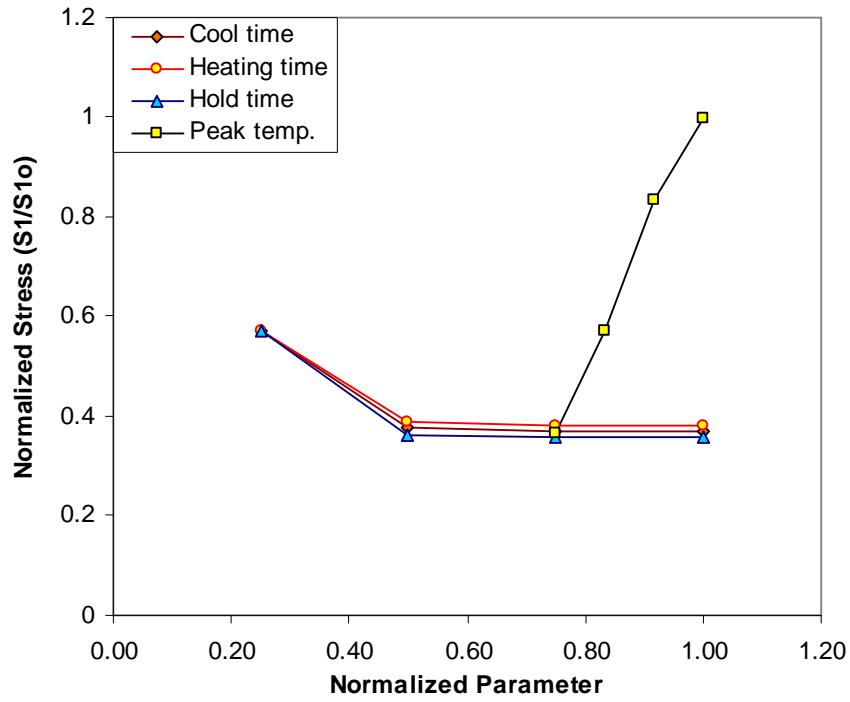
Continued

Figure 3.4: Plots showing top coat principal stress sensitivity to (a) geometric parameters (normalizing values of $h^{max}=6 \mu\text{m}$, $A^{max}=25 \mu\text{m}$, $W^{max}=120 \mu\text{m}$, and $S1^{max}=604 \text{MPa}$), b) material parameters (normalizing values of $E_{TGO}^{max}=400 \text{GPa}$, $E_{TC}^{max}=220 \text{GPa}$, $\alpha_{TC}^{max}=12\text{e-}6$, $\alpha_{TC}^{max}=8\text{e-}6$, and $S1_0^{max}=167.16 \text{MPa}$), and c). thermal load cycle parameters (normalizing values of $s_r^{max}=40 \text{minutes}$, $s_c^{max}=40 \text{minutes}$, $s_h^{max}=40 \text{minutes}$, $T_{peak}^{max}=1200 \text{ }^\circ\text{C}$, and $S1_0^{max}=363.20 \text{MPa}$).

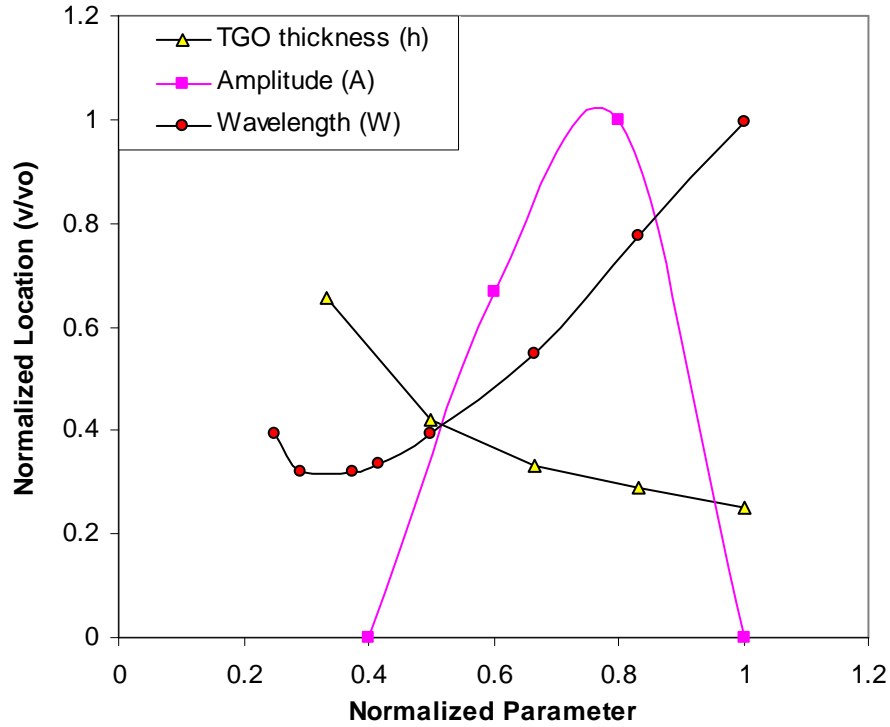
Figure 3.4 continued



(b)



(c)

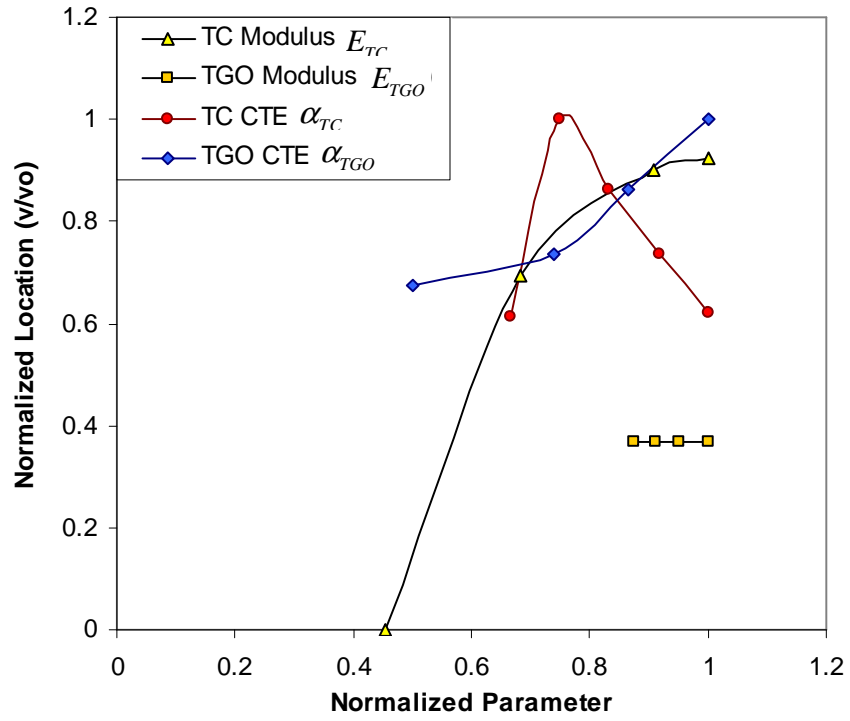


(a)

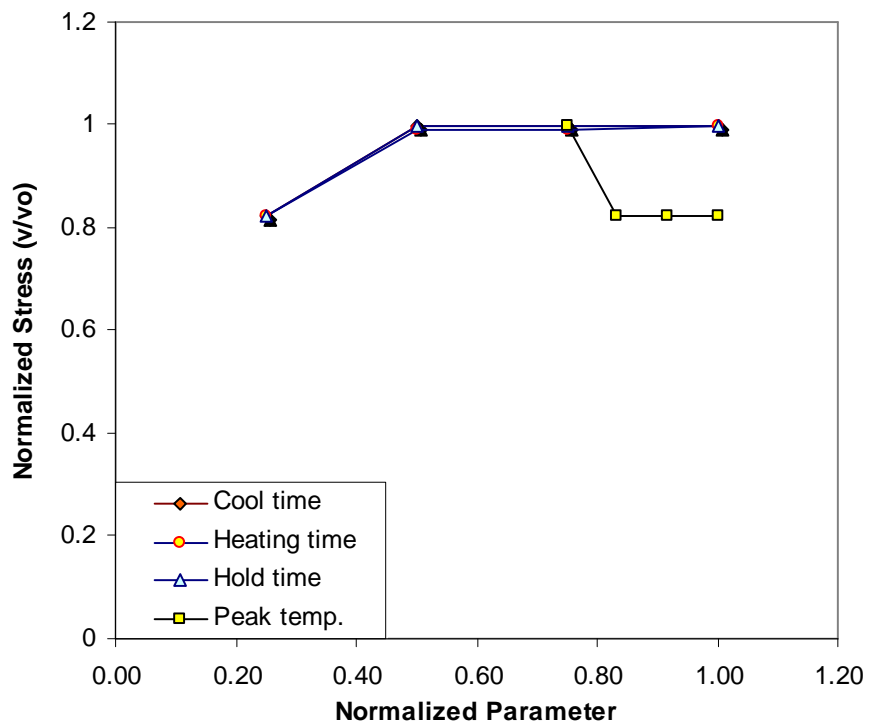
Continued

Figure 3.5: Plots showing sensitivity of the location of principal stress to (a) geometric parameters (normalizing values of $h^{\max} = 6 \mu\text{m}$, $A^{\max} = 25 \mu\text{m}$, $W^{\max} = 120 \mu\text{m}$, and $\nu_0 = 15.22 \mu\text{m}$), (b) material parameters (normalizing values of $E_{TGO}^{\max} = 400 \text{ GPa}$, $E_{TC}^{\max} = 220 \text{ GPa}$, $a_{TC}^{\max} = 12\text{e-}6$, $a_{TGO}^{\max} = 8\text{e-}6$ and $\nu_0 = 32.53 \mu\text{m}$) and c). thermal load cycle parameters (normalizing values of $s_r^{\max} = 40 \text{ minutes}$, $s_c^{\max} = 40 \text{ minutes}$, $s_h^{\max} = 40 \text{ minutes}$, $T_{peak}^{\max} = 1200 \text{ }^\circ\text{C}$, and $\nu_0 = 20.18 \mu\text{m}$)

Figure 3.5 continued



(b)



(c)

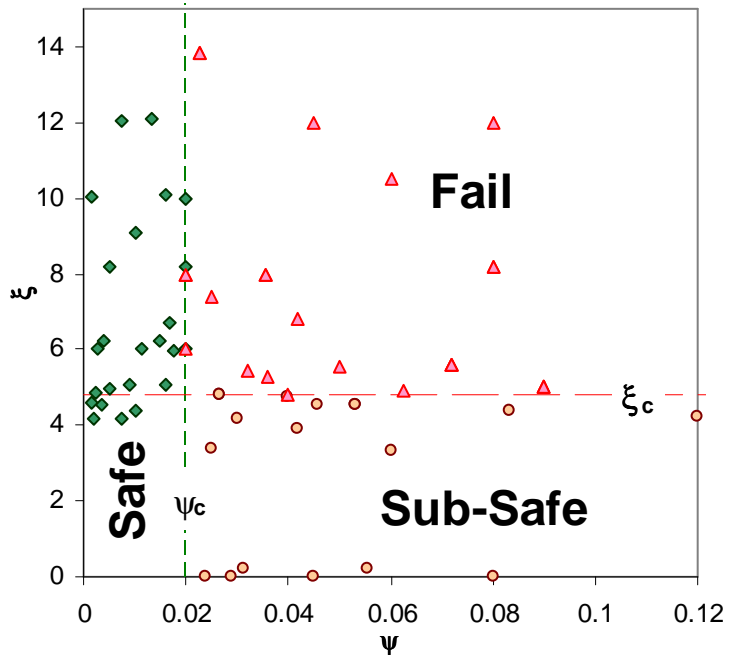


Figure 3.6: Plot showing the domain map of the parametric space delineating TBC designs into safe, sub-safe and fail combinations based on two unique combinations of parameters ψ and ξ .

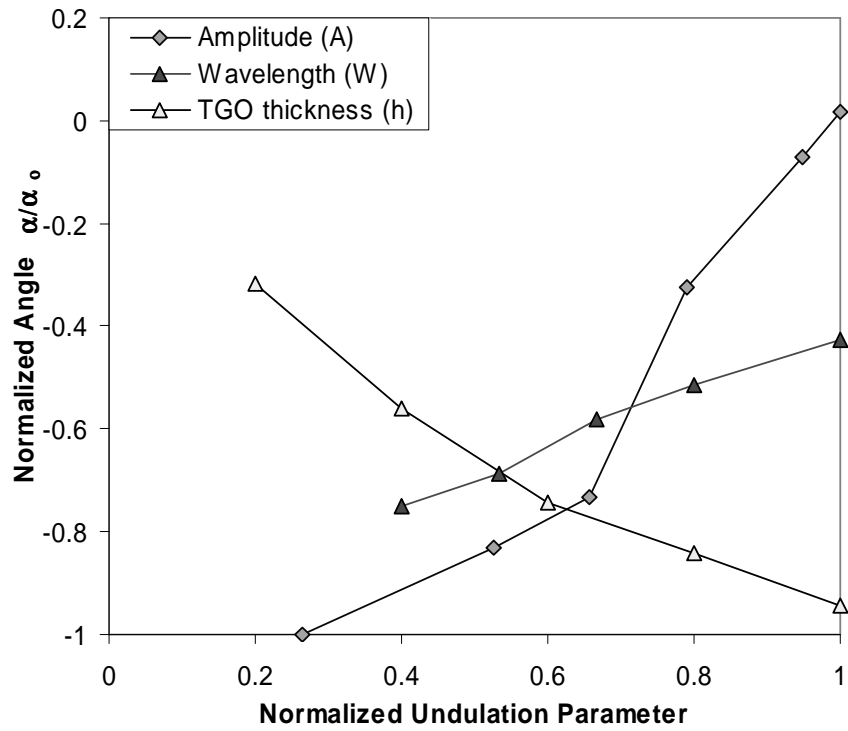


Figure 3.7: Plots showing sensitivity of the incremental direction of crack propagation to geometric parameters (normalizing values of $h^{\max} = 10 \mu\text{m}$, $A^{\max} = 38 \mu\text{m}$, $W^{\max} = 120 \mu\text{m}$, and $\alpha_0 = 8.73^\circ$), and

CHAPTER 4

A PARAMETRIC STUDY OF DAMAGE INITIATION AND PROPAGATION IN EB-PVD THERMAL BARRIER COATINGS

4.1 INTRODUCTION

There is experimental evidence that with significant bond coat creep, damage initiates within the top coat that leads to delamination of the top coat and TGO interface [12, 13, 44]. Damage within the top coat is driven primarily by the stresses developed due to the coefficient of thermal expansion (CTE) mismatch between the different layers during thermal loading, as well as by creep deformation of the bond coat. Notable among the factors which contribute to damage initiation and propagation are thermo-mechanical material properties and morphological features of interfaces and constituent layers.

There exists a significant body of work characterizing the growth of undulations under cyclic loading [12, 13, 44]. A number of these investigations also consider the top coat damage [12, 13], but the relationship between damage and geometric and material

factors has not been addressed in detail. Xu *et al.* [14] have demonstrated the variation in energy release rate as the crack propagates within the top coat for crack paths that were selected *a priori*.

This chapter starts with the development of parametric understanding of top coat crack initiation and propagation responsible for eventual delamination of TGO and top coat interface. A parametric relationship for the maximum principal stress with material and geometric parameters is developed to predict crack initiation. Subsequently, crack propagation and the interfacial delamination are investigated for all parametric combinations resulting in cracks initiating away from the interface. As a final step, the crack trajectory predicted by finite element simulation is compared with a top coat cracking observed in a real microstructures.

4.2 FINITE ELEMENT MODELS OF TBCS

A finite element model is developed to investigate delamination of the TGO and top coat interface. The model features bond coat creep and top coat damage evolution, which is characterized by crack initiation and crack propagation phases. To characterize both phases, the following two studies are performed: a) determination of probable crack

initiation and b) subsequent crack propagation study assuming a finite crack at the initiation locations.

For the first study, a mode I crack initiation criterion similar to [45] is employed where damage appears as a finite crack oriented normal to principal direction and when the maximum of first principal stress ($S1^{max}$) exceeds rupture stress ($\sigma_{rupture}$):

$$S1^{max} \geq \sigma_{rupture} \quad (4.1)$$

This criterion enables identification of safer TBC designs through a sensitivity analysis to determine the relationship between $S1^{max}$ and the various geometric and material parameters. The parameters considered for this study include: a) top coat modulus (E_{TC}), b) TGO modulus (E_{TGO}), c) TGO thickness (h), d) amplitude (A) and wavelength (W) of the undulation, and e) thermal cycle parameters including peak temperature and heating, holding, and cooling time. Since the resulting crack is oriented normal to the principal direction, the orientation of the principal axis is recorded to introduce properly oriented nascent cracks.

The subsequent crack propagation study simulates crack propagation by inserting a hysteretic cohesive zone between continuum elements of the finite element mesh. The evolution of the crack path is determined by selecting the direction of maximum cohesive

energy as proposed in [18]. This eliminates the mesh-dependent prediction of crack path even with a structured mesh [17].

Various aspects of this finite element model of the TBC are summarized in the following subsections.

4.2.1 MATERIAL MODELS

The bond coat material of choice for TBCs is an inter-metallic platinum modified nickel aluminide with a CTE similar to that of the substrate material. In this study, a thermally-activated creep material model for the bond coat proposed in [27] is employed. The creep model in [27] is based on micro-tensile test results performed on bond coats extracted from actual TBC systems and are deemed accurate. The strain rate-stress law in this creep model is expressed as

$$\begin{aligned} \dot{\epsilon}_{creep} &= 7.5 \times 10^{20} \left(\frac{\sigma}{E} \right)^{2.7} \exp\left(\frac{-340 [kJ/mol]}{RT} \right) & T < 800^\circ C \\ \dot{\epsilon}_{creep} &= 9.1 \times 10^{27} \left(\frac{\sigma}{E} \right)^4 \exp\left(\frac{-400 [kJ/mol]}{RT} \right) & T > 800^\circ C \end{aligned} \quad (4.2)$$

where $\dot{\epsilon}_{creep}$ is the equivalent creep strain rate, σ is the equivalent deviatoric stress, R is the gas constant, and T is the absolute temperature. The bond coat material model is implemented as a user subroutine in the ABAQUS [55] finite element package.

Advanced TBCs typically have nickel based super-alloy substrates with high strength and stiffness at elevated temperatures. Thus the substrate is treated as an isotropic, elastic material. The top coat and TGO are idealized as an isotropic, elastic material with no pre-existing flaws. Although the columnar structure of the top coat suggests that it will be more compliant under tension than under compression, CTE mismatches between the top coat and substrate would prevent in-plane tension. With little in-plane tension, effects of the columnar microstructure should not be significant. The rupture stress for the top coat is assumed to be same as homogeneous Yittria stabilized Zirconia reported in [58]. The material property values for each of the TBC layers are same as those reported in Table 3.1; values were obtained from [7, 29, 58].

4.2.2 GEOMETRIC MODEL AND FEM MESH

A finite element model of the TBC system including the substrate, bond coat, TGO, and top coat is shown in Fig. 4.2. 2D plane strain representations of the TBC system are selected as undulations are assumed to run through the sample thickness. The TBC morphology is assumed to be symmetric about the vertical plane and only the half geometry is modeled. In this study, only sinusoidal undulations penetrating into the bond coat are considered.

A $150 \times 1100 \mu\text{m}$ section of TBC system is modeled with a graded mesh of four-noded elements which are identified as CPE4(QUAD2D) in the ABAQUS element library [55]. The resulting model consist of more than 11,000 elements and 12,000 nodes, and exhibits less than 0.5% error in the strain energy when compared to a more refined mesh. As shown in Fig. 4.2b, mesh in the vicinity of the TGO undulation is refined and becomes coarse away from the region of interest.

4.2.3 BOUNDARY CONDITIONS

The TBC system model is subjected to a cyclic thermal load through variation of a uniformly applied temperature from $1000 \text{ }^\circ\text{C}$ to room temperature of $30 \text{ }^\circ\text{C}$. Each nominal temperature cycle includes 10 minutes of heating and a 10 minute hold at peak temperature and 10 minutes of cooling. The top surface of the TBC is assumed to be free of any mechanical constraints or loads. Symmetry boundary conditions are applied at the left edge, roller supports are applied at the lower horizontal boundary; and radial periodic boundary conditions are applied at the right edge of the models. These boundary conditions are shown pictorially in Fig. 4.2b.

4.2.4 IRREVERSIBLE HYSTERETIC MIXED-MODE COHESIVE ZONE MODEL

Due to the cyclic nature of the thermal loading, TBCs may incur significant fatigue damage within the top coat leading to crack coalescence and failure. The hysteretic cohesive models proposed by Nyugen *et al.* [50] and Maiti and Guebelle [51] and extended for mixed mode application by Bhatnagar *et al.* [60] will be employed for this investigation. This hysteretic cohesive model reduces to an irreversible bi-linear, rate-independent cohesive law under monotonic loading [48, 51].

The bi-linear cohesive model is discussed in detail elsewhere *e.g.*, [48, 61] and is summarized by the following traction-separation law:

$$T = \begin{cases} \frac{\sigma_{\max}}{\delta_c} \delta & \text{if } \delta < \delta_c \text{ (hardening region)} \\ \frac{\sigma_{\max}}{\delta_c - \delta_e} (\delta - \delta_e) & \text{if } \delta_c < \delta < \delta_e \text{ (softening region)} \\ 0 & \text{if } \delta > \delta_e \text{ (completely debonded)} \end{cases} \quad (4.3)$$

The effective separation and effective traction are defined as $\delta = \sqrt{\delta_n^2 + \beta^2 \delta_t^2}$ and $T = \sqrt{T_n^2 + \beta^{-2} T_t^2}$, respectively, where δ_n and T_n are the normal separation and traction, δ_t and T_t are the tangential separation and traction and β is an empirical factor. As shown in Fig. 4.3 as the effective separation increases, the effective traction across the elements linearly increases to a maximum value (σ_{\max}) at δ_c , and then decreases for further

increase in separation. This increase in traction is known as hardening and is elastic. The subsequent decrease is known as softening. Any further unload/reload prior to reaching the maximum separation of δ_c is carried out with lower stiffness. After exceeding δ_c , the element has zero stiffness.

To account for dissipative mechanisms in the fracture process zone ahead of the crack tip, a hysteretic model incurs fatigue damage only during reloading. During reloading the stiffness of the cohesive element is assumed to decay according to the stiffness degradation given below in Eqn. 4.4 and again shown in Fig. 4.3. The rate of stiffness decay is controlled by the introduction of an additional parameter δ_f .

$$\begin{aligned} \dot{K}_{nn} &= \begin{cases} -K_{nn} \frac{\dot{\delta}_n}{\delta_f} & \text{if } \dot{\delta}_n > 0 \\ 0 & \text{if } \dot{\delta}_n \leq 0 \end{cases} \\ \dot{K}_{tt} &= \begin{cases} -K_{tt} \frac{\dot{\delta}_t}{\delta_f} & \text{if } \dot{\delta}_t > 0 \\ 0 & \text{if } \dot{\delta}_t \leq 0 \end{cases} \end{aligned} \quad (4.4)$$

These incremental stiffness equations are integrated to calculate the stiffness at the $(p+1)^{th}$ step in terms of the stiffness of the p^{th} load step and increment in displacement jump. The resulting normal and tangential stiffness are:

$$K_{nn}^{p+1} = K_{nn}^p e^{\frac{\Delta\delta_n}{\delta_f}} \quad \text{and} \quad K_{tt}^{p+1} = K_{tt}^p e^{\frac{\Delta\delta_t}{\delta_f}} \quad (4.5)$$

where $\Delta\delta_n = \delta_n^{p+1} - \delta_n^p$ and $\Delta\delta_t = \delta_t^{p+1} - \delta_t^p$.

The hysteretic response of the cohesive model remains within the envelope of the bilinear model, and when the reloading curve intersects the softening curve it follows the curve for as long as the loading process continues. During such periods the element accrues only monotonic damage without any fatigue damage. From the above formulation, it can be seen that five cohesive zone parameters namely, σ_{\max} , δ_c , δ_e , δ_f , and β define the hysteretic cohesive model response.

This hysteretic cohesive model is implemented as a four-noded cohesive element within an ABAQUS User defined Element (UEL) subroutine [55]. These elements are compatible with the regular, continuum ABAQUS QUAD2D elements. The element is comprised of two cohesive surfaces with 2 nodes each. In the initial, unloaded state, the nodes of the two surfaces share the same coordinates. With the application of external load, the surfaces move and separate from one another as the adjacent solid elements deform. The relative normal and tangential tractions for the 2D cohesive elements are calculated at the element integration points according to the traction separation law defined by Eqn. 4.3. The element has two integration points corresponding to those of the QUAD2D element. Fig. 4.2 shows a TBC finite element model with cohesive elements along a representative crack path.

4.2.5 INCREMENTAL DIRECTION OF CRACK PROPAGATION

The crack trajectory cannot be determined *a priori* as it depends on the local drivers at the crack tip. Since the crack is restricted to follow the trajectory defined by the cohesive zone elements, it is imperative to evaluate the direction of crack propagation at each increment of loading. In the present work direction is determined using the maximum cohesive energy criterion proposed by Li and Ghosh [17, 18]. This criterion postulates that the crack will propagate in the direction that maximizes the cohesive energy. From the definition of the J-Integral, a relation between the cohesive energy ϕ for complete decohesion and the critical energy release rate G_c has been established by Ortiz *et al.* [47] as:

$$G_c = J = \int_0^R T \frac{\partial \delta}{\partial x} dx = \int_0^{\delta_c} T d\delta = \phi \quad (4.6)$$

where R is the length of the cohesive zone. Consequently, for a given crack tip state of stress, the crack growth direction is estimated as that along which G_c or equivalently the cohesive energy ϕ is maximized. The cohesive energy ϕ_A at the crack tip A along any direction α can be expressed for an arbitrary effective separation $\delta(\alpha)$ as:

$$\phi_A(\alpha) = \left(\int_0^{\delta} T(\alpha) d\delta \right)_A = \left(\int_0^t T(\alpha) \cdot \frac{\partial \delta}{\partial t} dt \right)_A \quad (4.7)$$

where $T(\alpha) = \sqrt{(T_n^{coh})^2 + \beta^{-2} (T_t^{coh})^2}$ is the magnitude of the effective cohesive traction.

The corresponding unit normal \mathbf{n} and tangential \mathbf{t} vectors along the direction α are expressed as:

$$\mathbf{n} = -\sin \alpha \mathbf{i} + \cos \alpha \mathbf{j} \quad \text{and} \quad \mathbf{t} = \cos \alpha \mathbf{i} + \sin \alpha \mathbf{j} \quad (4.8)$$

The normal and tangential components of the cohesive traction force at an angle α are then deduced as:

$$\begin{Bmatrix} T_n^{coh} \\ T_t^{coh} \end{Bmatrix} = \begin{bmatrix} n_x & n_y \\ t_x & t_y \end{bmatrix} \begin{Bmatrix} \sigma_{xx} n_x + \sigma_{xy} n_y \\ \sigma_{xy} n_x + \sigma_{yy} n_y \end{Bmatrix} = \begin{Bmatrix} \sigma_{xx} \sin^2 \alpha + \sigma_{xy} \sin 2\alpha + \sigma_{yy} \cos^2 \alpha \\ -\frac{1}{2} \sigma_{xx} \sin 2\alpha + \sigma_{xy} \cos 2\alpha + \frac{1}{2} \sigma_{yy} \sin 2\alpha \end{Bmatrix} \quad (4.9)$$

and hence the effective cohesive traction for direction α is:

$$T(\alpha) = \sqrt{\left(\sigma_{xx} \sin^2 \alpha - \sigma_{xy} \sin 2\alpha + \sigma_{yy} \cos^2 \alpha \right)^2 + \beta^{-2} \left(-\frac{1}{2} \sigma_{xx} \sin 2\alpha + \sigma_{xy} \cos 2\alpha + \frac{1}{2} \sigma_{yy} \sin 2\alpha \right)^2} \quad (4.10)$$

$\phi_A(\alpha)$ is evaluated by inserting Eqn. 4.10 into Eqn. 4.7 and maxima is obtained using the extremum criteria in Eqn. 4.11. Thus, the resulting direction of crack propagation α_0 is reported in Eqn. 4.12.

$$\frac{\partial \phi_A(\alpha)}{\partial \alpha} = 0 \quad \text{and} \quad \frac{\partial^2 \phi_A(\alpha)}{\partial \alpha^2} < 0. \quad (4.11)$$

$$\alpha_0 = \sin^{-1} \left(\frac{\sigma_{yy} - \sigma_{xx} \pm \sqrt{(\sigma_{xx} - \sigma_{yy})^2 + 4\sigma_{xy}^2}}{\sqrt{\left(\sigma_{yy} - \sigma_{xx} \pm \sqrt{(\sigma_{xx} - \sigma_{yy})^2 + 4\sigma_{xy}^2}\right)^2 + 4\sigma_{xy}^2}} \right). \quad (4.12)$$

Any change in crack trajectory is achieved by generating a new mesh incorporating an updated crack path laced with cohesive elements. To reduce the computational expense associated with this process, the crack trajectory is updated when there are tendencies for significant directional change.

4.2.6 SELECTION OF COHESIVE ZONE PARAMETERS

A rigorous methodology is followed for the selection of five cohesive zone parameters namely, σ_{\max} , δ_c , δ_e , δ_f , and β defining the hysteretic cohesive zone response. First, the peak stress σ_{\max} is set equal to the rupture stress of the top coat material, thus simulating the onset of damage. Next, selection of δ_c determines the hardening stiffness (σ_{\max}/δ_c) of the cohesive zone and requires sensitivity study. Fig. 4.4 summarizing the sensitivity study and shows that the crack propagation angle α_0 computed by Eqn. 4.12 monotonically converges to a stabilized value with increasing hardening stiffness. For hardening stiffness above 6e9 MPa/ μm the variation in α_0 becomes less than 1% and convergence is assumed. Hence, δ_c is computed using this stiffness along with the

selected σ_{\max} . Furthermore, δ_e is computed by equating the cohesive energy to fracture toughness of the material as demonstrated in Eqn. 4.6. Finally, the fatigue damage parameter δ_f is chosen to be $5 \delta_e$.

4.3 PARAMETRIC MODELING OF CRACK INITIATION IN THE TOP COAT

Simulations conducted with the computational models discussed in Sec. 4.2 are used to derive a functional form for the maximum principal stress (SI^{max}) in terms of important geometrical and material parameters in the TBC system. Sensitivity analyses of these drivers are conducted with respect to various parameters and the results are utilized in the determination of the functional dependence. Although, finite element simulations show that location of maximum principal stress is variable only SI^{max} magnitude variation is considered for development of the parametric relation. Candidate parameters considered in the sensitivity analysis are: (i) h , thickness of the TGO, (ii) A , amplitude of the sinusoidal undulation, (iii) W , wavelength of the undulation (iv) t , thickness of the top coat (v) E_{TGO} , modulus of the TGO and (vi) E_{TC} , modulus of the top coat. Definitions of the geometric parameters are pictorially given in Fig. 4.2a. The parametric space is defined by parameter ranges given in Table 3.2 of the previous chapter.

For sensitivity analyses, a parametric matrix covering all possible combinations of parameters and their values is generated. To limit the number of analyses few discrete values are selected for each parameter to represent its range. The simulations revealed that the magnitude and location of $S1^{\max}$ in the top coat is sensitive to several parameters. A representative set of the sensitivity analyses results for $S1^{\max}$ magnitude are summarized in Fig. 4.5a and 4.5b, where the normalized $S1^{\max}$ is plotted as a function of the normalized geometric and material parameters respectively. The $S1^{\max}$ for each plot is normalized with $S1_0^{\max}$, the maximum amongst all reported results in that plot. Each parameter is normalized with its maximum value in Table 3.2. Beyond the nominal values ($b=60 \mu\text{m}$ and $t=100 \mu\text{m}$) $S1^{\max}$ is found to be insensitive to any increase in the top coat thickness t or the bond coat thickness b selected. Fig. 4.5a shows that principal stress decreases exponentially with increasing undulation wavelength W and asymptotically approaches zero. This is confirmed by the fact that an undulation with infinite wavelength corresponds to a flat interface for which the $S1^{\max}$ principal stress is zero. For increasing amplitude A , there is first an increase in the principle stress and then exponential decay. Finally, the principal stress increases monotonically with the TGO thickness h .

Fig. 4.5b shows that $S1^{\max}$ linearly increases with increasing top coat modulus. The response is similar for increasing TGO modulus but with a much steeper slope. The graph also elucidates that a minor reduction in TGO modulus will prevent top coat crack initiation as $S1^{\max}$ decreases below rupture stress.

4.3.1 PARAMETRIC REPRESENTATION FOR CRACK INITIATION IN THE TOP COAT

From the summary of results in Fig. 4.5, the critical parameters selected are the top coat modulus E_{TC} , TGO thickness h and modulus E_{TGO} , undulation wavelength W and amplitude A . Based on their influence on $S1^{\max}$, the geometric parameters are reclassified into three basic non-dimensional groups h/h_0 , W/A and A/A_0 and the sensitivity study results are used to establish functional relations. The material parameters E_{TC} and E_{TGO} are assigned a linear function based on the linear response shown in Fig. 4.5b. All the individual functions are subsequently combined to derive the following functional dependence for the maximum principal stress:

$$S1_{\max} = c_1 \left(1 + c_2 \frac{h}{h_0} e^{-\frac{W}{4A}} \right) \left(\frac{\left(\frac{A}{A_0} \right)}{1 + \left(\frac{A}{A_0} \right)^2} \right) \left(1 + c_3 \frac{E_{TC}}{E^*} \right) E_{TGO} \quad (4.13)$$

where $A_0=1 \mu\text{m}$, $h_0=1 \mu\text{m}$, $E^*=100 \text{ GPa}$ and c_1-c_3 are constants. The constants in Eqn. 4.13 are evaluated using a least squares based best fit analysis of all FEM results with a tolerance of 15%. For stress and moduli expressed in GPa and lengths in μm , the constants are derived to be: $c_1=0.8124$, $c_2=5.000$ and $c_3=0.1320$.

4.4 PARAMETRIC INVESTIGATION OF TOP COAT CRACK PROPAGATION

The parametric relation for $S1^{\text{max}}$ established in Eqn. 4.13 predicts the crack initiation within the top coat, however its severity on failure is determined by its location. The cracks initiating at the interface would lead to large scale delamination and are considered critical, whereas the cracks initiating away from the interface are critical only if they propagate to the TGO-top coat interface. Hence, subsequent to crack initiation sensitivity analysis, crack propagation simulations are performed for 25 unique parametric combinations that resulted in cracks initiating away from the interface. Due to the evolutionary nature of the crack trajectory these simulations are performed iteratively with finite element mesh regeneration for each significant deviation in crack path. Initially, a linear crack path oriented normal to the principal axis is prescribed and laced with hysteretic cohesive elements. The optimal crack increment direction is evaluated using Eqn. 4.12 for each increment in crack length and when it deviates significantly

from prescribed path the simulation is terminated. Subsequently, the crack path is updated linearly along the incremental direction and finite element mesh is regenerated for the updated crack path. In addition to monitoring the incremental direction for crack propagation, the rate of crack propagation is also monitored for each increment.

4.4.1 VALIDATION OF TOP COAT CRACK PROPAGATION DIRECTION

Prior to performing the crack propagation investigation, a sensitivity study is conducted to estimate the effect of variation in crack propagation direction on the propagation rate. The sensitivity analysis is performed using a representative parametric combination with $A=10\ \mu\text{m}$, $W=40\ \mu\text{m}$, $h=4\ \mu\text{m}$, $E_{TGO}=400\ \text{GPa}$ and $E_{TC}=200\ \text{GPa}$. For this combination of parameters, crack initiates perpendicular to the symmetry axis at a normal distance of $6.35\ \mu\text{m}$ from the interface. Using the crack propagation angle in Eq. 4.12 crack should deviate by 1° from horizontal after propagating $5\ \mu\text{m}$ to location P shown in Fig. 4.2a. To evaluate the effect of incremental direction on propagation rate, in addition to the 1° determined by Eqn. 4.12, three distinct propagation angles 90° , 60° and 30° are prescribed at the crack tip. The results of subsequent crack propagation analyses show that the crack remains arrested at P for the propagation angles 90° , 60° and 30° but

propagates at an accelerating rate along the 1° direction. The results of crack propagation analyses for 30° and 90° are shown in Fig. 4.6a and 4.6b.

This study demonstrates a strong influence of incremental direction on propagation rate and also confirms that the propagation direction evaluated by Eqn. 4.12 is most favorable for crack propagation.

4.4.2 TOP COAT CRACK PROPAGATION RESULTS

Crack propagation simulations show that the crack trajectories do not undergo significant deviations and remain oriented along the initially prescribed linear path. Amongst all simulations the maximum deviation in crack path until the interface is observed to be 4° . Fig. 4.7 summarizes the results with a representative parametric combination of $A=10\ \mu\text{m}$, $W=40\ \mu\text{m}$, $h=4\ \mu\text{m}$ that initiates a crack at a perpendicular distance of $6.01\ \mu\text{m}$ from the interfacial trough. Fig. 4.7a shows the variation in incremental propagation direction as the crack propagates towards the interface along the initially prescribed linear crack path. It should be noted that incremental directions are negative, thus indicating the crack is deviating towards the undulation. Fig. 4.7b illustrates the corresponding rate of propagation measured as the crack extension per minute during the thermal cycle. The propagation rates increase as crack tip advances

towards the interface and achieves peak values in the vicinity of the interface. There is significant difference in the initial rates of propagation between different parametric combinations, however the propagation rate monotonically increases as crack tip approaches the interface and, for all cases achieves very high values at the interface.

These simulations conclude that the parametric combinations that initiate cracks away from the interface also assist in the crack propagation towards the TGO and top coat interface. However, since oblique angle of incidence makes it unclear whether the cracks reaching the interface will initiate delamination, such interactions are investigated next.

4.4.3 EFFECT OF TOP COAT CRACKS ON TGO AND TOP COAT INTERFACE DELAMINATION

First, the TGO and top coat interface is interlaced with cohesive elements to enable simulation of delamination. The cohesive parameters are chosen ($\sigma_{\max} = 1 \text{ GPa}$, $\delta_c = 1.0e-8$) such that the interface does not delaminate in the absence of the top coat crack. Fig. 4.8 shows an excellent agreement of the top coat stresses for perfectly bonded interface and interface laced with stiff cohesive zone. Such a stiff cohesive zone isolates the influence of top coat cracks on delamination and also represents the interface conservatively.

Next, top coat crack propagation simulations are repeated with crack trajectories reaching the interface which is laced with a stiff cohesive zone. Fig. 4.9 shows the eventual crack trajectories for representative geometries a). $A=10\ \mu\text{m}$, $W=30\ \mu\text{m}$, $h=6\ \mu\text{m}$ and b). $A=10\ \mu\text{m}$, $W=30\ \mu\text{m}$, $h=4\ \mu\text{m}$. In both cases the crack propagates along a horizontal path and intersects the interface at an oblique angle and subsequently initiates delamination extending away from undulation trough. This scenario is typical for all crack propagation simulations and in each case the interfacial delamination extended only towards the planar interface leaving the remaining interface within the undulation intact. It should be noted that the crack propagation towards the interface is dominated by mode I, however, after reaching the interface the delamination is dominated by mode II. Hence, a change in dominant modality of crack propagation is observed as the crack intersects the interface between top coat and TGO.

4.5 COMPARISON OF NUMERICAL PREDICTION WITH EXPERIMENTS

As a final step, the predictions of finite element simulations are compared to the top coat crack trajectories observed in real microstructures. Simulations are performed for TBC geometric parameters obtained from SEM micrograph in [7] and nominal material parameters $E_{TGO} = 400$ GPa, $E_{TC} = 200$ GPa and $\sigma_{max} = 287$ MPa. The finite element simulation predicts that the crack initiates at a perpendicular distance of $6.38 \mu\text{m}$ from the interfacial trough and propagates to reach the TGO and top coat interface. Consequently, the interfacial delamination initiates at the site of intersection and extends towards the planar interface leaving the remaining interface within the undulation intact. This prediction closely matches the experimental observation demonstrating the capability of the proposed modeling framework to accurately predict failure scenarios. The excellent agreement between the crack trajectory observed in the SEM and finite element simulation is shown in Fig. 4.10.

4.6 CONCLUSIONS

In this chapter, failure of TBCs due to delaminations along susceptible interface between TGO and top coat is investigated using finite element models. The work focuses on crack initiation and propagation within the top coat that is postulated to be responsible for catastrophic failure of TBC system.

The top coat crack initiation is investigated using a thermo-elastic finite element model with bond coat creep. Crack is assumed to initiate when maximum principal stress exceeds rupture stress of the top coat. A sensitivity analysis estimates the contribution of geometric and material parameters and forms a basis to develop parametric relation to estimate maximum principal stress. The parametric relation delineates the parametric combinations that are susceptible to damage.

Subsequently, crack propagation simulations using a finite element model with embedded hysteretic cohesive zone model are performed for parametric combinations which initiate cracks away from the interface. These analyses conclude that parametric combinations initiating top coat cracks also assist in propagation and eventual delamination of TGO and top coat interface. The materials and geometries in the study are chosen to be representative of TBC materials in real applications.

The chapter concludes with finite element simulations of a representative failure scenario from the literature. The geometry and material properties for this case are obtained from the literature and nominal material properties are selected for simulation. The crack trajectory predicted by simulation is found to be in good agreement with crack trajectory observed in SEM images.

Although the present study characterizes the top coat damage evolution and propagation in detail, the validity is limited to damage initiating in an idealized, defect free isotropic top coat. The top coat in real applications is anisotropic and quite heterogeneous with multiple defects [15]. The effect of the top coat microstructural defects on the overall failure of TBCs will be investigated in the next chapter.

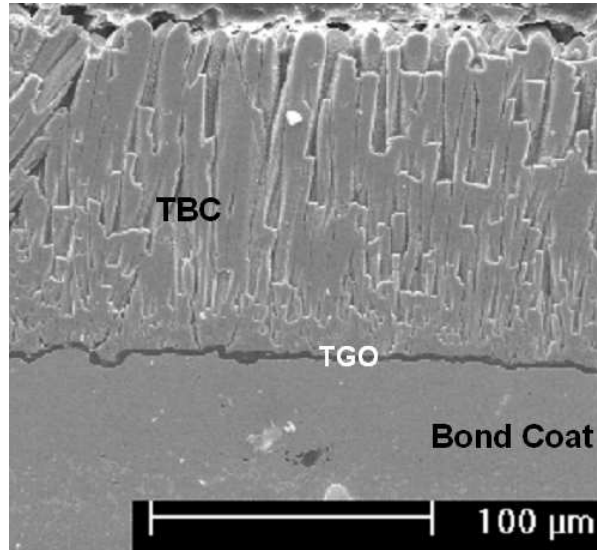


Figure 4.1: An SEM image of the TBC microstructure consisting of the top coat, the thermally grown oxide layer, the bond coat and the super-alloy substrate [20].

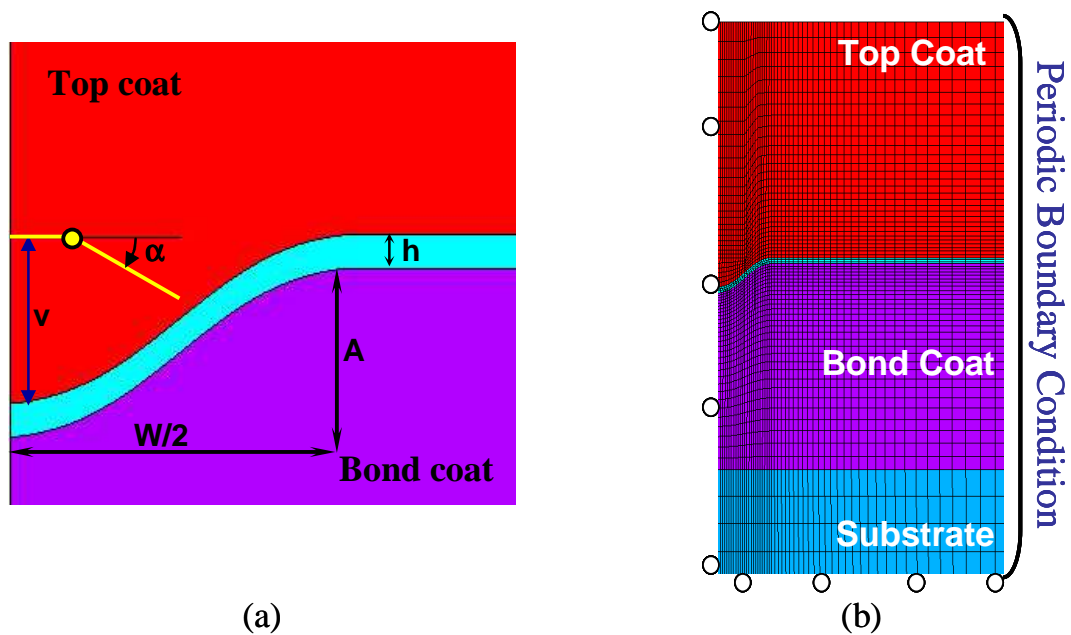


Figure 4.2: Schematic diagrams showing (a) geometric and dimensional parameters (b) finite element model (not to scale) of the TBC system with boundary conditions.

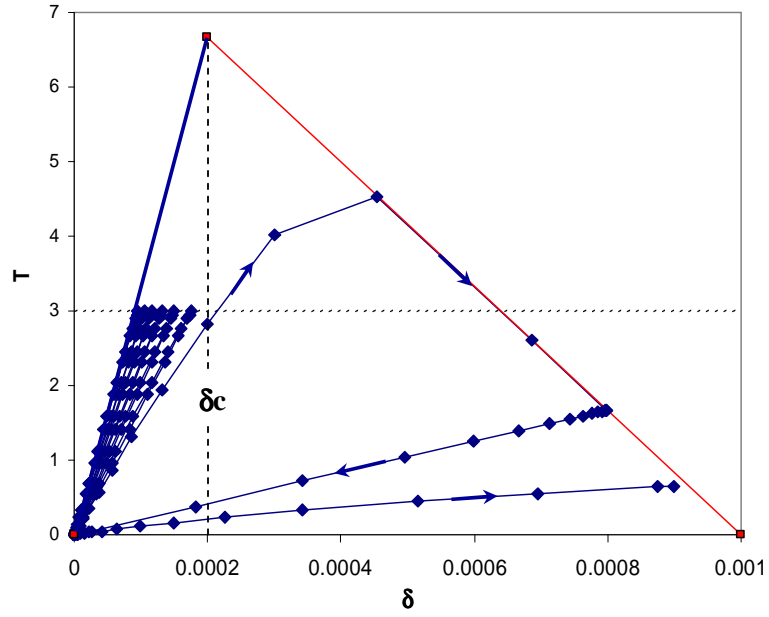


Figure 4.3: A plot showing the hysteretic cohesive zone element response with cyclic loading to eventual failure when $\delta=\delta_e=0.001$

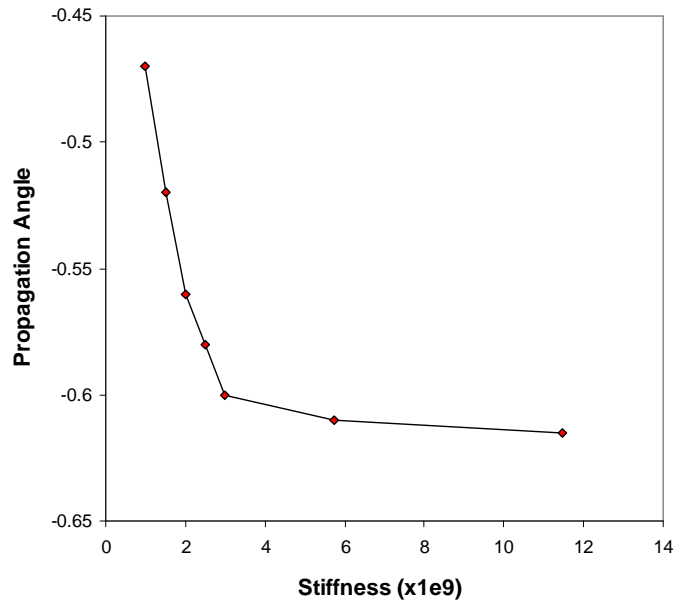
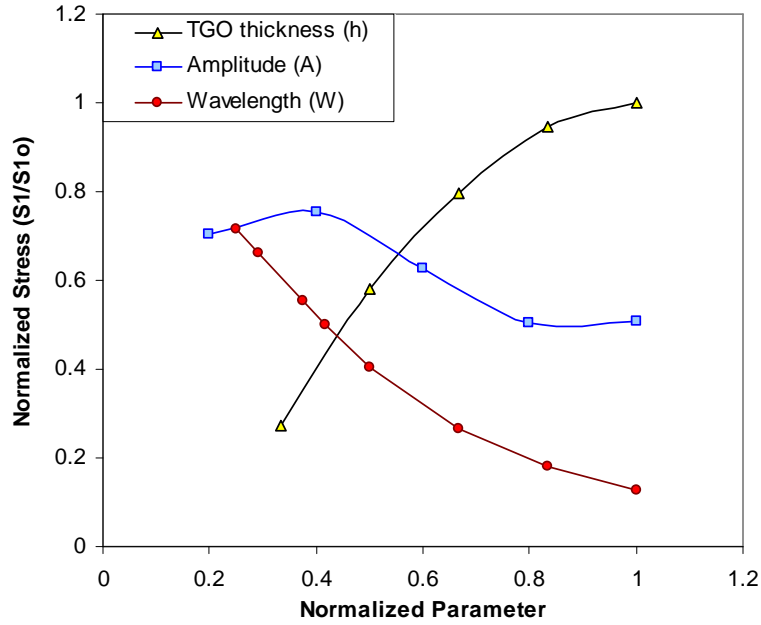
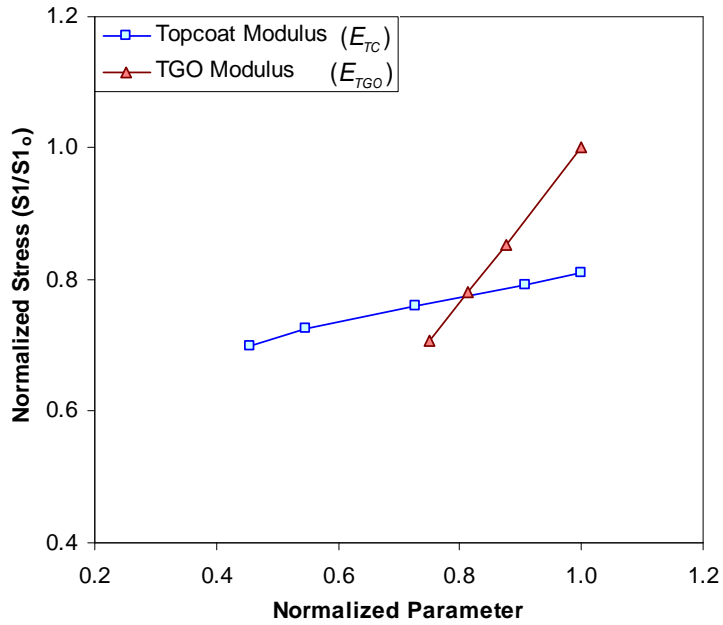


Figure 4.4: Plot showing the convergence of crack propagation angle with increasing cohesive stiffness (σ_{max}/δ_e)

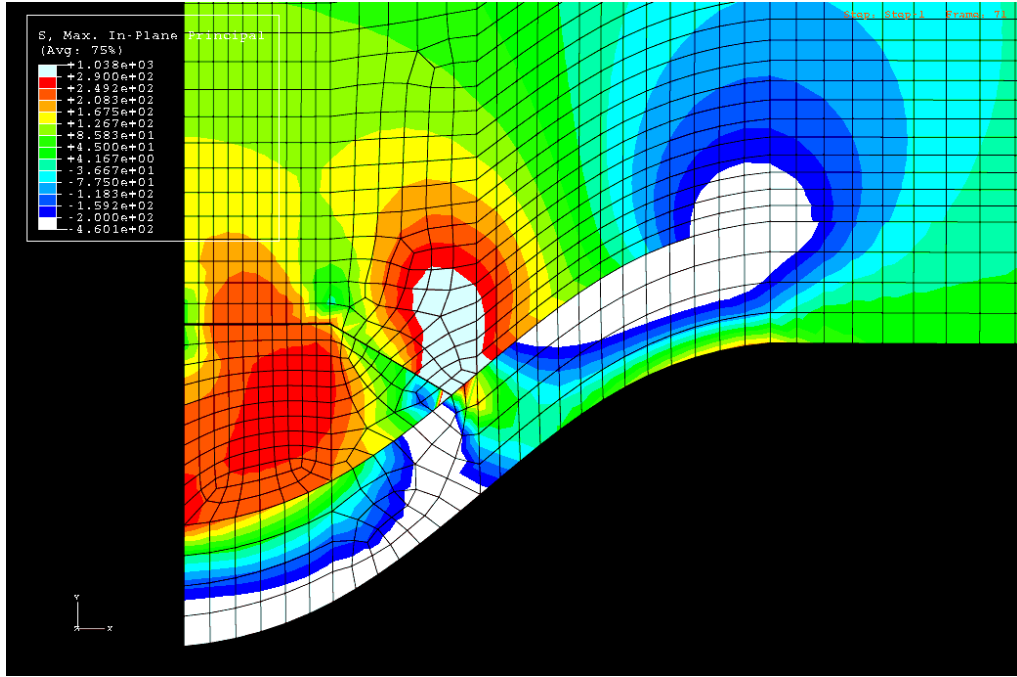


(a)

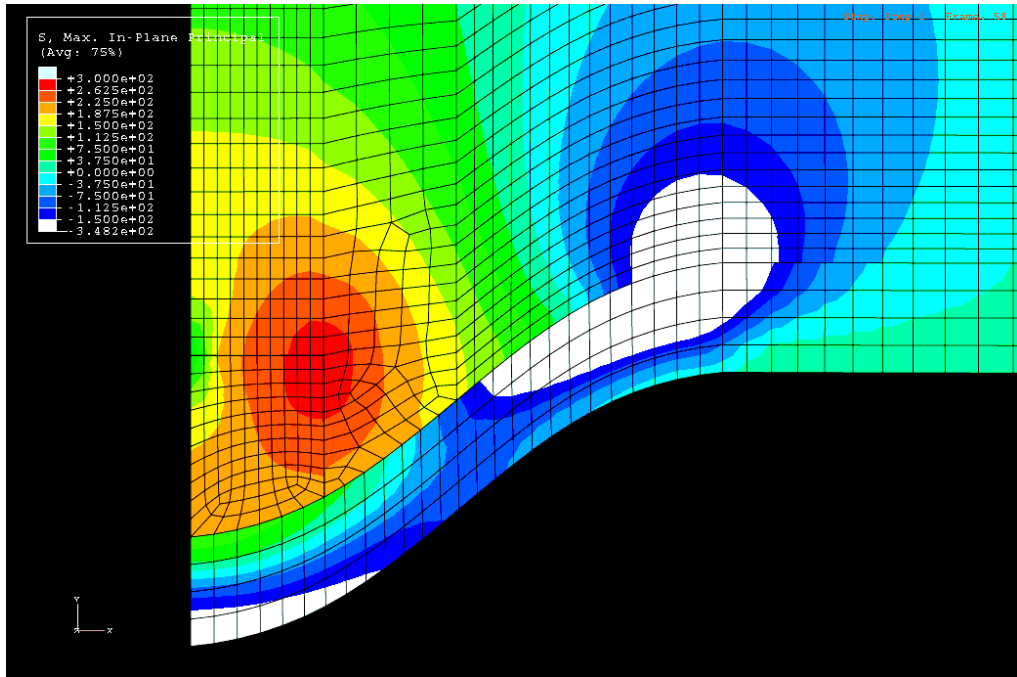


(b)

Figure 4.5: Plots showing top coat principal stress sensitivity to (a) geometric parameters (normalizing values of $h_{max}=6 \mu\text{m}$, $A_{max}=25 \mu\text{m}$, $W_{max}=120 \mu\text{m}$, and $SI_0=604 \text{ MPa}$), (b) material parameters (normalizing values of $E_{TGO}^{max}=400 \text{ GPa}$, $E_{TC}^{max}=220 \text{ GPa}$ and $SI_0=410.89 \text{ MPa}$)

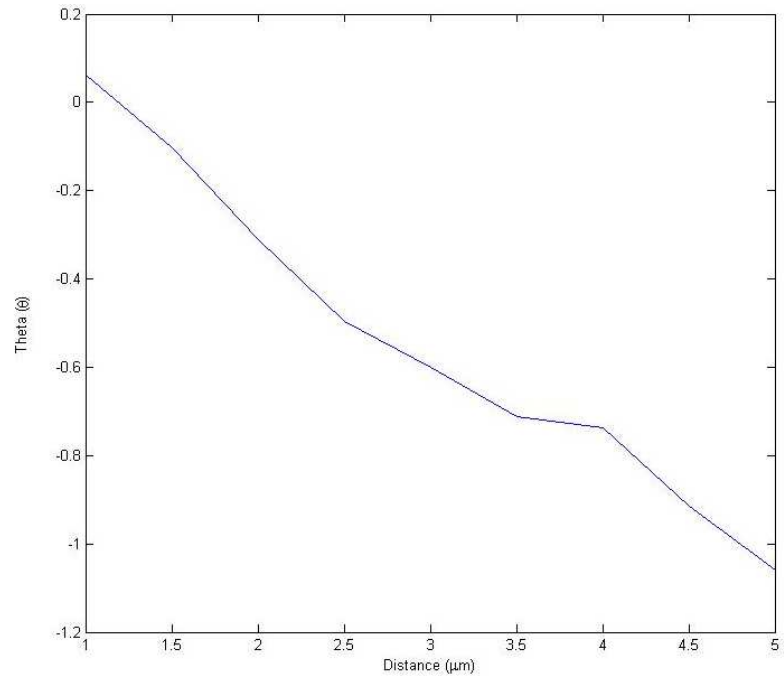


(a)

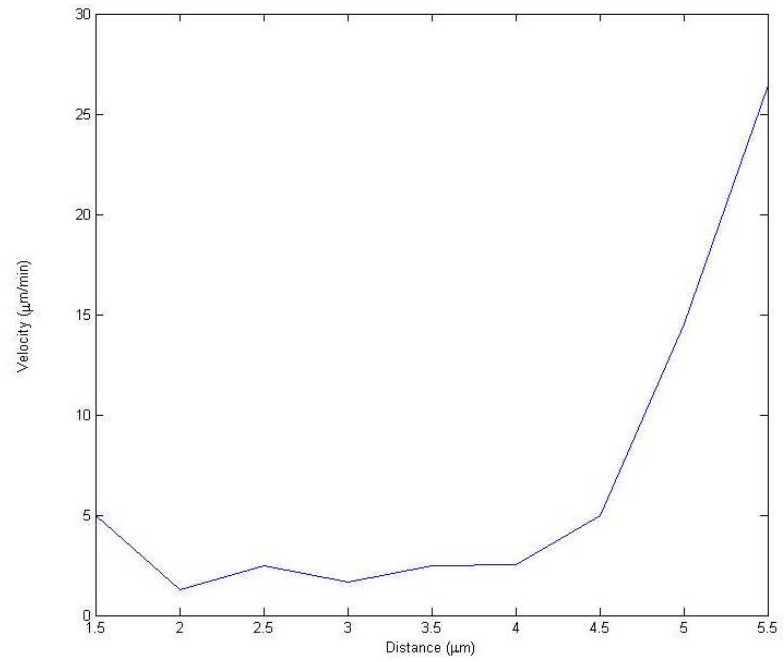


(b)

Figure 4.6: Plots of principal stress contours showing crack arrest when prescribed path deviates by (a) 30 degrees and (b) 90 degrees from that predicted by Eqn. (5).

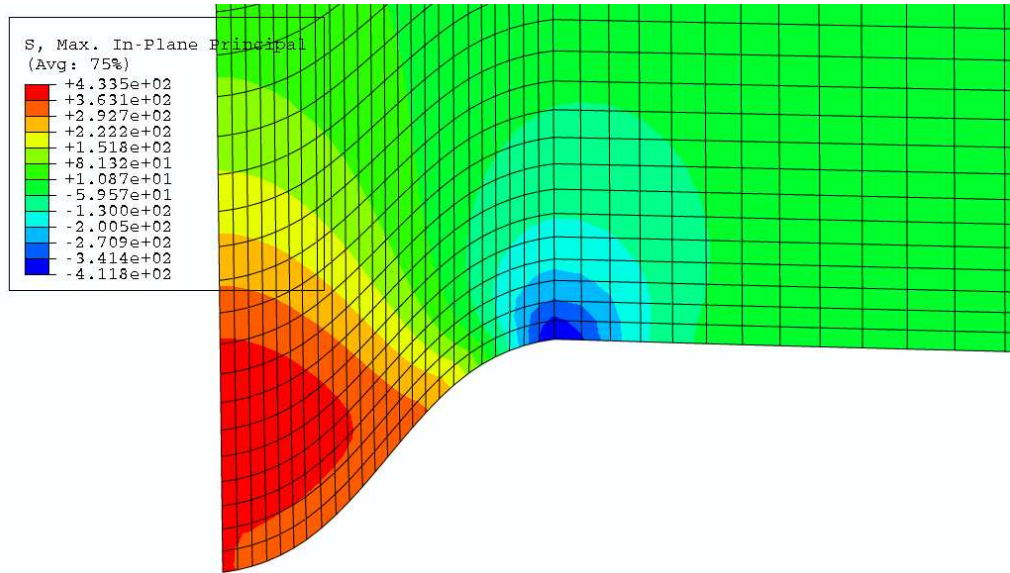


(a)

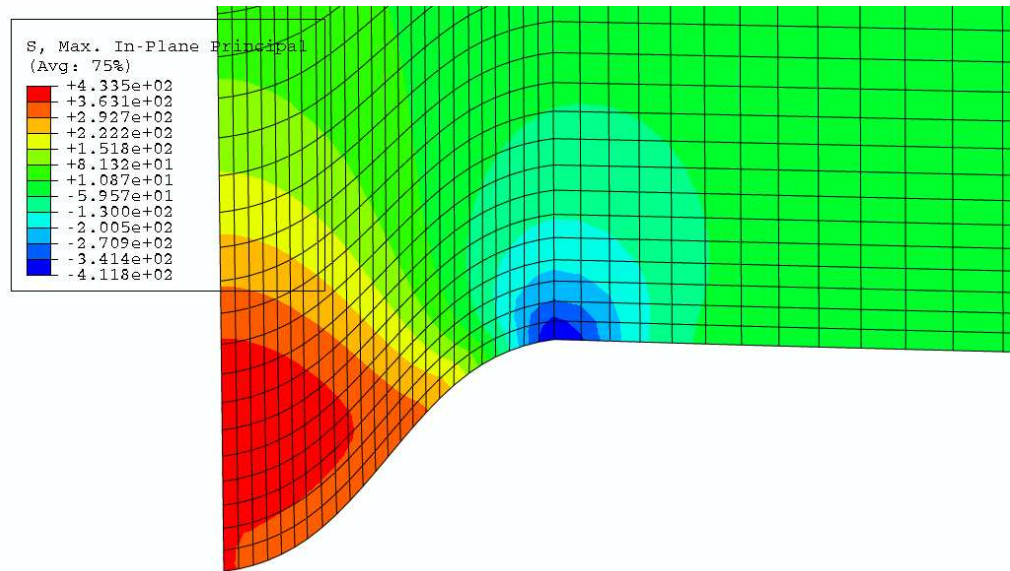


(b)

Figure 4.7: Plots showing the variation in (a) incremental crack propagation direction and (b) crack propagation rate as the crack propagates along an initially assigned path towards the interface.

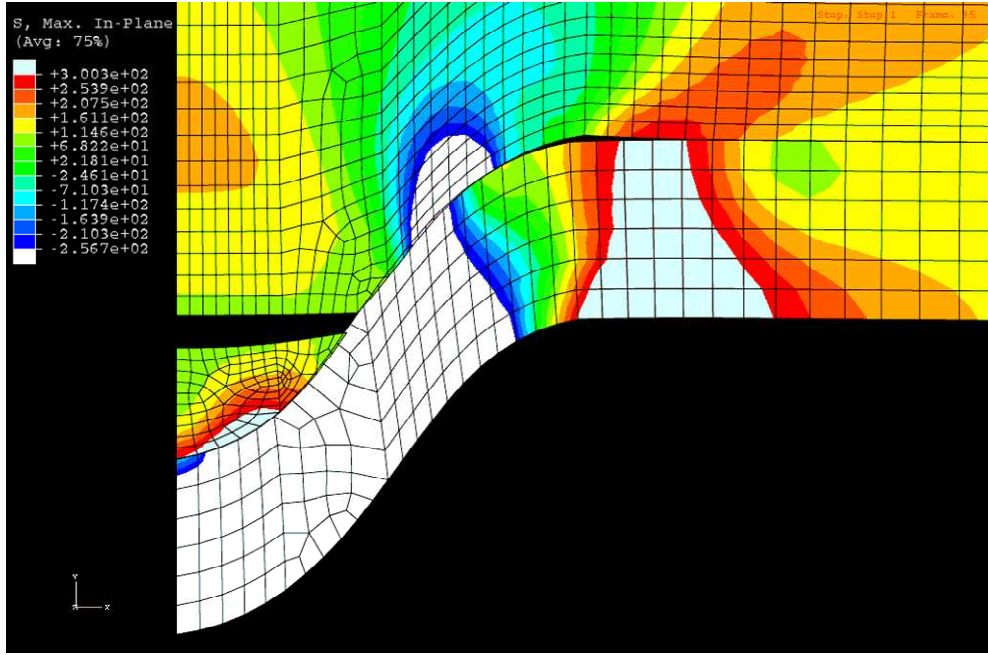


(a)

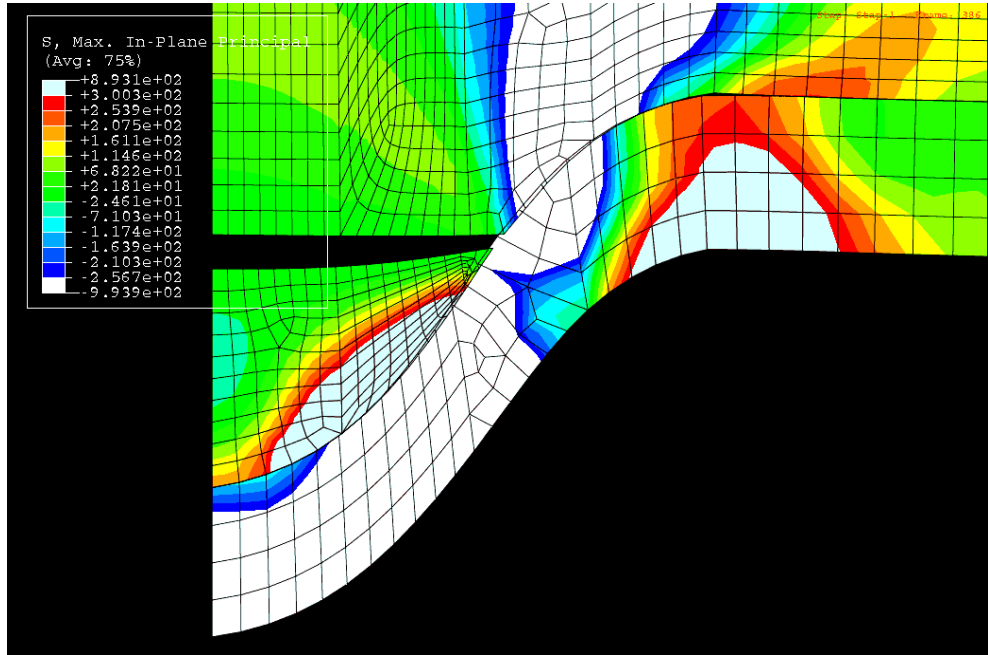


(b)

Figure 4.8: Plots showing the topcoat principal stress contours when topcoat and TGO interface is (a) perfectly bonded and (b) laced with very stiff cohesive zone elements.



(a)



(b)

Figure 4.9: Principal stress contour plots showing crack trajectories for TBC geometry defined by (a) $A=10$ mm, $W=20$ mm and $h=6$ μm and (b) $A=10$ μm , $W=30$ μm , $h=4$ μm

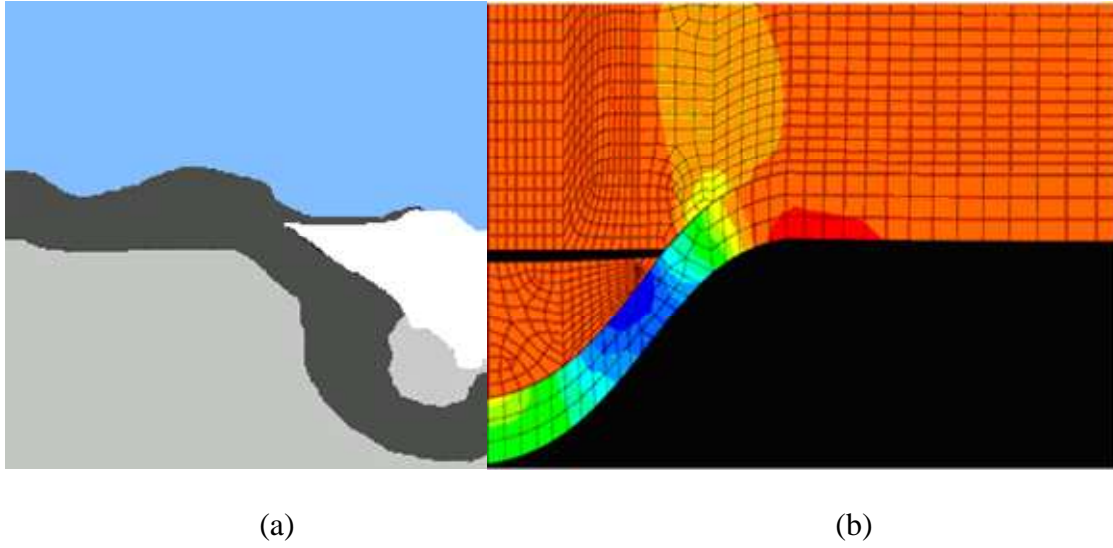


Figure 4.10: Comparison of top coat crack trajectory (a) schematic of SEM micrograph observations [7] with (b) finite element simulation. The geometric parameters are $A=10 \mu\text{m}$, $W=30 \mu\text{m}$, $t=3 \mu\text{m}$

CHAPTER 5

A HOMOGENIZATION BASED CONTINUUM DAMAGE MECHANICS MODELING FRAMEWORK FOR THERMAL BARRIER COATINGS

5.1 INTRODUCTION

Based on experimental observations it has been postulated [15] that top coat microstructure with large number of micro-defects are prone to damage evolution. The discrete discontinuities in the top coat may propagate and coalesce resulting in TBC failure. As seen in Fig. 5.1, due to the diffused nature of top coat micro-cracks a representative volume element (RVE) can simulate mechanical response of the top coat. An RVE forms the basis of utilizing the homogenization based continuum damage mechanics model (HCDM)[16]. Although HCDM is primarily developed for damage in heterogeneous composite materials, it can be utilized for top coat damage with some restrictions. Micromechanical damage in the representative volume element (RVE) is

explicitly incorporated in the form of cohesive cracks in a homogeneous material. The model uses an evolving principal damage coordinate system as its reference in order to represent the anisotropic damage coefficients. This is essential for accurate simulations as cracks propagate along complex trajectories introducing anisotropic damage. The material constitutive law involves a fourth order orthotropic tensor with stiffness characterized as a macroscopic internal variable. Damage in the top coat is accounted for through the fourth order damage tensor populated with functional forms that are written in terms of macroscopic strain components.

Due to morphological and constitutive complexities that govern its growth, numerical analysis and simulation of the growth of multiple cracks in the top coat is a challenging enterprise. Since the element formulation does not account for high stress gradients and singularities, the conventional finite element method suffers from very slow convergence and requires fine mesh structures. In this chapter, an extended Voronoi cell finite element method (X-VCFEM) developed by Li and Ghosh [17, 18] is employed for modeling the growth of multiple cohesive cracks in the top coat. The model accounts for interaction between cracks and invokes an adaptive crack growth formulation to represent the continuously changing direction of evolving cracks.

X-VCFEM augments the conventional VCFEM model by incorporating multi-resolution wavelet functions [62-64] in the vicinity of the crack tip. The incremental crack propagation direction and length are adaptively determined by a cohesive energy based criterion. No remeshing is needed in X-VCFEM for simulating crack growth, and this increases the accuracy and effectiveness of X-VCFEM. The formulation and various capabilities of X-VCFEM are explained in detail by Li and Ghosh in [17, 18, 65, 66] and will be briefly summarized in following sections.

This chapter starts with a brief discussion of the X-VCFEM formulation followed by two numerical examples to demonstrate the distinctive capabilities of this method. A brief introduction of HCDM [16, 19] is presented next with details of its unique features. Finally, the results of a parametric study to determine applicable range of validity of HCDM for TBCs are summarized,

5.2 VORONOI CELL FINITE ELEMENT ASSUMPTIONS AND WEAK FORM

Consider a schematic of a typical representative volume of top coat Ω consisting of N cracks shown in Fig. 5.2a. The volume is partitioned into a mesh of Voronoi polytopes. The Voronoi cells surrounding each heterogeneity are generated by a surface based tessellation algorithm [67, 68]. Each element in VCFEM consists of the heterogeneity and its neighboring material contained in a Voronoi cell element Ω_e . A schematic of a typical Voronoi cell element Ω_e containing a crack and its neighboring material is shown in Fig. 5.2b. The element boundary $\partial\Omega_e$ with outward normal \mathbf{n}^E may consist of regions with prescribed traction Γ_{te} , prescribed displacement Γ_{ue} and inter-element edges Γ_{me} . Thus, $\partial\Omega_e = \Gamma_{te} \cup \Gamma_{ue} \cup \Gamma_{me}$. Furthermore, each element is assumed to contain a crack with a fracture process zone represented by a cohesive zone model.

In order to describe the discontinuity across the crack, stress interpolation in the element is divided into the two parts, Ω_e^1 and Ω_e^2 , on opposite sides of the crack path. An incompatible displacement field is facilitated across the crack (Γ_{cr}) through a set of connected node-pairs. Traction continuity on the intra-element boundaries (Γ_{int}) is satisfied by weak form Lagrangian multipliers. $\partial\Omega_e$ has an outward normal \mathbf{n}^e , while \mathbf{n}^{cr} and \mathbf{n}^i are the outward normals for cracks and intra-element boundaries. The

equilibrated stress field is set to σ ; u^e , u^m , and u^t denote kinematically admissible displacement fields on $\partial\Omega_e$, crack and intra-element boundaries excluding crack paths, respectively. The notations $(\bullet)^1$ and $(\bullet)^2$ represent two different subregions of Ω_e , and the prefix Δ implies increments. A complementary energy functional in incremental form for one element may be given in terms of increments of stress and boundary displacement fields as

$$\begin{aligned}
\Pi_e = & \frac{1}{2} \int_{\Omega_e^1} (\sigma_{ij}^1 + \Delta \sigma_{ij}^1) S_{ijkl} (\sigma_{ij}^1 + \Delta \sigma_{ij}^1) d\Omega + \frac{1}{2} \int_{\Omega_e^2} (\sigma_{ij}^2 + \Delta \sigma_{ij}^2) S_{ijkl} (\sigma_{ij}^2 + \Delta \sigma_{ij}^2) d\Omega \\
& - \int_{\partial\Omega_e^1} (\sigma_{ij}^1 + \Delta \sigma_{ij}^1) n_j^e (u_i^e + \Delta u_i^e) d\partial\Omega - \int_{\partial\Omega_e^2} (\sigma_{ij}^2 + \Delta \sigma_{ij}^2) n_j^e (u_i^e + \Delta u_i^e) d\partial\Omega \\
& - \int_{\Gamma_{cr}^1} (\sigma_{ij}^1 + \Delta \sigma_{ij}^1) n_j^{cr} (u_i^e + \Delta u_i^e) d\Gamma_{cr} + \int_{\Gamma_{cr}^2} (\sigma_{ij}^2 + \Delta \sigma_{ij}^2) n_j^{cr} (u_i^e + \Delta u_i^e) d\Gamma_{cr} \\
& - \int_{\Gamma_{int}} (\sigma_{ij}^1 + \Delta \sigma_{ij}^1 - \sigma_{ij}^2 - \Delta \sigma_{ij}^2) n_j^t (u_j^t + \Delta u_j^t) d\Gamma_{int} + \int_{\Gamma_{tm}^1} \bar{T}_i (u_i^e + \Delta u_i^e) d\Gamma_{tm} \\
& + \int_{\Gamma_{tm}^2} \bar{T}_i (u_i^e + \Delta u_i^e) d\Gamma_{tm} - \int_{\Gamma_{cr}} \int_0^{\mathbf{u} + \Delta \mathbf{u} - \mathbf{u} - \Delta \mathbf{u}} T_i^{coh} d(u_i + \Delta u_i - u_i - \Delta u_i) d\Gamma_{cr}
\end{aligned} \tag{5.1}$$

The last term provides the work done by the crack tractions $T^{coh} = T_n^{coh} \mathbf{n} + T_t^{coh} \mathbf{t}$ due to crack separation $(\mathbf{u} - \mathbf{u})^1$, where T_n^{coh} and T_t^{coh} are normal and tangential components of the crack traction. The total complementary energy may be obtained by adding the energy in N elements

$$\Pi = \sum_{e=1}^N \Pi_e \tag{5.2}$$

The VCFEM formulation is based on the assumed stress hybrid finite element method. In this method, letting the variation Π_e with respect to stress increments $\Delta \boldsymbol{\sigma}^1$ and $\Delta \boldsymbol{\sigma}^2$ be zero, yields the element displacement compatibility relations as:

$$\begin{aligned}
& -\int_{\Omega_e} \left(\frac{\partial \Delta B}{\partial \Delta \sigma_{ij}} + \varepsilon_{ij} \right) \delta \Delta \sigma_{ij} d\Omega + \int_{\partial \Omega_e} \delta \Delta \sigma_{ij} n_j^E (u_i^E + \Delta u_i^E) d\partial \Omega \\
& + \int_{\Gamma_{cr}^1} \delta \Delta \sigma_{ij} n_j^{cr} ({}^1 u_i^{cr} + \Delta {}^1 u_i^{cr}) d\Gamma_{cr} - \int_{\Gamma_{cr}^2} \delta \Delta \sigma_{ij} n_j^{cr} ({}^2 u_i^{cr} + \Delta {}^2 u_i^{cr}) d\Gamma_{cr} = 0
\end{aligned} \tag{5.3}$$

Solution of Eqn. 5.3 yields domain stresses in the Voronoi cell. In the VCFEM formulation, the equilibrium conditions and constitutive relations in the material and the compatibility conditions on the element boundary and crack surfaces are satisfied *a priori* in a strong sense. However, the element kinematic equation is satisfied in a weak sense. Furthermore, the VCFEM formulation assumes weak satisfaction of the traction reciprocity conditions on (i) the interelement boundary Γ_{me} , and (ii) the domain traction boundary Γ_{te} , and (iii) the crack surfaces Γ_{cr}^1 and Γ_{cr}^2 . Using the variational principle, traction reciprocity conditions on the element boundaries are obtained by setting the first variation of the total complementary energy Π with respect to the displacements $\Delta \mathbf{u}^e$, $\Delta \mathbf{u}^m$, $\Delta \mathbf{u}^e$, $\Delta \mathbf{u}^m$, and $\Delta \mathbf{u}^f$ equal to zero.

5.3 CREATION OF ENRICHED STRESS FUNCTIONS IN X-VCFEM

Independent assumptions on stress increments are made in the two subregions, Ω_e^1 and Ω_e^2 , to accommodate stress jumps across the crack. In two-dimensional analysis, Airy's stress function $\Phi(x, y)$ is a convenient tool for deriving equilibrated stress fields. Important micromechanics observations, that stress concentrations depend on the heterogeneity, have been incorporated in the choice of stress functions. Two conditions need to be considered in the choice of stress functions [18]. The first is that the stress functions should adequately represent the high concentration at the crack tips. Polynomial functions alone are unable to satisfy this requirement and hence suffers from poor convergence [65]. The second condition is that the stress function should account for stress jump across the crack surface.

In view of the existence of crack tips, the stress functions are decomposed into three different components, namely: (a) a purely polynomial function Φ^{poly} to yield the far field stress distributions away from the crack tip, (b) a branch function Φ^{branch} that is constructed from level set functions, and (c) a multi-resolution wavelet function Φ^{wvl} to account for the moving crack tip stress concentration. Thus the complete stress function becomes:

$$\Phi = \Phi^{poly} + \Phi^{branch} + \Phi^{wit} \quad (5.4)$$

5.3.1 PURE POLYNOMIAL FORMS OF STRESS FUNCTION

The pure polynomial function Φ^{poly} is written as

$$\Phi^{poly} = \sum_{p,q} \xi^p \eta^q \beta_{pq} \quad (5.5)$$

where (ξ, η) corresponds to scaled local coordinates with the origin at the element centroid (x_c, y_c) , written as $\xi = (x - x_c)/L$, $\eta = (y - y_c)/L$ and the scale parameter $L = \sqrt{\max(x - x_c) \times \max(y - y_c)}$ $\forall (x, y) \in \partial\Omega_e$. The use of the local coordinates (ξ, η) instead of global coordinates (x, y) in the construction of stress functions prevents ill conditioning of the stiffness matrix incurred through discrepancies due to high exponents of (x, y) in Φ^{poly} [65].

5.3.2 BRANCH STRESS FUNCTIONS USING LEVEL SET METHODS

The branch function Φ^{branch} facilitates jumps in stresses across the crack surfaces. The branch function should not affect the solutions in the continuous region beyond the crack. This construction requires a functional representation of the surface or line of

discontinuity. The discontinuous surface is expressed by a signed distance function $f(x)$ defined as [65]:

$$f(x) = \min_{x \in \Gamma} \|x - \bar{x}\| \text{sign}(n^+ \cdot (x - \bar{x})) \quad (5.6)$$

Radial distance functions to the two crack tips $r_1(x)$ and $r_2(x)$ and the corresponding angular positions $\theta_1(x)$ and $\theta_2(x)$ are depicted in are expressed in terms of coordinates of local systems (ξ, η) with origins at the crack tips. The branched stress function is constructed in terms of the functions $f(x)$, $r_1(x)$, $\theta_1(x)$ and $r_2(x)$, $\theta_2(x)$ as [18]:

$$\Phi^{branch} = \sum_{s,t} r_1^2 \sin(\theta_1/2) r_2^2 \cos(\theta_2/2) \xi^s \eta^t \beta_{st} \quad (5.7)$$

The terms r_1^2 and r_2^2 in Φ^{branch} are necessary for avoiding crack tip singularities in the stresses due to this function and for improving the accuracy. Along the tangential extension to the crack path at the first tip Φ^{branch} is zero. Hence Φ^{branch} does not contribute to the stresses ahead of the first crack tip. In an analogous manner, Φ^{branch} goes to zero along the extension to the crack path at the second tip. However, along the crack surface between the two crack tips, Φ^{branch} is discontinuous across the crack path.

5.3.3 MULTI-RESOLUTION WAVELET BASED STRESS FUNCTIONS

The wavelet based stress function is constructed in a local orthogonal coordinate system (ξ, η) , centered at the crack tip. The ξ direction corresponds to the local tangent to the crack surface. The corresponding stress function $\Phi_{a,b,c,d}$ in the Gaussian wavelet basis is given as [18]:

$$\Phi_{a,b,c,d}(\xi, \eta) = e^{-\frac{(\xi-b)^2}{2a}} e^{-\frac{(\eta-d)^2}{2c}} \beta_{a,b,c,d} \quad (5.8)$$

where a , b , c , and d are parameters that can take arbitrary continuous values. The dilatational (a,c) and translation (b,d) can vary in a continuous manner. Translation parameters allow wavelet bases to closely follow the crack tip. The dilatation parameters with compact adjustable window support can be used to provide high refinement and resolution near the crack tip [17]. For implementation in multi-resolution analysis involving discrete levels, the translation and dilation parameters should be expressed as discrete multiples of some starting values. Consequently, these discrete values a_m , b_n , c_k and d_l are expressed as [65]:

$$\begin{cases} a_m = a_1 \cdot (tr_a)^{m-1} \\ b_n = n \cdot b_1 \cdot a_m \\ c_k = c_1 \cdot (tr_c)^{k-1} \\ d_l = l \cdot d_1 \cdot c_k \end{cases} \quad (5.9)$$

Here (m,k) correspond to the levels and (n,l) correspond to the discrete translation of the bases in the (ξ,η) basis directions respectively. The parameters (a_l,c_l) are the initial dilating values at the first level $m=1$, while tr_a , and tr_c are the transfer rates from one level to the next higher one. The parameters (b_l,d_l) represent the starting values of a step translation quantity at the m^{th} dilation level. With the specific relations between dilation and translation parameters expressed in Eqn. 5.9, the Gaussian wavelet enriched stress function in Eqn. 5.8 becomes

$$\Phi^{wvlt} = \sum_{m,n,k,l} e^{-\frac{1}{2} \left(\frac{\xi - b_n}{a_m} \right)^2} e^{-\frac{1}{2} \left(\frac{\eta - d_l}{c_k} \right)^2} \beta_{m,n,k,l} \quad (5.10)$$

The family of wavelet enriched stress functions in Eqn. 5.10 are not orthonormal, but they construct a linearly independent basis [69]. This leads to robustness and high precision in the reconstruction of any function f even with low level coefficients. The wavelet enriched stress function in X-VCFEM is thus written as

$$\Phi^{wvlt}(\xi, \eta) = \sum_{m,n,k,l} \Phi_{m,n,k,l}(\xi, \eta) \quad (5.11)$$

Stresses can be obtained by differentiating $\Phi^{wvlt}(\xi, \eta)$:

$$\begin{pmatrix} \Delta\sigma_{xx} \\ \Delta\sigma_{yy} \\ \Delta\sigma_{xy} \end{pmatrix} = \begin{pmatrix} \frac{\partial^2 \Delta\Phi^{wvlt}(\xi, \eta)}{\partial \eta^2} \\ \frac{\partial^2 \Delta\Phi^{wvlt}(\xi, \eta)}{\partial \xi^2} \\ -\frac{\partial^2 \Delta\Phi^{wvlt}(\xi, \eta)}{\partial \xi \partial \eta} \end{pmatrix} = \begin{pmatrix} \sum_{m,n,k,l} \frac{\partial^2 e^{-\frac{(\xi-b_n)^2}{a_m}} e^{-\frac{(\eta-d_l)^2}{c_k}}}{\partial \eta^2} \Delta\beta_{m,n,k,l} \\ \sum_{m,n,k,l} \frac{\partial^2 e^{-\frac{(\xi-b_n)^2}{a_m}} e^{-\frac{(\eta-d_l)^2}{c_k}}}{\partial \xi^2} \Delta\beta_{m,n,k,l} \\ -\sum_{m,n,k,l} \frac{\partial^2 e^{-\frac{(\xi-b_n)^2}{a_m}} e^{-\frac{(\eta-d_l)^2}{c_k}}}{\partial \xi \partial \eta} \Delta\beta_{m,n,k,l} \end{pmatrix} \quad (5.12)$$

In summary, the stresses in an element are computed by adding contributions from equations (5.5), (5.7), and (5.11), to yield

$$\begin{pmatrix} \sigma_{xx} \\ \sigma_{yy} \\ \sigma_{xy} \end{pmatrix} = \begin{pmatrix} \sigma_{xx} \\ \sigma_{yy} \\ \sigma_{xy} \end{pmatrix}^{poly} + \begin{pmatrix} \sigma_{xx} \\ \sigma_{yy} \\ \sigma_{xy} \end{pmatrix}^{branch} + \begin{pmatrix} \sigma_{xx} \\ \sigma_{yy} \\ \sigma_{xy} \end{pmatrix}^{wvlt} = \begin{pmatrix} \beta_{pq} \\ \beta_{st} \\ \beta_{m,n,k,l} \end{pmatrix} = [P]_e \{\beta\}_e \quad (5.13)$$

5.4 X-VCFEM SOLUTION METHOD

Propagation of multiple cracks is solved using an incremental approach, where a set of elemental and global equations are solved in each increment for stresses and

displacements. Stress increments are obtained by differentiating the stress functions

$\Phi(x, y)$ to produce

$$\begin{Bmatrix} \Delta\sigma_{xx} \\ \Delta\sigma_{yy} \\ \Delta\sigma_{xy} \end{Bmatrix} = \begin{Bmatrix} \frac{\partial^2 \Delta\Phi}{\partial y^2} \\ \frac{\partial^2 \Delta\Phi}{\partial x^2} \\ -\frac{\partial^2 \Delta\Phi}{\partial x \partial y} \end{Bmatrix} = [\mathbf{P}]\{\Delta\boldsymbol{\beta}\} \quad (5.14)$$

Considering the two different subregions on opposite sides of the crack path, we have

$\{\Delta\boldsymbol{\sigma}\}^1 = [\mathbf{P}]\{\Delta\boldsymbol{\beta}\}^1$ and $\{\Delta\boldsymbol{\sigma}\}^2 = [\mathbf{P}]\{\Delta\boldsymbol{\beta}\}^2$. Interpolating the nodal displacements on the

boundaries using standard linear or reinforced hierarchical shape functions generates

compatible displacement increments $\{\Delta\boldsymbol{u}^e\}^1 = [\mathbf{L}_e]\{\Delta\boldsymbol{q}^e\}^1$ on $\partial\Omega_e^1$ and $\{\Delta\boldsymbol{u}^e\}^2 = [\mathbf{L}_e]\{\Delta\boldsymbol{q}^e\}^2$ on

$\partial\Omega_e^2$, $\{\Delta\boldsymbol{u}^m\}^1 = [\mathbf{L}_m]\{\Delta\boldsymbol{q}^m\}^1$ on Γ_{cr}^1 , $\{\Delta\boldsymbol{u}^m\}^2 = [\mathbf{L}_m]\{\Delta\boldsymbol{q}^m\}^2$ on Γ_{cr}^2 and $\{\Delta\boldsymbol{u}^i\} = [\mathbf{L}_i]\{\Delta\boldsymbol{q}^i\}$ on Γ_{int}

[65]. Substituting the relations for stress and displacement increment interpolation in

Eqn. 5.1 gives the complimentary energy as:

$$\begin{aligned}
\Pi_e = & \frac{1}{2} \{\beta + \Delta\beta\}^T [\mathbf{H}] \{\beta + \Delta\beta\} + \frac{1}{2} \{\beta + \Delta\beta\}^T [\mathbf{H}] \{\beta + \Delta\beta\} \\
& - \{\beta + \Delta\beta\}^T [\mathbf{G}^e] \{q^e + \Delta q^e\} - \{\beta + \Delta\beta\}^T [\mathbf{G}^e] \{q^e + \Delta q^e\} \\
& + \{\bar{\mathbf{T}}\}^T \{q^e + \Delta q^e\} - \{\beta + \Delta\beta\}^T [\mathbf{G}^t] \{q^t + \Delta q^t\} + \{\bar{\mathbf{T}}\}^T \{q^e + \Delta q^e\} \\
& - \{\beta + \Delta\beta\}^T [\mathbf{G}^m] \{q^m + \Delta q^m\} + \{\beta + \Delta\beta\}^T [\mathbf{G}^m] \{q^m + \Delta q^m\} \\
& + \{\beta + \Delta\beta\}^T [\mathbf{G}^t] \{q^t + \Delta q^t\} - \int_{\Gamma_{cr}} \int_0^{\bar{\mathbf{u}} + \Delta\bar{\mathbf{u}} - \bar{\mathbf{u}} - \Delta\bar{\mathbf{u}}} T_i^{coh} d(u_i + \Delta u_i - u_i - \Delta u_i) d\Gamma_{cr}
\end{aligned} \tag{5.15}$$

where $[\mathbf{H}] = \int_{\Omega_e} [\mathbf{P}]^T [\mathbf{S}] [\mathbf{P}] d\Omega$, $[\mathbf{H}] = \int_{\Omega_e} [\mathbf{P}]^T [\mathbf{S}] [\mathbf{P}] d\Omega$, $[\mathbf{G}^e] = \int_{\partial\Omega_e} [\mathbf{P}]^T [\mathbf{n}^e] [\mathbf{L}_e] d\partial\Omega$,
 $[\mathbf{G}^e] = \int_{\partial\Omega_e} [\mathbf{P}]^T [\mathbf{n}^e] [\mathbf{L}_e] d\partial\Omega$, $[\mathbf{G}^m] = \int_{\Gamma_{cr}} [\mathbf{P}]^T [\mathbf{n}^{cr}] [\mathbf{L}^m] d\Gamma_{cr}$, $[\mathbf{G}^m] = \int_{\Gamma_{cr}} [\mathbf{P}]^T [\mathbf{n}^{cr}] [\mathbf{L}^m] d\Gamma_{cr}$,
 $[\mathbf{G}^t] = \int_{\Gamma_{int}} [\mathbf{P}]^T [\mathbf{n}^t] [\mathbf{L}^t] d\Gamma_{int}$, $[\mathbf{G}^t] = \int_{\Gamma_{int}} [\mathbf{P}]^T [\mathbf{n}^t] [\mathbf{L}^t] d\Gamma_{int}$, $[\bar{\mathbf{T}}] = \int_{\Gamma_m} [\mathbf{P}]^T [\mathbf{n}^e] [\mathbf{L}^e] d\Gamma_m$, and
 $[\bar{\mathbf{T}}] = \int_{\Gamma_m} [\mathbf{P}]^T [\mathbf{n}^e] [\mathbf{L}^e] d\Gamma_m$

From Eqn. 5.15, the weak form of the element kinematic relations is obtained as [18]

$$\begin{bmatrix} [\mathbf{H}] \\ [\mathbf{H}] \end{bmatrix} \begin{Bmatrix} \beta + \Delta\beta \\ \beta + \Delta\beta \end{Bmatrix}_e = \begin{bmatrix} [\mathbf{G}^e] & 0 & [\mathbf{G}^m] & 0 & [\mathbf{G}^t] \\ 0 & [\mathbf{G}^e] & 0 & -[\mathbf{G}^m] & -[\mathbf{G}^t] \end{bmatrix} \begin{Bmatrix} q^e + \Delta q^e \\ q^e + \Delta q^e \\ q^m + \Delta q^m \\ q^m + \Delta q^m \\ q^t + \Delta q^t \end{Bmatrix}_e \tag{5.16}$$

or in its condensed form

$$[\mathbf{H}]_e \{\beta + \Delta\beta\}_e = [\mathbf{G}]_e \{q\}_e \tag{5.17}$$

If the element $[\mathbf{H}]_e$ matrix is invertible then the stress coefficients can be directly expressed in terms of the nodal displacements, since the Eqn. 5.17 is linear. The weak forms of the global traction continuity conditions are subsequently solved by setting the variation of the total energy functional in Eqn. 5.2 with respect to the displacement degrees of freedom to zero. This results in the weak form of the traction reciprocity conditions as [18]:

$$\sum_{e=1}^N \begin{bmatrix} [\mathbf{G}^e] & 0 & [\mathbf{G}^m] & 0 & [\mathbf{G}^t] \\ 0 & [\mathbf{G}^e] & 0 & -[\mathbf{G}^m] & -[\mathbf{G}^t] \end{bmatrix}_e^T \begin{Bmatrix} \beta^1 + \Delta \beta^1 \\ \beta^2 + \Delta \beta^2 \end{Bmatrix}_e = \sum_{e=1}^N \begin{Bmatrix} \frac{1}{T} \\ \frac{2}{T} \\ \bar{f}_{coh} \\ -\bar{f}_{coh} \\ 0 \end{Bmatrix}_e \quad (5.18)$$

where $\bar{f}_{coh}^e = \frac{\partial}{\partial \Delta u} \int_{\Gamma_{cr}} [\phi(\mathbf{u} + \Delta \mathbf{u} - \mathbf{u} - \Delta \mathbf{u}) - \phi(0)] d\Gamma_{cr}$. In its condensed form Eqn. 5.18 becomes

$$\sum_{e=1}^N [\mathbf{G}]_e^T \{\boldsymbol{\beta} + \Delta \boldsymbol{\beta}\} = \sum_{e=1}^N \{\bar{\mathbf{T}}_{ext}\}_e \quad (5.19)$$

Combining Eqns. 5.17 and 5.19 and eliminating the stress degree of freedom, the following final equation is obtained:

$$\sum_{e=1}^N \{[\mathbf{G}]^T [\mathbf{H}]^{-1} [\mathbf{G}]\}_e \{\mathbf{q} + \Delta \mathbf{q}\} = \sum_{e=1}^N \{\bar{\mathbf{T}}_{ext}\}_e \quad (5.20)$$

Eqn. 5.20 is a nonlinear algebra equation system and a Newton-Raphson iteration solver is consequently invoked to solve for the nodal displacement increments on the element boundaries and crack interfaces. The linearized form of Eqn. 5.20 for the j -th iteration is

$$\left\{ \sum_{e=1}^N \frac{\partial \{\bar{\mathbf{T}}_{ext}\}_e}{\partial \{\mathbf{q}\}} - \sum_{e=1}^N \{[\mathbf{G}]^T [\mathbf{H}]^{-1} [\mathbf{G}]\}_e \right\}^j \{d\mathbf{q}\}^j = \left\{ \sum_{e=1}^N \{\bar{\mathbf{T}}_{ext}\}_e - \sum_{e=1}^N \{[\mathbf{G}]^T [\mathbf{H}]^{-1} [\mathbf{G}]\}_e \{\mathbf{q} + \Delta\mathbf{q}\}_e \right\}^j \quad (5.21)$$

or in its condensed form

$$[\mathbf{K}^g]^j \{d\mathbf{q}^g\}^j = \{\mathbf{R}_{ext}^g\} - \{\mathbf{R}_{int}^g\}^j \quad (5.22)$$

During cohesive crack growth, snap-back may occur. As shown schematically in Fig. 5.3, snap-back results in simultaneous drops in load and displacement. For processes controlled monotonically by deformation the BCD portion of the curve shown in Fig. 5.3 is ignored and the solution curve will show a discontinuity with a negative jump from point B to point D. The BCD portion can be followed by decreasing both load and deformation while the crack grows and opens. In general, a Newton-Raphson solver cannot catch the snap-back branch, since the loading processing is monotonically

controlled by external deformation or loading conditions. The arc-length solver has been proposed in [70-72] as a method of overcoming shortcomings of the Newton-Raphson solver by introducing an arc length as a replacement to the incremental load parameter, thus improving the convergence direction in the solution space. For implementing arc length method in the X-VCFEM formulation, Eqn. 5.22 is modified with the introduction of the unknown loading parameter γ as

$$[\mathbf{K}^g]^j \{d\mathbf{q}^g\}^j = (\gamma^j + d\gamma^j) \{\mathbf{R}_{ext}^g\} - \{\mathbf{R}_{int}^g\}^j \quad (5.23)$$

where both $d\gamma^j$ and $\{d\mathbf{q}^g\}^j$ are unknowns. To account for additional unknowns, a constraint on the total crack opening separation is chosen as the additional equation. The total crack opening separation is written as

$$\sum_{i \in Crk} (\mathbf{u}_i^2 + \Delta \mathbf{u}_i^2 - \mathbf{u}_i^1 - \Delta \mathbf{u}_i^1) = \Delta l^2 \quad (5.24)$$

where Crk represents the set of all nodes on crack surfaces. The constant Δl on the right hand side of Eqn. 5.24 is adjusted according to the current iteration step size. Although other constraint conditions may be chosen as the additional equation, a linear equation, such as that in Eqn. 5.24, effectively improves the convergence of the solver [65].

5.5 ASPECTS OF NUMERICAL IMPLEMENTATION OF X-VCFEM

5.5.1 STABILITY CONDITIONS

The stability of the XVCFEM solution algorithm is dependent on the following conditions:

- 1) The $[P]$ matrix must have linearly independent columns .
- 2) The $[H]$ matrix must be invertible .
- 3) The element boundary and crack must have the same rigid body modes.
- 4) The rigid body displacement field should not generate any stress. This is ensured

by satisfying the following condition :

$$n_{\beta} > n_q + n_{cr} - 3 \quad (5.25)$$

where $n_{\beta} > n_q + n_{cr} - 3$ are the number of stress parameters $\{\beta\}$, the number of displacement degrees of freedom on element boundary, and the number of degrees of freedom on crack face, respectively.

5.5.2 ADAPTIVE CRITERIA FOR COHESIVE CRACK GROWTH

A). Direction of incremental cohesive crack advance

To determine the direction of incremental crack advance, a criterion based on the cohesive energy at the crack tip is used in X-VCFEM. From the definition of the J integral, a relation between the cohesive energy ϕ for complete decohesion and the critical energy release rate G_c has been established as [47]:

$$G_c = J = \int_0^R T \frac{\partial \delta}{\partial x} dx = \int_0^{\delta_c} T d\delta = \phi \quad (5.26)$$

where R is the length of the cohesive zone. Consequently, the crack growth direction is estimated such that G_c or equivalently the cohesive energy ϕ is maximized for a given crack tip state of stress. The cohesive energy ϕ_A at the crack tip A along any direction α can be expressed for an arbitrary separation $\delta(\alpha)$ as:

$$\phi_A(\alpha) = \left(\int_0^{\delta} T(\alpha) d\delta \right)_A = \left(\int_{\sigma_{\max}}^t T(\alpha) \cdot \frac{\partial \delta}{\partial t} dt \right)_A \quad (5.27)$$

where $T(\alpha) = \sqrt{(T_n^{coh})^2 + \beta^{-2} (T_t^{coh})^2}$ is the magnitude of the effective cohesive traction.

The corresponding unit normal \mathbf{n} and tangential \mathbf{t} vectors along the direction α are expressed as:

$$\mathbf{n} = -\sin \alpha \mathbf{i} + \cos \alpha \mathbf{j} \quad , \quad \mathbf{t} = \cos \alpha \mathbf{i} + \sin \alpha \mathbf{j} \quad (5.28)$$

The normal and tangential components of the cohesive traction force at an angle α are then deduced as:

$$\begin{Bmatrix} T_n^{coh} \\ T_t^{coh} \end{Bmatrix} = \begin{bmatrix} n_x & n_y \\ t_x & t_y \end{bmatrix} \begin{Bmatrix} \sigma_{xx} n_x + \sigma_{xy} n_y \\ \sigma_{xy} n_x + \sigma_{yy} n_y \end{Bmatrix} = \begin{Bmatrix} \sigma_{xx} \sin^2 \alpha + \sigma_{xy} \sin 2\alpha + \sigma_{yy} \cos^2 \alpha \\ -\frac{1}{2} \sigma_{xx} \sin 2\alpha + \sigma_{xy} \cos 2\alpha + \frac{1}{2} \sigma_{yy} \sin 2\alpha \end{Bmatrix} \quad (5.29)$$

and hence the effective cohesive traction for direction α is:

$$T(\alpha) = \sqrt{\left(\sigma_{xx} \sin^2 \alpha - \sigma_{xy} \sin 2\alpha + \sigma_{yy} \cos^2 \alpha \right)^2 + \beta^{-2} \left(-\frac{1}{2} \sigma_{xx} \sin 2\alpha + \sigma_{xy} \cos 2\alpha + \frac{1}{2} \sigma_{yy} \sin 2\alpha \right)^2} \quad (5.30)$$

From simple calculus, extremum conditions for a $\phi_A(\alpha)$ are as follows:.

$$\frac{\partial \phi_A(\alpha)}{\partial \alpha} = 0 \quad \text{and} \quad \frac{\partial^2 \phi_A(\alpha)}{\partial \alpha^2} < 0 \quad (5.31)$$

Therefore the direction, α_c that maximizes $\phi_A(\alpha)$ is obtain by substituting Eqns. 5.27 and 5.30 into Eqn. 5.31, and the resulting direction of crack propagation α_c is reported as follows

$$\alpha_c = \begin{cases} \arctan \left(\frac{\sigma_{yy} - \sigma_{xx} \pm \sqrt{(\sigma_{xx} - \sigma_{yy})^2 + 4\sigma_{xy}^2}}{2\sigma_{xy}} \right) \\ \arctan \left(\frac{2(\beta^2 - 1)\sigma_{xy} \pm \sqrt{(4\beta^4 - 8\beta^2 + 4)\sigma_{xy}^2 - (4\beta^4 - 4\beta^2 + 2)\sigma_{xx}\sigma_{yy} - (2\beta^2 - 1)(\sigma_{xx}^2 + \sigma_{yy}^2)}}{2\beta^2\sigma_{xx} - \sigma_{xx} + \sigma_{yy}} \right) \end{cases} \quad (5.32)$$

B). Length of the incremental cohesive crack advance

Figure 5.4 shows various parameters associated with a cohesive crack in a Voronoi cell. The length of cohesive zone advance ($\Delta \bar{l}$) is estimated by postulating that the cohesive energy vanishes at the tip of the new crack segment shown in Fig. 5.4. To find where the cohesive energy vanishes, the cohesive energies at points A (present crack tip) and B (close to A in the direction of crack propagation) are evaluated by substituting the stresses into Eqn. 5.27. The tip of the cohesive zone is obtained from the linear extrapolation of this line to the point that yields zero cohesive energy. The increment of cohesive crack length is then defined as [18]:

$$\Delta \bar{l} = \frac{\phi_A}{\phi_A - \phi_B} |AB| \quad (5.33)$$

C). Cracks crossing the inter-element boundaries and merging with each other

A continuous tracking algorithm is implemented to monitor intersection of cohesive surface with element boundary. The intersection of the crack path and an element boundary is obtained by solving the equation system:

$$\frac{x-x_i}{x_{i+1}-x_i} = \frac{y-y_i}{y_{i+1}-y_i}, \quad \frac{x-x_n}{x_{n+1}-x_n} = \frac{y-y_n}{y_{n+1}-y_n} \quad (5.34)$$

where (x_i, y_i) represents the tip of the cohesive crack line for the i^{th} increment, and (x_n, y_n) is the position of the n^{th} node on the element boundary. If the intersection point is outside of the cohesive line or the element boundary, no intersection is assumed. Once a cohesive crack has intersected a boundary, a new node pair is introduced on the element boundary at this point. The crack is subsequently advanced to the next element.

It is possible for multiple cracks in proximity to merge or intersect with each other. The algorithm for crack merging is an extension of the boundary intersection algorithm, discussed above. To obtain the intersection of cracks merging together, (x_n, y_n) in Eqn. 5.34 is replaced with the position of the n^{th} node on the neighboring crack path.

5.5.3 ELIMINATION OF ELEMENT RIGID BODY MODES

Displacement fields on the element and crack boundaries in the X-VCFEM formulation are represented independently. The node-pairs at the crack face are not topologically connected to the element boundary nodes. It is important for all nodes in the element to possess the same rigid body modes. The prescribed displacement boundary conditions directly constrain the rigid body modes of the element boundary displacements $\{\mathbf{q}^e\}$. However, it is necessary to connect these with rigid-body modes for the crack face displacement fields $\{\mathbf{q}^{cr}\}$ and $\{\mathbf{q}^{cr}\}$. Singular value decomposition or SVD has been discussed in [73] as an effective method for identifying and constraining rigid body modes at interfaces inside the Voronoi cell elements. The matrix product may be expressed as

$$\begin{aligned} \left[\begin{array}{c} [\mathbf{G}^{cr}] \\ -[\mathbf{G}^{cr}] \end{array} \right] \left\{ \begin{array}{c} \mathbf{q}^{cr} \\ \mathbf{q}^{cr} \end{array} \right\} &= [\mathbf{U}][\lambda][\mathbf{V}] \left\{ \begin{array}{c} \mathbf{q}^{cr} \\ \mathbf{q}^{cr} \end{array} \right\} = [\mathbf{U}][\lambda] \left\{ \begin{array}{c} \hat{\mathbf{q}}^{cr} \\ \hat{\mathbf{q}}^{cr} \end{array} \right\} \\ &= \left[\begin{array}{c} [\hat{\mathbf{G}}^{cr}] \\ -[\hat{\mathbf{G}}^{cr}] \end{array} \right] \left\{ \begin{array}{c} \hat{\mathbf{q}}^{cr} \\ \hat{\mathbf{q}}^{cr} \end{array} \right\} \end{aligned} \quad (5.35)$$

where $[\mathbf{U}]$ and $[\mathbf{V}]$ are orthonormal matrices obtained by SVD of $\left[\begin{array}{c} [\mathbf{G}^{cr}] \\ -[\mathbf{G}^{cr}] \end{array} \right]$. $[\lambda]$ is

a rectangular matrix with non-negative diagonal values. The zero or singular values in $[\lambda]$

correspond to either trivial solutions or to rigid body modes of the displacement solution. For accurate displacements, elements in $\{\hat{\mathbf{q}}^{cr}\}$ corresponding to small or zero eigenvalues in $[\lambda]$ are eliminated.

5.5.4 CRACK UPDATE PROCEDURE

The crack propagation without a predefined crack path introduces additional challenges due to sudden changes in crack length. The high stresses in the vicinity of the crack tip are re-distributed as the crack tip advances. The crack length increases instantaneously with no change in total energy of the system. Numerical instabilities and errors may arise if the situation is not dealt with carefully. A revised equilibrating scheme is introduced for crack propagation. The details of this scheme are presented next.

Crack trajectory update requires the introduction of new nodes and cohesive elements. The wavelets associated with the crack tip are also reassigned to the new crack tip. The Gaussian Wavelet bases chosen in this study only provide a set of linearly independent basis function which have a compact support but do not form orthogonal bases. Due to this limitation, all of the $\{\beta\}$ coefficients related to the redistributed stress field must be re-evaluated by performing an intermediate equilibrating step on the updated geometry without any change in total potential energy. Total potential energy is

kept fixed by keeping the external loading and boundary conditions unchanged. To avoid any fictitious damage accumulation, the non-linearity due to irreversible cohesive elements is suppressed during this equilibrating step.

In view of the local influence of the wavelets and stress concentration at the crack tip, the equilibrating step is performed by constraining boundary nodes of each element. The solution procedure followed during this step remains unaltered with an additional constraint equation:

$$\{\Delta \mathbf{q}^e\} = 0 \quad (5.36)$$

This equilibrating step eliminates the artificially introduced imbalance caused by the change in topology of the structure. The stresses generated during this step become a reference state upon which further loading is applied.

5.6 NUMERICAL EXAMPLES USING X-VCFEM

The X-VCFEM method has already been rigorously tested by comparing computational results with experimental observations elsewhere [17, 18, 65, 66]. However, to demonstrate the importance and efficiency of the revised crack update procedure an elastic plate problem with traction free crack faces is selected. Except for

the irreversible nature of the cohesive law, the problem is perfectly elastic and could be solved analytically using linear elastic fracture mechanics (LEFM). This is a very useful test to check the validity of the crack update procedure as LEFM problems have a unique solution and the material properties do not depend on the any kind of history. Hence, the solution obtained by the incremental procedure for a given crack length should be the same as that obtained by reloading the same geometry from zero load.

Figure 5.5 shows a centre-cracked plate of width $2w=5\text{m}$ and length $2b=3\text{m}$ with a crack length of $2a=0.6\text{m}$. The plate is assumed to be under plane strain and is subjected to simple far field tensile stress of σ_0 . The material and cohesive parameters selected for the study are: $E = 36.5 \text{ GPa}$, Poisson's ratio $=0.1$, $\sigma_{\max} = 0.01 \text{ MPa}$. The plate is modeled with one X-VCFEM element. The crack face is represented with 7 node pairs and the element boundary consists of 22 segments.

As described earlier, Φ^{poly} , Φ^{branch} and Φ^{wvlr} are the stress functions employed in the X-VCFEM formulation. For the polynomial function, the order of interpolation is $p_n = 13$ and $q_n = 13$ for a total of 102 terms. For the branch function only one term is included with $s_n = 0$ and $t_n = 0$. The resolution of wavelet functions adaptively increases until

convergence. The initial values of the parameters for the lowest wavelet resolution ($m=k=1$) are: $n_n=3$, $l_n=2$, and $a_I=c_I=b_I=d_I=0.15$.

The model is analyzed using two different solution schemes with and without the equilibrating step. First, after every crack increment the updated geometry is subjected to loading starting from zero until the crack propagation criterion is satisfied and the new crack increment is obtained. This process of loading from zero is repeated until the model loses all load carrying capacity. The second method includes incremental loading while performing an elastic equilibrium step after each crack increment. During the equilibrating step, the load history is preserved and cohesive elements follow a perfectly elastic traction-separation law without any damage. All external loading remains stationary and, by introduction of new node pairs, stresses within the element can redistribute once the crack is extended. Subsequent to the equilibrating step, external loads are incremented using the arc-length solver. A σ_{22} stress contour plot in Fig. 5.6 shows the stress concentrations at the crack tips. Figure 5.7 shows excellent agreement between macroscopic stress-strain responses obtained using the reloading procedure and the incremental loading with crack update procedure.

The excellent agreement between the results obtained using either the reloading or incremental loading with crack update methods confirms the effectiveness of introducing an equilibrating step in the incremental procedure. At this point it must be noted that the reloading procedure works for linear elastic problems, the response changes drastically as the irreversible cohesive zone elements are introduced. Figure 5.8 shows the macroscopic stress-strain response for incremental loading with crack updates when irreversible cohesive elements are present.

To demonstrate crack merging capability of X-VCFEM, a plate with two off center inclined cracks is analyzed. Figure 5.9 shows the geometric details of the model and the crack trajectories when the plate is subjected to simple tensile loading. Plane strain is assumed, and the material and cohesive parameters selected for this study are $E=36.5$ GPa, Poisson's ratio=0.1, $\sigma_{\max}=0.01$ MPa. Both the crack trajectories intersect the element boundaries and the eventual trajectories indicate that the cracks propagated such as to facilitate merging. Figure 5.10 shows the corresponding macroscopic response of the model and a rapid decline in load carrying capacity of the cracked plate is noted

5.7 HOMOGENIZATION BASED CONTINUUM DAMAGE MECHANICS (HCDM) MODEL

Traditional continuum damage mechanics (CDM) models [74] introduce a fictitious stress $\tilde{\Sigma}_{ij}$ acting on an active resisting area \tilde{A} . The reduction in original resisting area A to \tilde{A} is due to material degradation associated with micro-cracks and stress concentration in the vicinity of cracks. The effective stress $\tilde{\Sigma}_{ij}$ can be related to the actual Cauchy stress Σ_{ij} [75] through a fourth order damage effect tensor M_{ijkl} as

$$\tilde{\Sigma}_{ij} = M_{ijkl}(\mathbf{D})\Sigma_{kl} \quad (5.37)$$

where M_{ijkl} is a function of a damage tensor $\mathbf{D} (= D_{ijkl}\mathbf{e}_i \otimes \mathbf{e}_j \otimes \mathbf{e}_k \otimes \mathbf{e}_l)$. The tensor \mathbf{D} can be a zeroth, second or fourth order based on the type of model selected. As discussed in [61, 76], the hypothesis of equivalent elastic energy is used to evaluate M_{ijkl} and to establish a relation between the damaged and undamaged stiffness as

$$W_C(\Sigma, \mathbf{D}) = \frac{1}{2}(E_{ijkl}(\mathbf{D}))^{-1}\Sigma_{ij}\Sigma_{kl} = W_C(\tilde{\Sigma}, \mathbf{0}) = \frac{1}{2}(E_{ijkl}^0)^{-1}\tilde{\Sigma}_{ij}\tilde{\Sigma}_{kl} \quad (5.38)$$

where $\boldsymbol{\Sigma} = \Sigma_{ij} \mathbf{e}_i \otimes \mathbf{e}_j$, E_{ijkl}^0 is the elastic stiffness tensor in the undamaged state and $E_{ijkl}(\mathbf{D})$ is the stiffness in a damaged state. From Eqns. 5.37 and 5.38, the relation between the damaged and undamaged stiffness is established as[16]

$$E_{ijkl} = \left(M_{pqij} \right)^{-1} E_{pqrs}^0 \left(M_{rskl} \right)^{-T} \quad (5.39)$$

where the exponent $(-T)$ corresponds to the transpose of the inverse of the fourth order tensor \mathbf{M} . An appropriate choice of the order of the damage tensor and the assumption of a function for M_{ijkl} enables formulation of a damage evolution model using micromechanics and homogenization. An anisotropic CDM model proposed in [61] introduces a damage evolution surface to delineate the interface between damaged and undamaged domains in the strain space (e_{ij}) as

$$F = \frac{1}{2} P_{ijkl} \mathbf{e}_i \mathbf{e}_j \mathbf{e}_k \mathbf{e}_l - \kappa(\alpha W_d) = 0 \quad (5.40)$$

where W_d is the dissipation of the strain energy density due to stiffness degradation that is expressed as:

$$W_d = \int \frac{1}{2} P_{ijkl} \mathbf{e}_i \mathbf{e}_j \mathbf{e}_k \mathbf{e}_l dE_{ijkl} \quad (5.41)$$

An associative rule is assumed in the stiffness space which results in the evolution of the fourth order secant stiffness as:

$$\dot{E}_{ijkl} = \lambda \frac{\partial F}{\partial \left(\frac{1}{2} e_{ij} e_{kl} \right)} = \lambda P_{ijkl} \quad (5.42)$$

where P_{ijkl} is a fourth order symmetric negative definite tensor that corresponds to the direction of the rate of stiffness degradation tensor \dot{E}_{ijkl} , α is the scaling parameter and $\kappa(\alpha W_d)$ is the damage state variable. Calibration of the CDM model requires evaluation of κ , α and P_{ijkl} .

5.7.1 DAMAGE STATE VARIABLE

In the HCDM model the damage state variable $\kappa(\alpha W_d)$ is evaluated for a reference loading path, and results for all other strain paths are scaled with respect to this reference value. For the reference loading path ($e_{11} \neq 0$, all other $e_{ij} = 0$), setting $P_{1111} = 1$, κ is determined from damage surface of Eqn. 5.40 as

$$\kappa = \frac{1}{2} (e_{11})^2 \quad (5.43)$$

A functional representation of κ with W_d is established based on the micromechanical analysis and κ is determined by evaluating W_d at each strain increment.

5.7.2 PRINCIPAL DAMAGE COORDINATE SYSTEM (PDCS)

The damage effect tensor M_{ijkl} in Eqn. 5.37 has been derived in [77] for a second order damage tensor D_{ij} as

$$M_{ijkl} = (\delta_{ik} - D_{ik})^{-1} \delta_{jl} \quad (5.44)$$

D_{ij} is symmetric and it can describe the damage states which have at least orthotropic symmetry. Arbitrary D_{ij} may result in unsymmetric effective stress tensor. The stress tensor may be rendered symmetric with an implicit method suggested in [78], which is used to derive the inverse of the damage effect tensor $[\mathbf{M}(D_{ij})]^{-1}$. The HCDM model under consideration assumes orthotropy of the homogenized stiffness matrix in the principal damage coordinate system [16]. Provided the values of E_{ijkl}^0 and E_{ijkl} are known, Eqn. 5.44 results in a system of non-linear algebraic equations in D_{ij} . These equations are solved using a non-linear least squares minimization. Subsequently, the eigenvectors $(\mathbf{e}_{D1}, \mathbf{e}_{D2}, \mathbf{e}_{D3})$ of D_{ij} are evaluated and the transformation matrix $[\mathbf{Q}]^D = [\mathbf{e}_{D1} \ \mathbf{e}_{D2}$

$\mathbf{e}_{D3}]^T$ is formed. The rotation matrix $[\mathbf{Q}]^D$ transforms the global coordinate system to the principal damage coordinate system.

5.7.3 MICROMECHANICAL RVE MODEL WITH COHESIVE ZONE ELEMENTS

The first step towards implementing an HCDM model is identification of a representative volume element (RVE). Subsequent micromechanical analysis of the RVE is necessary for the development of the HCDM model. The damage evolution may be significantly influenced by the choice of RVE. The HCDM model is valid as long as an RVE exists, *i.e.* the damage is diffused and no localization or dominant crack path is established. The X-VCFEM model can be employed to perform the micromechanical analysis of top coat RVEs. Micromechanical damage in the RVE is explicitly incorporated as discrete cracks surrounded by fracture process zones that are simulated with extrinsic cohesive zone elements.

Cohesive zone models, introduced in [79, 80] and developed in [46-48, 51, 60, 81-83], are effective in depicting material failure as a separation process across an extended crack tip or fracture process zone. In these models, the tractions across the crack reach a maximum, subsequently decrease and eventually vanish with increasing separation across the crack. The cohesive model used in this chapter is a three parameter rate independent

linear cohesive model, proposed in [46, 47]. This is an extrinsic (two stage) model which has an infinite stiffness or slope in the rising portion of the traction-separation law up to a peak traction value. The rising portion of the traction-separation law is followed by a linearly descending segment until zero traction value is reached. The model assumes a free cohesive energy potential ϕ such that the traction across the cohesive surface is expressed as:

$$\mathbf{t}^{coh} = \frac{\partial \phi}{\partial \delta_n} \mathbf{n} + \frac{\partial \phi}{\partial \delta_t} \mathbf{t} \quad (5.45)$$

where δ_n and δ_t correspond to the normal and tangential components of the opening displacements over the cohesive surface in the \mathbf{n} and \mathbf{t} directions respectively. An effective opening displacement is defined as

$$\delta = \sqrt{\beta^2 \delta_t^2 + \delta_n^2} \quad (5.46)$$

where β is a coupling coefficient to allow assignment of different weights to normal and tangential opening displacements. Consequently the cohesive surface traction reduces to

$$\mathbf{t}^{coh} = \frac{t}{\delta} (\beta^2 \delta_t \mathbf{t} + \delta_n \mathbf{n}) \quad \text{where} \quad t = \frac{\partial \phi}{\partial \delta} = \sqrt{(\mathbf{t}_n^{coh})^2 + \beta^2 (\mathbf{t}_t^{coh})^2} \quad (5.47)$$

where t_n^{coh} and t_t^{coh} are the normal and tangential components of surface tractions, respectively. The effective cohesive force t in this model for increasing δ takes the form

$$t = \begin{cases} \frac{\sigma_{\max} (\delta_e - \delta)}{\delta_e} & \forall \delta < \delta_e \\ 0 & \forall \delta \geq \delta_e \end{cases} \quad (5.48)$$

δ_e corresponds to the separation at which t goes to zero and σ_{\max} is the peak value of t .

The effective normal traction-separation response of this model is depicted in Fig. 5.11.

As shown by the line BO in Fig. 5.11, in the softening region going from A to B or C,

unloading from any point on the traction-separation curve, proceeds along a linear path

from the current position to the origin.. The corresponding traction separation relation is

$$t = \frac{\sigma_{\max}}{\delta_e} \frac{\delta_e - \delta_{\max}}{\delta_{\max}} \delta \quad \forall \delta \leq \delta_{\max} \leq \delta_e \quad (5.49)$$

Reloading follows a linear path OBC with a reduced stiffness in comparison with the original stiffness. Traction vanishes for $\delta \geq \delta_e$. For negative normal displacement (compression), stiff penalty springs with high stiffness are introduced between the node pairs on the crack face.

5.7.4 HOMOGENIZATION AND STIFFNESS EVALUATION

Components of the homogenized elastic stiffness tensor E_{ijkl} , are calculated by solving six independent micromechanical boundary value problems (BVP) with the RVE. For each BVP the RVE is subjected to periodicity displacement conditions on the boundary. These conditions are enforced by constraining nodes on opposite faces of the RVE boundary to deform in a periodic manner. A given macroscopic or average strain e_{ij} is applied on the RVE by decomposing the displacement on the boundary into a macroscopic averaged part and a periodic part [84, 85]. The relationship between e_{ij} and the displacements is as follows:

$$u_i = e_{ij}x_j + \tilde{u}_i \quad (5.50)$$

Since the periodic part \tilde{u}_i is equal on corresponding nodes of opposite faces of the RVE (say n_1^p and n_2^p), the total displacement at these nodes are related as

$$(u_i)_{n_2^p} - (u_i)_{n_1^p} = e_{ij}\Delta x_j \quad (5.51)$$

where Δx_j are the relative coordinates of nodes on opposite faces.

For evaluating the homogenized elastic stiffness tensor E_{ijkl} , periodic BVPs of the RVE are solved by applying only a single unit strain component. The homogenized or macroscopic stresses σ_{ij} are obtained by volume averaging using the following equation:

$$\Sigma_{ij} = \frac{1}{Y} \int_Y \sigma_{ij}(Y) dY \quad (5.52)$$

The homogenized strains are evaluated by volume averaging the micromechanical solutions with the following equation:

$$e_{ij} = \frac{1}{Y} \int_Y \varepsilon_{ij}(Y) dY + \frac{1}{2Y} \int_{\partial Y_{\text{int}}} ([u_i] n_j + [u_j] n_i) dS \quad (5.53)$$

For Eqns. 5.52 and 5.53, σ_{ij} and ε_{ij} are RVE-based microscopic stresses and strains, respectively, and Y is the RVE domain. Y_{int} corresponds to the crack faces domain and $[u_i]$ denotes the jump in displacement components across the crack faces with outward normal n_i .

5.8 EVOLUTION EQUATIONS FOR THE HOMOGENIZATION BASED MODEL IN PDCS

The damage evolution surface of Eqn. 5.40 is rewritten in the PDCS as

$$F' = \frac{1}{2} e'_{ij} P'_{ijkl} e'_{kl} - \kappa'(W_d) = 0 \quad (5.54)$$

where the prime in the superscript denotes quantities expressed in the PDCS using the following transformation laws

$$E'_{ijkl} = Q_{ip} Q_{jq} Q_{kr} Q_{ls} E_{pqrs} \quad \text{and} \quad e'_{ij} = Q_{ip} Q_{jq} e_{kl} \quad (5.55)$$

where Q_{ij} is the transformation matrix. The corresponding rate of stiffness degradation in the PDCS is

$$\dot{E}'_{ijkl} = \dot{\lambda} \frac{\partial F'}{\partial \left(\frac{1}{2} e'_{ij} e'_{kl} \right)} = \dot{\lambda} P'_{ijkl} \quad (5.56)$$

5.9 SENSITIVITY ANALYSIS OF VALIDITY OF HCDM FOR TOP COAT DAMAGE

The HCDM model can be employed for evaluating damage evolution in the top coat of TBCs. Unlike with composite materials for which HCDM model has been developed, the top coat damage may result in complete loss of stiffness. Complete loss of stiffness may result in material instability and render the HCDM model invalid.

Before the HCDM model can be applied to the top coat a sensitivity analysis is performed to determine conditions and restrictions on the use of the HCDM model. The simple RVE shown in Fig. 5.12 is selected for a sensitivity analysis. Micro-mechanical analyses required for the HCDM model are performed for this RVE. All geometric and material parameters remain stationary while the cohesive elements parameter (δ_e) is varied to represent variation in fracture energy of the top coat. The material parameters for the RVE are $E=200$ GPa, Poisson's ratio=0.3 and $\sigma_{max}=287$ MPa. The fracture energy of the top coat is assumed to vary from 0.25-3.5 J/m² and the corresponding values of δ_e are evaluated by equating cohesive energy $\left(\phi = \frac{1}{2} \sigma_{max} \delta_e \right)$ to the fracture energy.

Fig. 5.12 shows the crack trajectory when the RVE is subjected to unit normal strain along the horizontal axis. Figure 5.13a shows the macroscopic response of this RVE for different values of δ_e , varying from 5.E-3 to 5.E-2. The macroscopic stress and strain are

evaluated using Eqns. 5.52 and 5.53, respectively. The snap-back instability experienced by the RVE is captured by the arc length algorithm employed in the X-VCFEM formulation. As seen in Fig. 5.13a, larger values of cohesive parameter δ_e (*i.e.*, higher cohesive energy) result in larger macroscopic strain accumulation prior to snap-back instability in the RVE. The onset of snap-back indicates that the material has become unstable. In such situations, the HCDM model will not be applicable. Appearance of snap-back instability implies limits for the validity for HCDM based on physical response of the micromechanical model.

Figure 5.13b shows the corresponding evolution of damage state variable (κ') with increasing damage work (W_d). For all parametric variation of δ_e considered, it can be observed that the κ' reaches a peak value before decreasing with increasing W_d . A decrease in κ' implies loss of material stability rendering the HCDM model invalid. Hence, for any selected value of cohesive energy there exists a unique critical peak value of damage function (κ'_c) beyond which the HCDM model becomes invalid. It should be noted that κ'_c corresponds to the onset of snap-back instability in macroscopic response of RVE. Hence, a criterion for the validity of the HCDM can be established as:

$$\kappa'(W_d) \leq \kappa'_c(\phi) \quad (5.57)$$

where ϕ is the cohesive energy.

The relationship between κ'_c and cohesive energy ϕ is graphically shown in Fig. 5.14. It reveals that κ'_c increases rapidly with increasing cohesive energy before stabilizing. The relationship between κ'_c and ϕ identifies the limit of validity of the HCDM for microstructure with dispersed cracks.

Figure 5.15 shows representative RVE results for the E_{2222} stiffness degradation for increasing values of δ_c . The monotonic degradation in stiffness confirms that the HCDM model can be readily calibrated using the micromechanical response of the RVE. Provided κ' does not exceed the critical value the HCDM can subsequently be implemented for a macro scale analysis of top coat damage.

5.10 CONCLUSIONS

In this chapter a framework to investigate damage evolution in top coat employing assumed stress hybrid extended Voronoi cell finite element (X-VCFEM) and homogenization based continuum damage mechanics (HCDM) model is presented. It is demonstrated that X-VCFEM can simulate micro-mechanical response of a top coat RVE containing a crack. The results show that the RVE experiences snap back instability after accumulating significant damage. Such instability is readily handled by X-VCFEM, however it renders the HCDM model invalid due to material instability. Thus, a sensitivity analysis is performed to identify a criterion to determine validity of HCDM model. It is found that there exists a critical value of damage state variable (κ'_c) beyond which material becomes unstable. The study also establishes a relationship between κ'_c and the fracture energy of top coat. The top coat is designed to be strain tolerant and it is not trivial to determine its fracture energy accurately. Using the validity criterion given in Eqn. 5.57, the HCDM model can be calibrated for any value of top coat fracture energy.

The framework proposed here is very appealing as it eliminates the computational cost involved in performing elaborate micro-mechanical analysis with numerous defects and yet incorporates their effects at the macro scale. However, identifying an accurate

RVE and determining the cohesive parameters is non trivial. In addition, the failure predictions would be conservative since only the onset of material instability can be predicted and actual failure cannot be predicted. Despite these limitations the proposed framework is a significant contribution towards TBC failure modeling. With additional experimental data this framework could be employed to determine effects of top coat microstructure on TBC failure. It can also be used to establish top coat microstructure design recommendations.

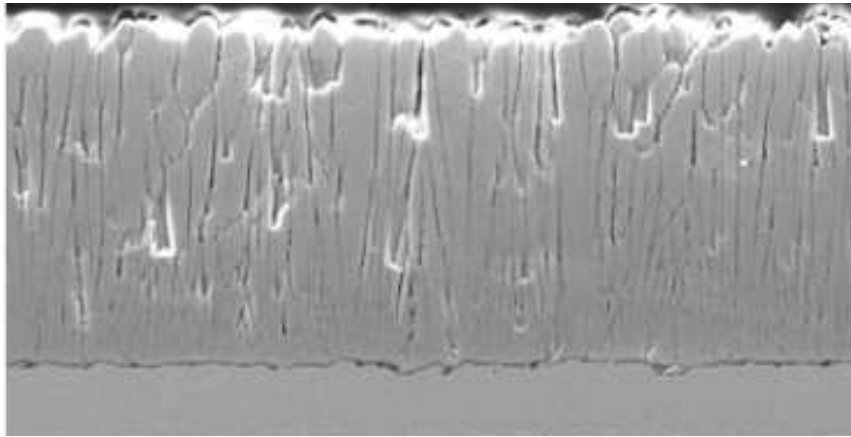
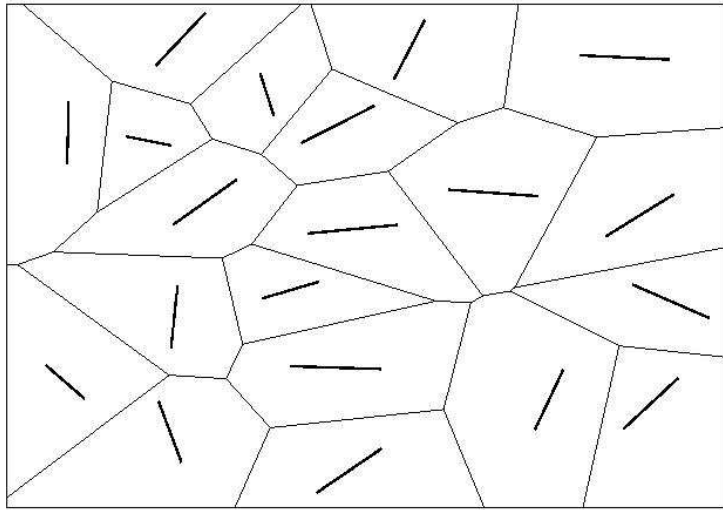
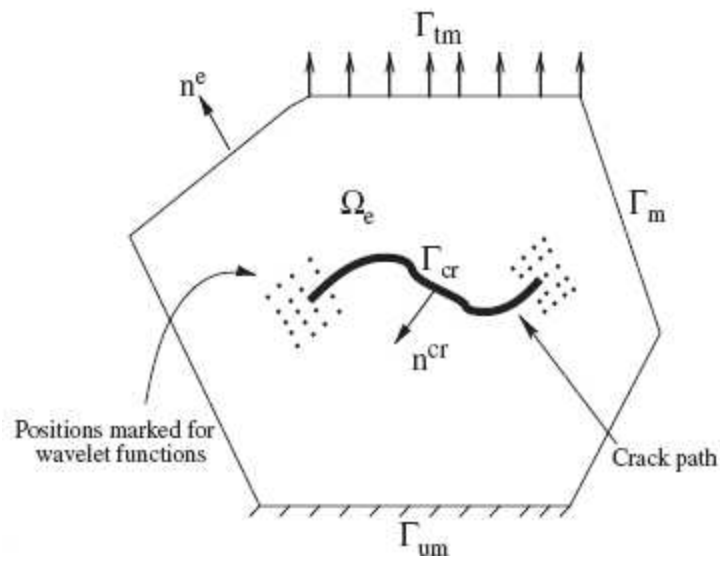


Figure 5.1: A SEM image of the TBC microstructure [20] showing the diffused nature of micro cracks in the top coat.



(a)



(b)

Figure 5.2: (a) A mesh of Voronoi cell elements generated by tessellation of the heterogeneous microstructural domain. (b) A typical Voronoi cell element enriched by wavelet functions.

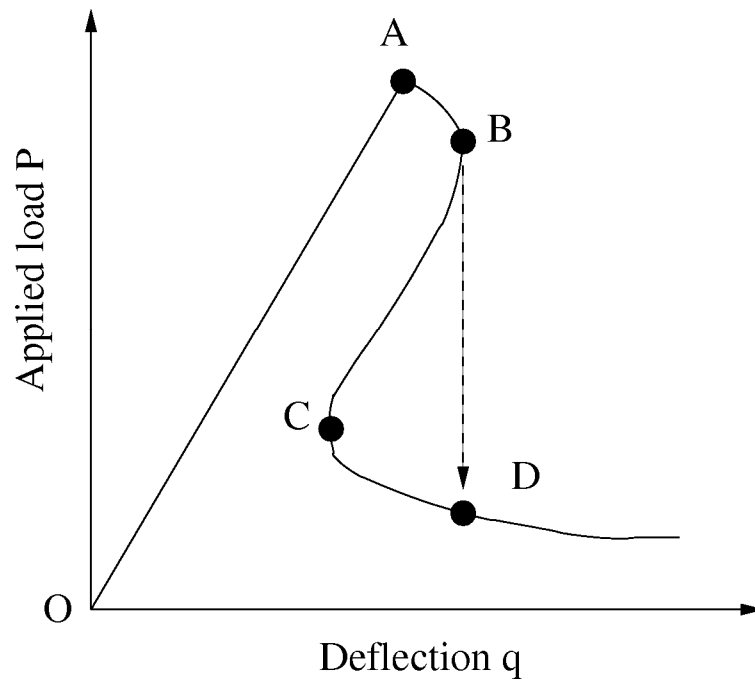


Figure 5.3: Schematic of a snap-back response with crack propagation.

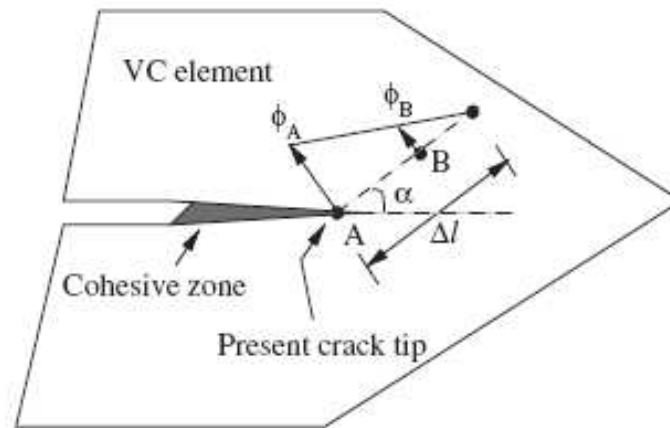


Figure 5.4 Schematic showing parameters associated with crack propagation within a Voronoi cell.

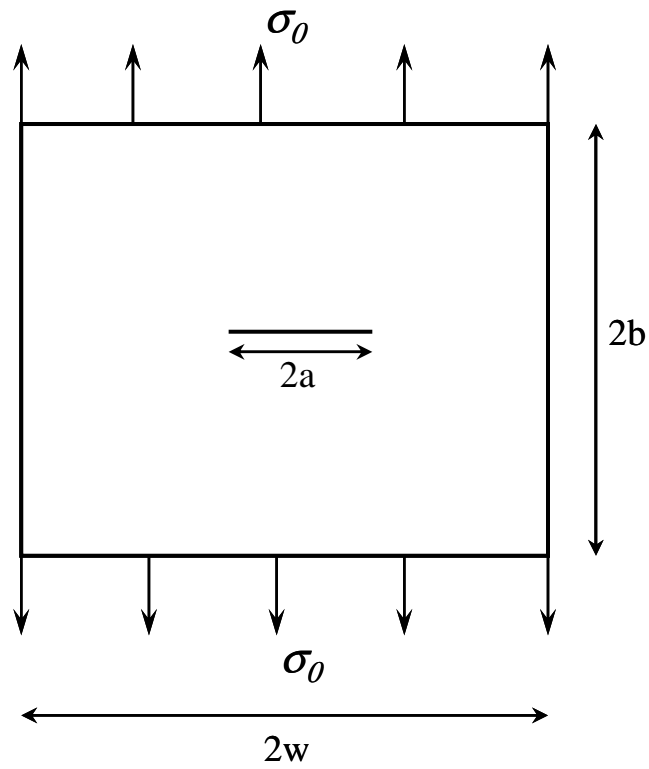


Figure 5.5 Schematic of a center cracked plate geometry subjected to uniaxial tension σ_0 .

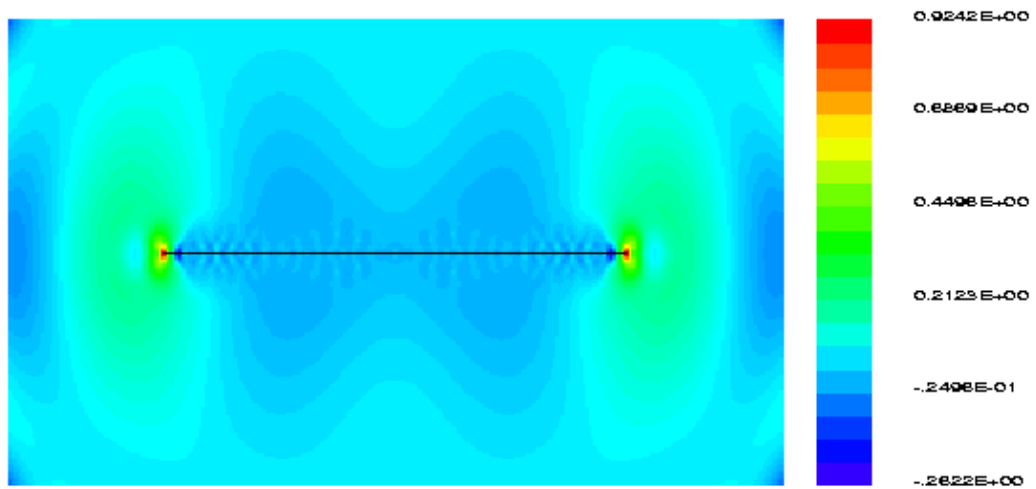


Figure 5.6 A σ_{22} normal stress contour plot of center cracked plate subjected to uniaxial tension after significant crack propagation.

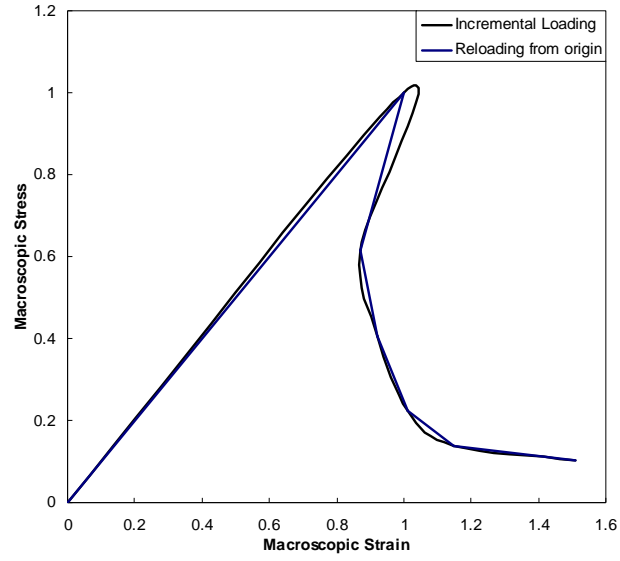


Figure 5.7: A comparison of the macroscopic stress-strain response of an elastic center cracked plate using complete reloading and incremental loading with crack update. The stress and strain are normalized $\sigma^{\max}=147$ MPa and $\epsilon^{\max}=1.E-5$.

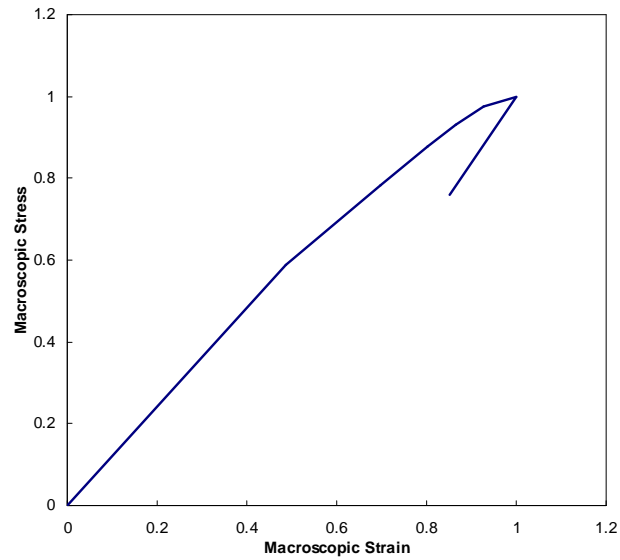


Figure 5.8: The mechanical response of a center cracked plate with irreversible cohesive elements using incremental loading with crack updates. The stress and strain are normalized with $\sigma^{\max}=186$ MPa and $\epsilon^{\max}=3.E-5$

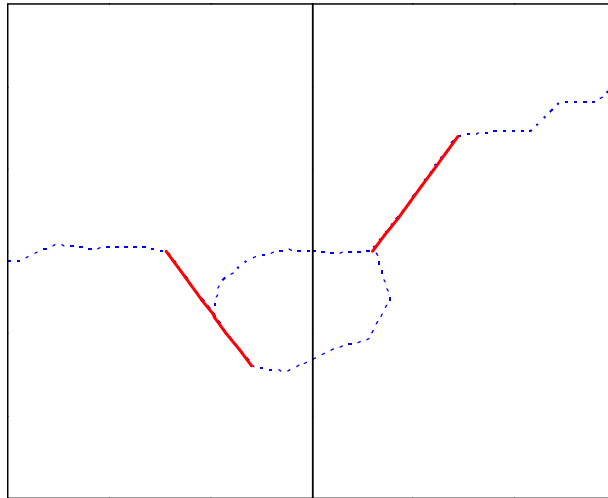


Figure 5.9: A schematic showing a plate with two inclined cracks contained in two Voronoi cells and subjected to uniaxial tensile load along vertical direction. The initial crack geometry is depicted with the solid line and the subsequent trajectory is illustrated with dashed lines.

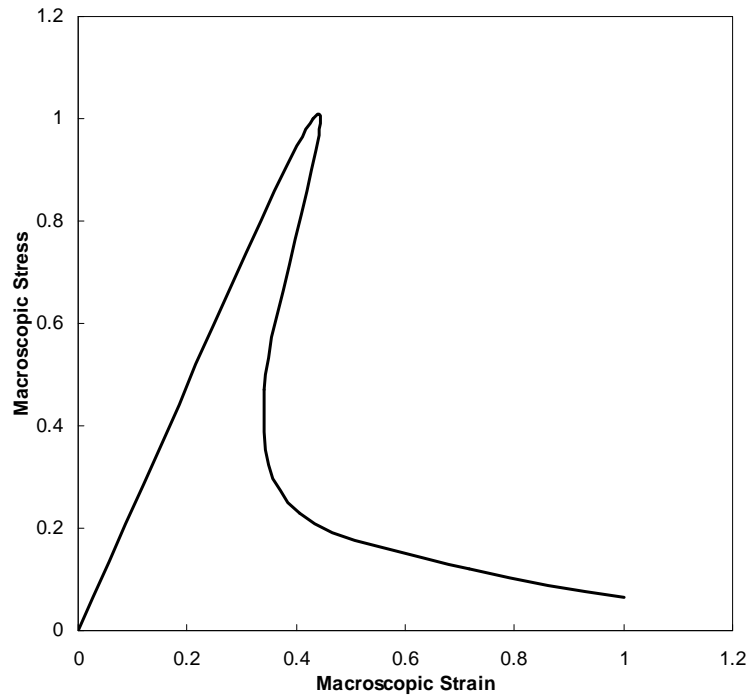


Figure 5.10: The macroscopic response from uniaxial loading of the plate with two inclined cracks shown in Fig. 5.9

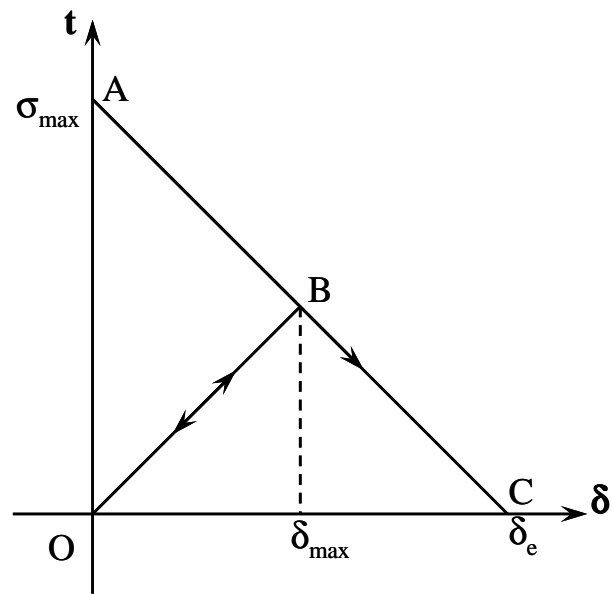


Figure 5.11 Rate independent irreversible traction separation cohesive law

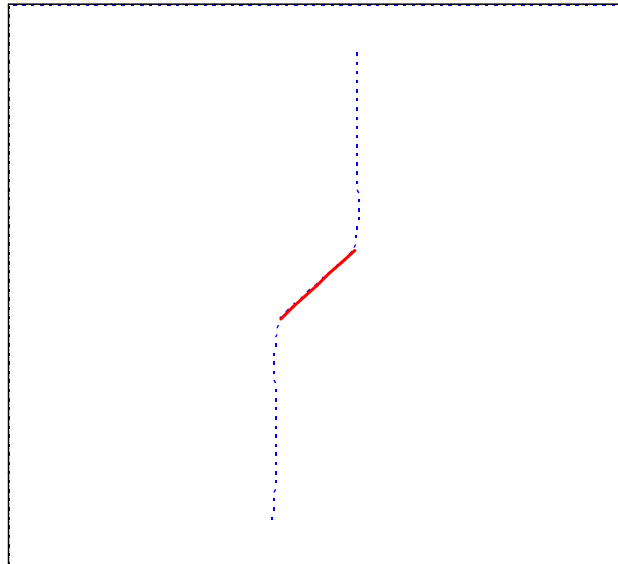
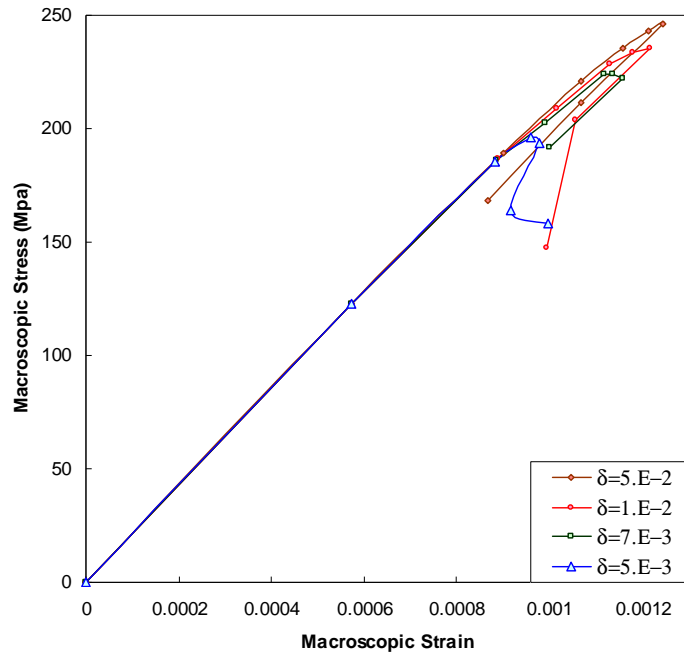
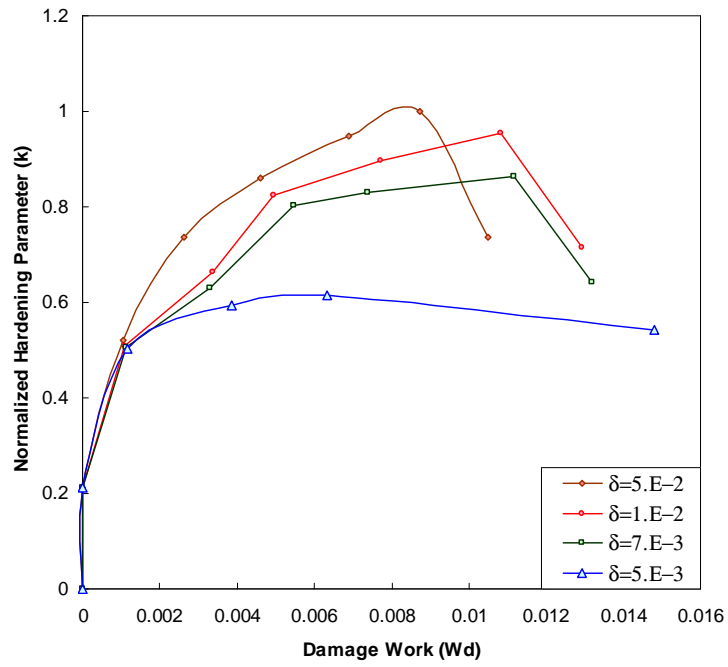


Figure 5.12: An RVE schematic showing the crack trajectory with an inclined crack subjected to unit tensile strain along horizontal axis. The initial crack geometry is depicted with solid line and the subsequent trajectory is illustrated with dashed line.



(a)



(b)

Figure 5.13 a) the macroscopic response of the RVE, and b) the relationship between damage state variable (κ) and damage work for increasing values of δ_e

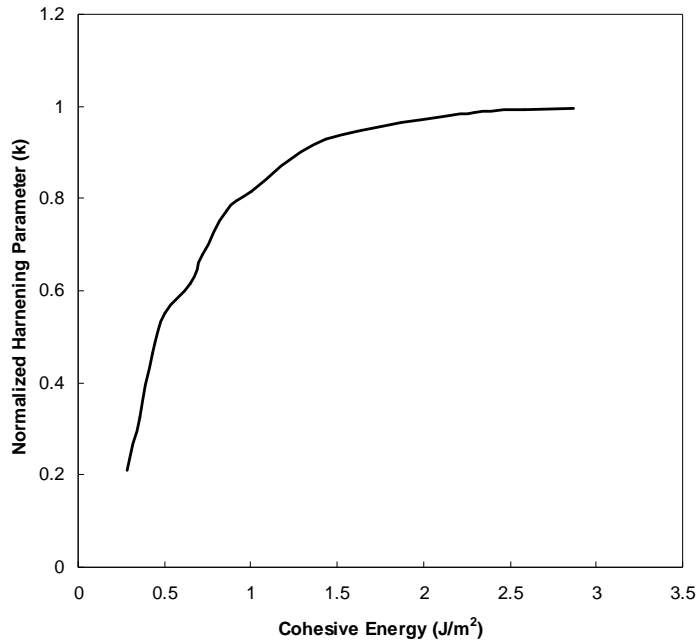


Figure 5.14: A plot showing the relationship between the critical value of damage state variable (κ_c) and cohesive energy associated with the cohesive zone elements.

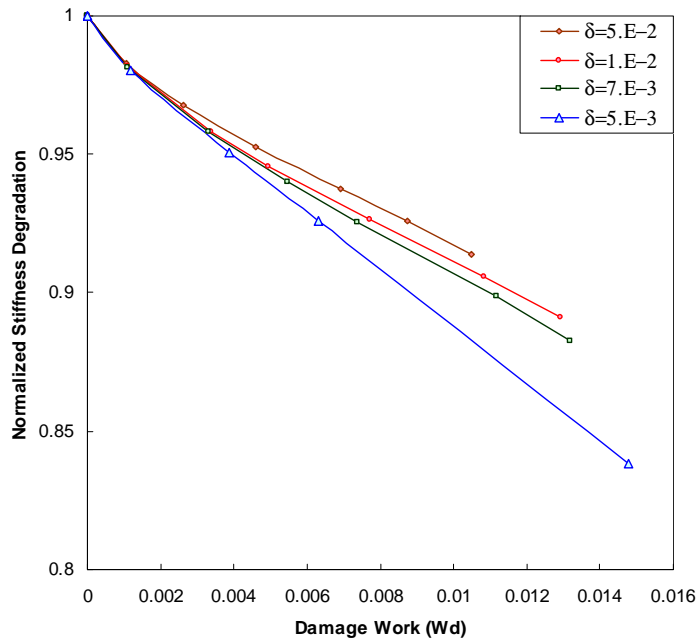


Figure 5.15: A plot showing the degradation of the secant stiffness E_{2222} of the top coat RVE for increasing damage work.

CHAPTER 6

CONCLUSIONS AND FUTURE STUDIES

In this dissertation, various failure mechanisms responsible for catastrophic failure of TBCs due to delaminations along susceptible interfaces of constituent layers are investigated using finite element models. Failure scenarios have been established by experimental observations found in the open literature. In the context of linear elastic TBCs, failure is preceded by a competition between buckling instability and delamination extension. On the other hand, TBCs experiencing significant bond coat creep incur top coat cracks that propagate to the interface and cause delamination. With an emphasis on determining critical geometric and material parameters, two separate finite element models are developed to characterize the experimentally observed failure scenarios.

The first investigation is aimed at using a finite element model to characterize competing interfacial delamination failure modes (*e.g.* buckling instability and strain energy driven interfacial crack propagation) in linear elastic thermal barrier coatings. The

solution of a linear elastic eigen-value problem determines the onset of the buckling instability with a pre-existing delamination between the bond coat and the TGO. The virtual crack extension method is employed to study strain energy release rate driven interfacial delamination at wavy interfaces. The materials and geometries in the study are chosen to be representative of TBC materials in real applications. Extensive sensitivity analyses are conducted to identify the critical design parameters affecting the onset of buckling and extension of interfacial delamination, as well as to develop parametric relations that enhance the understanding of these mechanisms. These novel parametric relations with extended range of application are validated with existing relations in the literature. In addition, the parametric formalism of the competing failure mechanisms for a 3-layer coating system is the first of its kind.

This first investigation concludes with a study of the competing mechanisms as the delamination extends over an undulation. It is demonstrated that the buckling instability is the leading failure mechanism at flat interfaces and at the locations of minimum cross-section in a wavy interface. However, in the vicinity of waviness, crack extension can become a dominant mode of failure. The probability of a particular mechanism taking precedence over the other depends on various geometric and material parameters and the

nature of the loading. A comparative study of the predicted critical buckling stress with critical delamination stress can identify the dominant mechanism. Although this study illustrates the competition between the failure mechanisms in detail, the validity is limited to the linear elastic TBCs.

The second investigation focuses on top coat crack initiation and propagation using a thermo-elastic finite element model with bond coat creep. Cracking is assumed to initiate when the maximum principal stress exceeds the rupture stress of the top coat. The contribution of geometric parameters to crack initiation is estimated, and a multi-dimensional parametric space is represented as a reduced-order 2-D parametric domain map for crack initiation in terms of the relevant parameters. The reduced-order domain map is constructed by collecting the critical parameters into 2 unique variables that span the 2-D domain. This domain classifies the design space as “fail”, “safe,” and “sub-safe” for crack initiation. An extended sensitivity analysis estimates the contribution of geometric and material parameters and forms a basis to derive a parametric relation to estimate maximum principal stress. The derived relation delineates the parametric combinations that are susceptible to damage.

Subsequent to the construction of domain map crack propagation simulations using a hysteretic cohesive zone model are performed for parametric combinations which initiate cracks away from the interface. These analyses conclude that parametric combinations that initiate top coat cracks also assist in propagation and eventual delamination of the TGO and top coat interface. The materials and geometries in the study are chosen to be representative of TBC materials in real applications.

This investigation of crack initiation and propagation concludes with a finite element simulation of a representative failure scenario seen in the literature. The geometry is obtained from an SEM image and the simulation is conducted with nominal material properties from the literature. The crack trajectory predicted by simulations is found to be in excellent agreement with crack trajectory observed in the SEM image. Although the present study characterizes the top coat damage evolution and propagation in detail, the validity is limited to damage initiating in an idealized, defect free isotropic top coat.

The final part of this dissertation proposes a modeling framework to incorporate the effects of top coat microstructure on TBC failure. The framework involves simulation of multiple propagating cohesive cracks in the top coat microstructure using an assumed stress hybrid element method. The results of these micro-mechanical simulations can be

used to calibrate a homogenization based continuum damage mechanics (HCDM) model to incorporate the effects of top coat microstructural flaws.. A sensitivity study provides the range of validity for the HCDM model.

The research presented in this dissertation has rigorously investigated the failure mechanisms and the parameters critical for failure of TBCs. Reduced-order models for buckling instability and delamination are developed for elastic defect free TBCs. Parametric models and relations are developed for delineating safe design regimes for TBCs demonstrating failure due to creep under cyclic thermal loading. These models can be easily incorporated into TBC design practices, especially with respect to structural integrity. However, these models are limited by the assumption that the TBC microstructure is initially defect free. The proposed HCDM frame work can be easily implemented in conjunction with experimental studies to identify representative volume elements for top coat, calibrate the model, and predict failure due to defects in top coat microstructure.

There are several TBC failure mechanisms that have not been addressed in this dissertation. Among the most actively researched mechanisms are those induced by calcium-magnesium-alumino-silicate (CMAS) [86] deposition on the exposed surfaces of

top coat and foreign object damage (FOD) [87]. In addition to the stresses due to thermal loads, several other damage inducing loads have been proposed. Primary among these are bond coat martensitic transformation strain [88] and TGO growth strains [12]. The finite element (FE) models presented in this dissertation can be easily enhanced to include loads resulting from transformation or growth strains as well as to address other failure mechanisms resulting from CMAS or FOD. The parametric nature of the FE models will enable identification of critical parameters for any selected failure mechanism.

BIBLIOGRAPHY

- [1] Wright PK, Evans AG. Mechanisms governing the performance of thermal barrier coatings. *Current Opinions in Solid State & Material Science* 1999;4:255.
- [2] Tolpygo VK, Clarke DR, Murphy KS. Oxidation-induced failure of EB-PVD thermal barrier coatings. *Surface & Coatings Technology* 2001;146:124.
- [3] Tolpygo VK, Clarke DR, Murphy KS. Evaluation of interface degradation during cyclic oxidation of EB-PVD thermal barrier coatings and correlation with TGO luminescence. *Surface & Coatings Technology* 2004;188-89:62.
- [4] Spitsberg IT, Mumm DR, Evans AG. On the failure mechanisms of thermal barrier coatings with diffusion aluminide bond coatings. *Materials Science and Engineering a-Structural Materials Properties Microstructure and Processing* 2005;394:176.
- [5] Vaidyanathan K, Gell M, Jordan E. Mechanisms of spallation of electron beam physical vapor deposited thermal barrier coatings with and without platinum aluminide bond coat ridges. *Surface & Coatings Technology* 2000;133-134:28.
- [6] Bhatnagar H, Ghosh S, Walter ME. Parametric studies of failure mechanisms in elastic EB-PVD thermal barrier coatings using FEM. *International Journal of Solids and Structures* 2005.
- [7] Evans AG, He MY, Hutchinson JW. Mechanics-based scaling laws for the durability of thermal barrier coatings. *Progress in Material Science* 2001;46:249.
- [8] Evans AG, Hutchinson JW, He MY. Micromechanics model for the detachment of residually compressed brittle films and coatings. *Acta Materialia* 1999;47:1513.

- [9] He MY, Evans AG, Hutchinson JW. Effects of morphology on the decohesion of compressed thin films. *Materials Science and Engineering a-Structural Materials Properties Microstructure and Processing* 1998;245:168.
- [10] Hutchinson JW, Suo Z. Mixed mode cracking in layered materials. *Advances in Applied Mechanics* 1992;29:148.
- [11] Evans AG, He MY, Hutchinson JW. Effect of interface undulations on the thermal fatigue of thin films and scales on metal substrates. *Acta Materialia* 1997;45:3543.
- [12] Karlsson AM, Hutchinson JW, Evans AG. The displacement of the thermally grown oxide in thermal barrier systems upon temperature cycling. *Materials Science and Engineering a-Structural Materials Properties Microstructure and Processing* 2003;351:244.
- [13] Karlsson AM, Xu T, Evans AG. The effect of the thermal barrier coating on the displacement instability in thermal barrier systems. *Acta Materialia* 2002;50:1211.
- [14] Xu T, He MY, Evans AG. A numerical assessment of the durability of thermal barrier systems that fail by ratcheting of the thermally grown oxide. *Acta Materialia* 2003;51:3807.
- [15] He MY, Mumm DR, Evans AG. Criteria for the delamination of thermal barrier coatings: with application to thermal gradients. *Surface & Coatings Technology* 2004;185:184.
- [16] Jain JR, Ghosh S. Homogenization based 3D continuum damage mechanics model for composites undergoing microstructural debonding. *International Journal of Damage Mechanics* 2008;0:10566789508091563.
- [17] Li SH, Ghosh S. Multiple cohesive crack growth in brittle materials by the extended Voronoi cell finite element model. *International Journal of Fracture* 2006;141:373.
- [18] Li SH, Ghosh S. Extended Voronoi cell finite element model for multiple cohesive crack propagation in brittle materials. *International Journal for Numerical Methods in Engineering* 2006;65:1028.

- [19] Jain JR, Ghosh S. Damage evolution in composites with a homogenization based continuum damage mechanics model. *Journal of Applied Mechanics* 2008;75:031011.
- [20] Kim H. Investigation of critical issues in Thermal Barrier Coating durability. *Mechanical Engineering*, vol. Ph.D. Columbus: Ohio State University, 2005.
- [21] Choi SR, Hutchinson JW, Evans AG. Delamination of multilayer thermal barrier coatings. *Mechanics of Materials* 1999;31:431.
- [22] Hutchinson JW, He MY, Evans AG. The influence of imperfections on the nucleation and propagation of buckling driven delaminations. *Journal of the Mechanics and Physics of Solids* 2000;48:709.
- [23] Yanar NM, Kim G, Hamano S, Pettit FS, Meier GH. Microstructural characterization of the failures of thermal barrier coatings on Ni-base superalloys. *Materials at High Temperatures* 2003;20:459.
- [24] Ansys7.0. *Structural Analysis Guide*: Ansys Inc., 2003.
- [25] Parks DM. A stiffness derivative finite element technique for determination of crack tip stress intensity factors. *International Journal of Fracture* 1974;10:487.
- [26] Cook RD, Malkus DS, Plesha ME. *Concepts and Applications of FE Analysis*. New York: John Wiley & Sons, 1989.
- [27] Pan D, Chen MW, Wright PK, Hemker KJ. Evolution of a diffusion aluminide bond coat for thermal barrier coatings during thermal cycling. *Acta Materialia* 2003;51:2205.
- [28] Johnson CA, Ruud JA, Bruce R, Wortman D. Relationships between residual stress, microstructure and mechanical properties of electron beam physical vapor deposition thermal barrier coatings. *Surface & Coatings Technology* 1998;109:80.
- [29] Cheng J, Jordan EH, Barber B, Gell M. Thermal/residual stress in an electron beam physical vapor deposited thermal barrier coating system. *Acta Mater.* 1998;46:5839.

- [30] Evans AG, Mumm DR, Hutchinson JW, Meier GH, Pettit FS. Mechanisms controlling the durability of thermal barrier coatings. *Progress in Material Science* 2001;46:505.
- [31] Reddy JN. *Elastic Plates: Theory and Analysis*, 1999.
- [32] Wang JS, Evans AG. Measurement and analysis of buckling and buckle propagation in compressed oxide layers on superalloy substrates. *Acta Materialia* 1998;46:4993.
- [33] Lundquist EE, Stowell, E. Z. Critical compressive stress for flat rectangular plates supported along all edges and elastically restrained against rotation along the unloaded edges. National Advisory Committee for Aeronautics Report 1942;No. 733:99.
- [34] Reismann H. Bending and buckling of an elastically restrained circular plate. *Journal of Applied Mechanics* 1952:167.
- [35] He MY, Evans AG. Effects of morphology on the decohesion of compressed thin films. *Physica Status Solidi A* 1998;166:19.
- [36] Cotterell B, Chen, Z. Buckling and cracking of thin films on compliant substrates under compression. *International Journal of Fracture* 2000;104:169.
- [37] Yu HH, Hutchinson JW. Influence of substrate compliance on buckling delamination of thin films. *International Journal of Fracture* 2002;113:39.
- [38] Mumm DR, Evans AG, Spitsberg IT. Characterization of a cyclic displacement instability for a thermally grown oxide in a thermal barrier system. *Acta Materialia* 2001;49:2329.
- [39] Tolpygo VK, Clarke DR. Surface rumpling of a (Ni, Pt)Al bond coat induced by cyclic oxidation. *Acta Materialia* 2000;48:3283.
- [40] Tolpygo VK, Clarke DR. Morphological evolution of thermal barrier coatings induced by cyclic oxidation. *Surface & Coatings Technology* 2003;163-164:81.
- [41] Yanar NM, Pettit FS, Meier GH. Effects of bond coat processing on the durability of thermal barrier coatings. *Thermec'2003, Pts 1-5, vol. 426-4. 2003. p.2453.*

- [42] Xu T, Faulhaber, S., Mercer, C., Maloney, M., Evans, A.G. Observations and analyses of failure mechanisms in thermal barrier systems with two phase bond coats on NiCoCrAlY. *Acta Materialia* 2004;52:1439.
- [43] Wang CM, lee KH. Buckling load relationship between Reddy and Kirchoff Circular plates. *Journal of the Franklin Institute* 1998;335:989.
- [44] Xu T, He MY, Evans AG. A numerical assessment of the propagation and coalescence of delamination cracks in thermal barrier systems. *Interface Science* 2003;11:349.
- [45] Anderson TL. *Fracture Mechanics*. Boca Raton, FL: CRC Press 1995.
- [46] Camacho GT, Ortiz M. Computational modelling of impact damage in brittle materials. *International Journal of Solids and Structures* 1996;33:2899.
- [47] Ortiz M, Pandolfi A. Finite-deformation irreversible cohesive elements for three-dimensional crack-propagation analysis. *International Journal for Numerical Methods in Engineering* 1999;44:1267.
- [48] Swaminathan S, Pagano NJ, Ghosh S. Analysis of interfacial debonding in three-dimensional composite microstructures. *Journal of Engineering Materials and Technology-Transactions of the Asme* 2006;128:96.
- [49] Xu XP, Needleman A. Numerical simulations of fast crack-growth in brittle solids. *Journal of the Mechanics and Physics of Solids* 1994;42:1397.
- [50] Nguyen O, Repetto EA, Ortiz M, Radovitzky RA. A cohesive model of fatigue crack growth. *International Journal of Fracture* 2001;110:351.
- [51] Maiti S, Geubelle PH. A cohesive model for fatigue failure of polymers. *Engineering Fracture Mechanics* 2005;72:691.
- [52] Erdogan F, Sih GC. On the crack extension in plates under plane loading and transverse shear. *Journal of Basic Engineering - Transactions of the ASME* 1963;85:519.
- [53] Palaniswamy KK, W. G. On the problem of crack extension in brittle solids under general loading. *Mechanics Today*, vol. 4: Pergamon Press, 1978. p.87.

- [54] Sih GC. Strain energy density factor applied to mixed mode crack problem. *International Journal of Fracture* 1974;10:305.
- [55] Abaqus. Users Manual: Hibbit, Karlsson and Sorrensen, 2005.
- [56] Balint DS, Hutchinson JW. An analytical model of rumpling in thermal barrier coatings. *Journal of the Mechanics and Physics of Solids* 2005;53:949.
- [57] Zhu DM, Miller RA, Nagaraj BA, Bruce RW. Thermal conductivity of EB-PVD thermal barrier coatings evaluated by a steady-state laser heat flow technique. *Surface & Coatings Technology* 2001;138:1.
- [58] Adams JW, Ruh R, Mazdiyasi KS. Young's Modulus, Flexural Strength, and Fracture of Yttria-Stabilized Zirconia versus Temperature. *Journal of the American Ceramic Society* 1997;80 [4]:903.
- [59] Gell M, Vaidyanathan K, Barber B, Cheng J, Jordan E. Mechanism of spallation in platinum aluminide/electron beam physical vapor-deposited thermal barrier coatings. *Metallurgical and Materials Transactions a-Physical Metallurgy and Materials Science* 1999;30:427.
- [60] Bhatnagar H, Walter ME, Ghosh S. A parametric domain map for top coat damage initiation and propagation in EB-PVD thermal barrier coatings. *International Journal for Multiscale Computational Engineering* 2007;5:227.
- [61] Raghavan P, Ghosh S. A continuum damage mechanics model for unidirectional composites undergoing interfacial debonding. *Mechanics of Materials* 2005;37:955.
- [62] Glowinski R, Lawton W, Ravachol M, Tenenbaum E. Wavelet solutions of linear and nonlinear elliptic, parabolic and hyperbolic problems in one space dimension. *Computing Methods in Applied Science and Engineering* 1990.
- [63] Jaffard S. Wavelet methods for fast resolution of elliptic problems. *Journal of Numerical Analysis* 2000;188.
- [64] Qian S, Weiss J. Wavelet and the numerical solution of boundary value problems. *Applied Mathematics Letters* 1993;6.

- [65] Li SH. Extended Voronoi cell finite element model for damage in brittle matrix composites. Mechanical Engineering, vol. Ph.D. Columbus: Ohio State University, 2006.
- [66] Li SH, Ghosh S. Modeling interfacial debonding and matrix cracking in fiber reinforced composites by the extended Voronoi cell FEM. Finite Elements in Analysis and Design 2007;43:397.
- [67] Ghosh S, Mukhopadhyay SN. A 2-Dimensional automatic mesh generator for finite element analysis for random composites. Computers and Structures 1991;41:245.
- [68] Ghosh S, Mukhopadhyay SN. A material based finite element analysis of heterogeneous media involving Dirichlet tessellations. Computer Methods in Applied Mechanics and Engineering 1993;104:211.
- [69] Daubechies I. Ten lectures in wavelets Society for Industrial and Applied Mathematics 1988.
- [70] Crisfield MA. A fast incremental/iterative solution procedure that handles 'snap-through'. Computer Structures 1981;13.
- [71] Crisfield MA. An arc-length method including line searches and accelerations. International Journal for Numerical Methods in Engineering 1983;19.
- [72] Schweizerhof KH, Wriggers Y. Consistent linearization for path following methods in nonlinear F.E. analysis. Computer Methods in Applied Mechanics and Engineering 1986;59.
- [73] Moorthy S, Ghosh S. Adaptivity and convergence in the voronoi cell finite element model for analyzing heterogeneous materials. Computer Methods in Applied Mechanics and Engineering 2000;185.
- [74] Kachanov LM. Introduction to continuum damage mechanics. Dordrecht, Boston: Nijhoff, Martinus, 1987.
- [75] Raghavan P, Ghosh S. A continuum damage mechanics model for unidirectional composites undergoing interfacial debonding. Mechanics of Materials 2005;37:955.

- [76] Cordebois J, Sidoroff F. Anisotropic damage in Elasticity and placticity. *Journal de Mecanique Theorique et Appliquee* 1982;45.
- [77] Murakami S. Mechanical modeling of material damage. *Journal of Applied Mechanics* 1988;55:280.
- [78] Voyiadjis GZ, Kattan PI. On the symmetrization of the effective stress tensor in continuum damage mechanics. *Journal of Mechanical Behavior of Material* 1996;7:139.
- [79] Barenblatt GI. The mathematical theory of equilibrium cracks in brittle fracture. *Advances in Applied Mechanics* 1962;7.
- [80] Dugdale DS. Yielding in steel containing slits. *Journal of the Mechanics and Physics of Solids* 1960;8.
- [81] Foulk JW, Allen DH. Formulation of a three-dimensional cohesive zone model for application to a finite element algorithm. *Computer Methods in Applied Mechanics and Engineering* 2000;183.
- [82] Geubelle PH. Finite deformation effects in homogeneous and interfacial fracture. *International Journal of Solids and Structures* 1995;32:1003.
- [83] Ghosh S, Ling Y, Majumdar B, Kim R. Interfacial debonding analysis in multiple fiber reinforced composites. *Mechanics of Materials* 2000;32:561.
- [84] Pellegrino C, Galvanetto U, Schrefler BA. Numerical homogenization of periodic composite materials with non-linear material components. *International Journal for Numerical Methods in Engineering* 1999;46:1609.
- [85] Segurado J, Llorca J. A numerical approximation to the elastic properties of sphere-reinforced composites. *Journal of the Mechanics and Physics of Solids* 2002;50:2107.
- [86] Mercer C, Faulhaber S, Evans AG, Darolia R. A delamination mechanism for thermal barrier coatings subject to calcium-magnesium-alumino-silicate (CMAS) infiltration. *Acta Materialia* 2005;53:1029.

- [87] Chen X, Wang R, Yao N, Evans AG, Hutchinson JW, Bruce RW. Foreign object damage in a thermal barrier system: mechanisms and simulations. *Materials Science and Engineering a-Structural Materials Properties Microstructure and Processing* 2003;352:221.
- [88] Chen MW, Glynn ML, Ott RT, Hufnagel TC, Hemker KJ. Characterization and modeling of a martensitic transformation in a platinum modified diffusion aluminide bond coat for thermal barrier coatings. *Acta Materialia* 2003;51:4279.